CDF/PHYS/EXOTIC/CDFR/8647
December 20, 2006

Search for the contribution of $H \to WW^*$ to the cross section for high transverse momentum dileptons in 1 fb^{-1} of Run II Data

D. Benjamin [i], P. Bussey [ii],S. Chuang [iii], T. Davies [ii], D. Hidas [i], M. Kruse [i], A. Robson [ii], R. St. Denis [ii], A.S. Thompson [ii]

[i)] Duke University
[ii)] Glasgow University
[iii)] Rutgers University

Abstract

We have searched for the contribution of the Standard Model Higgs to the production of high transverse momentum dileptons using approximately 1 fb^{-1} Tevatron Run 2 data collected by the CDF detector. The dominant Higgs decay in this search is that to W pairs where the W decays to an electron, muon or a tau which itself decays to an electron or muon. A cuts based analysis of the azimuthal distribution of the dileptons plus a variety of multivariate techniques having different input variables are used to study these high p_t dileptons. No evidence of a contribution of the Higgs decays to the dilepton cross section is observed. For Higgs masses of 110, 120, 130, 140, 150, 160, 170, 180, 190 and 200 GeV we obtain 95% CL limits on the $p\bar{p} \to H^0 \to WW^*$ of ?, 12.8, 8.5, 6.4, 4.8, 3.0, 3.3, 4.6, 6.4 and 8.1 pb, with expected limits of ?, 7.6, 4.4, 3.5, 2.7, 1.7, 1.9, 2.8, 3.6, and 4.3 pb. These expected limits are factors of ?, 57, 19, 11, 7.5, 4.4, 5.6, 10.0, 18.5 and 27.9 larger than the expected NNLO Standard Model cross sections.

1 Introduction

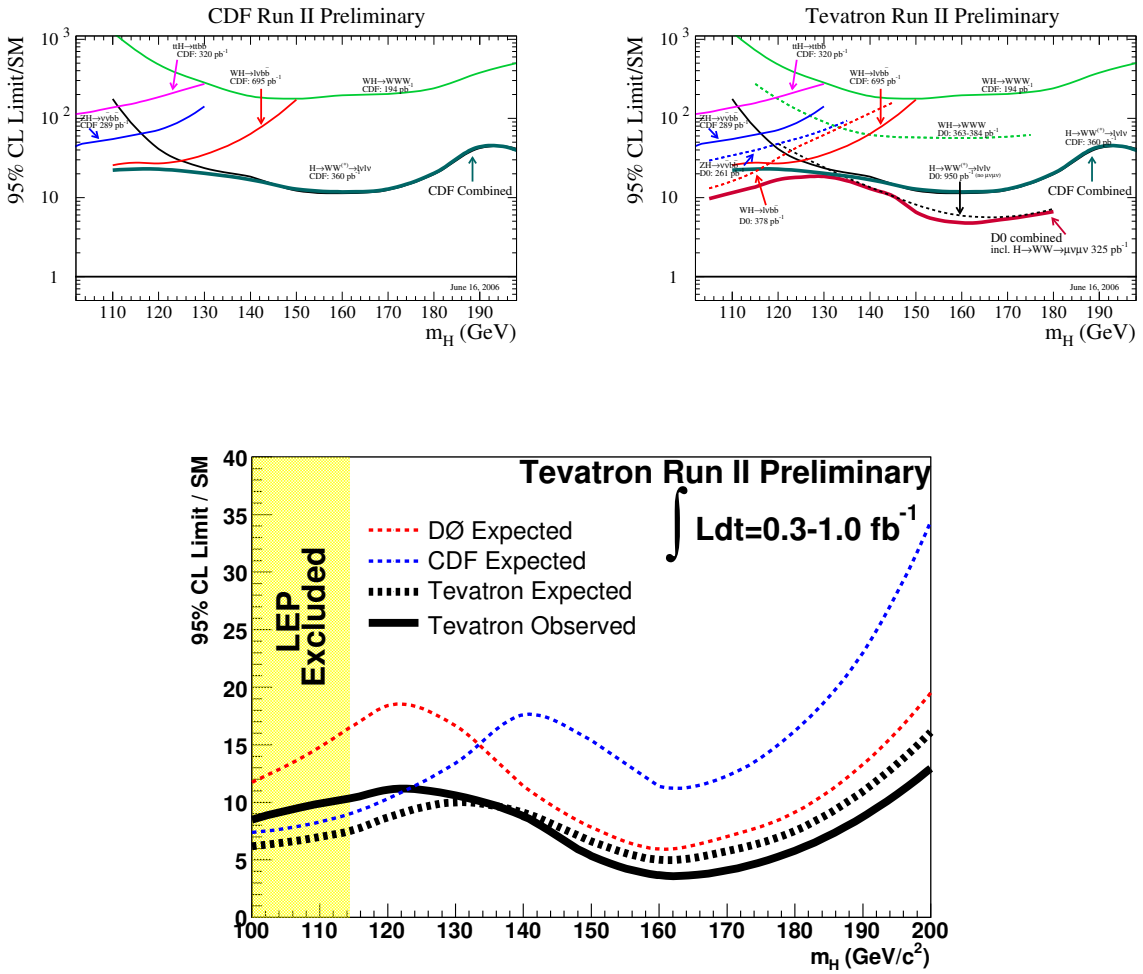

Figure 1: Summer 2006 CDF Higgs direct search cross section limits(top) and combined CDF/D0 Higgs limits on a log (middle) and linear (bottom) scale expressed in terms of the Standard Model Higgs production cross section

.

Searches for evidence of the contribution of the Higgs to events observed at the Tevatron are intensifying as the data sample is increasing. A previous analysis of dileptons [1] put limits on the cross section at about a factor of 14 higher than the standard model prediction at $M_h = 160\text{GeV/c}^2$. With improvements in NNLO computations [2] this became a factor of 10. Results for the direct search of a Standard Model Higgs presented in summer of 2006 for CDF alone as well as with CDF and D0 combined are shown in Figure 1. The limit on the cross section limit

for production of a standard model higgs having $M_h = 160\text{GeV/c}^2$ comes to within a factor of 4 of the Standard Model Prediction. CDF improvements and increased data volume for the low mass values of the Higgs have resulted in signficant improvements such that all values are now a within a factor of 20 of the Standard Model cross section in the range $114 < M_h < 200$ GeV/c^2.

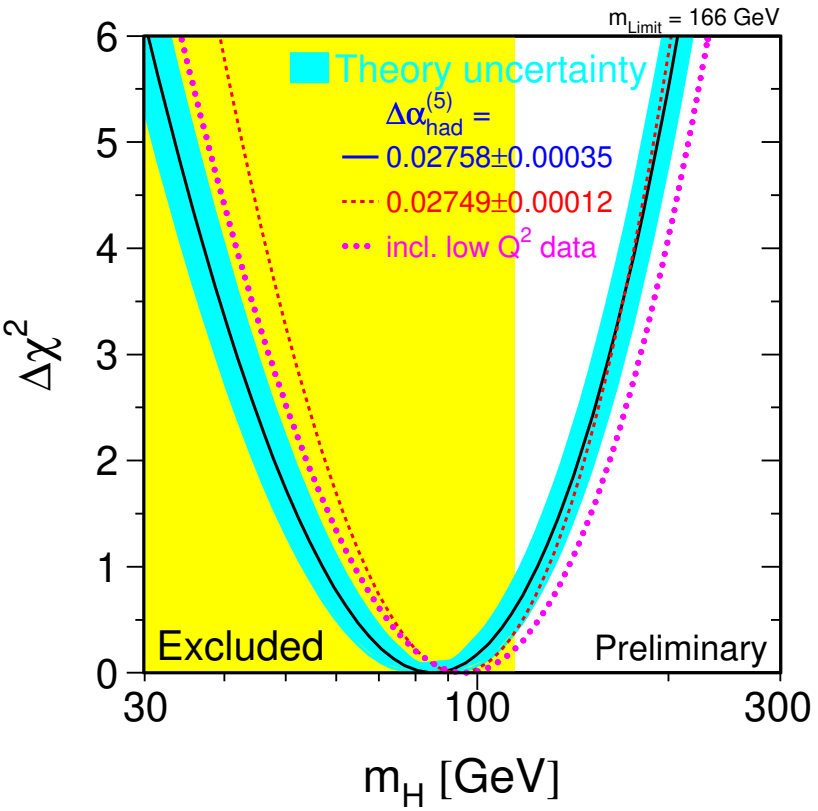

Figure 2: Summer 2006 Electoweak working group fits to the Standard Model Higgs.

The latest Electroweak working group fits [3] shown in Figure 2 place the preferred value at $M_h = 85^{+39}_{-28}\text{GeV/c}^2$, at 68% confidence level. Precision electroweak measurements indicate that that M_h <166 GeV/c^2 at 95% confidence. Direct searchs indicate that M_h >114.4 GeV/c^2 at 95% confidence [4]. Combining this with the precision electroweak measurements gives a limit of M_h <199 GeV/c^2 at 95% confidence.

At the Tevatron the dominant SM Higgs boson production mechanism is gluon-gluon fusion, gg→H (Figure 3). A second Higgs production mechanism, vector boson fusion, produces the same final state plus two forward, hard jets, and contributes an extra 7% to the WW final state. A third Higgs production mechanism, quark-quark fusion, which produces a Higgs in association

with a W boson, is about 2 orders of magnitude smaller. The branching ratios of the Higgs to W pairs dips to 15% at 120GeV/c^2 and rises to 90% at 160GeV/c^2, contributing to the search over the full range from 110 GeV/c^2 to 200 GeV/c^2. This is the range considered in this analysis.

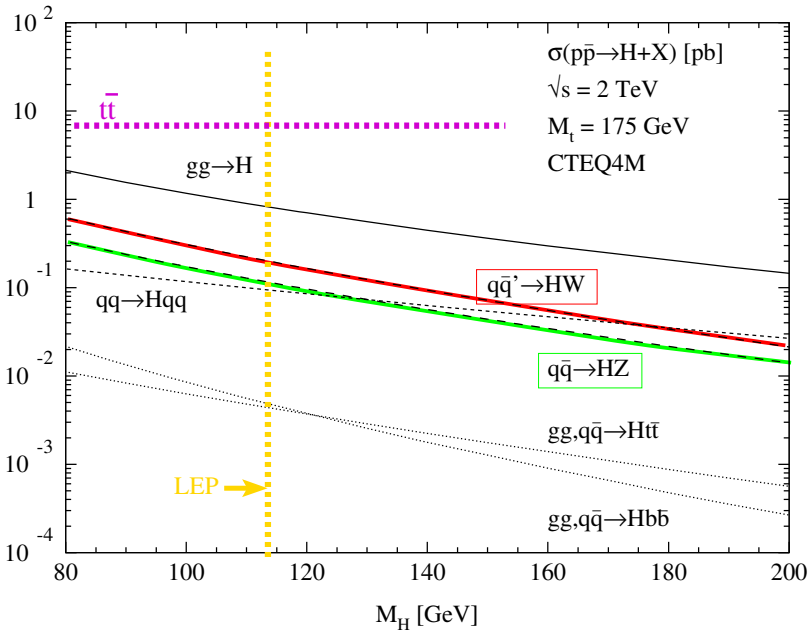

Figure 3: SM Higgs production versus the mass of the Higgs boson.

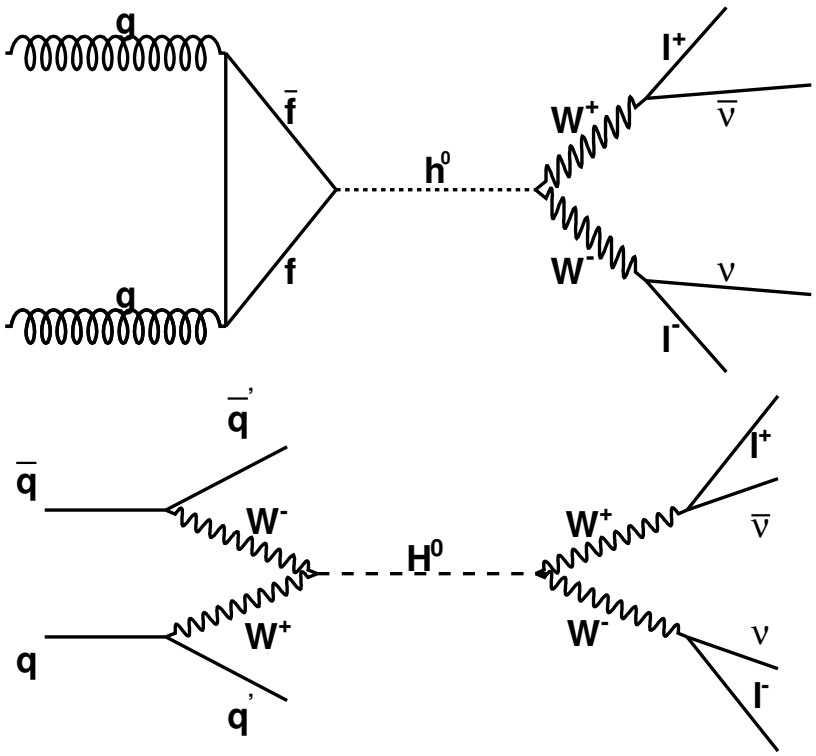

Figure 4: Feynman diagram for the dominant production mechanism and for a secondary contribution to the same final state of both final state W's decaying leptonically.

M_h	$gg \to H^0$	Vbf	Br(WW)	$gg \to H^0$ $\to WW$	Vbf$\to H^0$ $\to WW$	gg$\to H^0$ $\to WW$ $\to llvv$	Vbf$\to H^0$ $\to WW$ $\to llvv$	Tot
GeV/c^2	fb	fb		fb	fb	fb	fb	fb
100	1657	99.5	0.1000	165.7	9.95	17.46	1.05	18.51
110	1281		0.0440	56.36	9.71	5.94	1.02	6.96
120	1006	71.7	0.1320	132.79	9.46	13.99	1	14.99
130	801		0.2869	229.81	17.32	24.21	1.83	26.04
140	646	52.1	0.4833	312.21	25.18	32.9	2.65	35.55
150	525		0.6817	357.89	29.8	37.71	3.14	40.85
160	431	38.2	0.9011	388.37	34.42	40.92	3.63	44.55
170	357		0.9653	344.61	30.43	36.31	3.21	39.52
180	297	28.3	0.9345	277.55	26.45	29.24	2.79	32.03
190	249		0.7761	193.25	20.94	20.36	2.21	22.57
200	211	21	0.7347	155.02	15.43	16.33	1.63	17.96

Table 1: The SM Higgs production cross section and branching ratios of H$\to$WW are presented [32]. Also the number of events produced in 1 fb^{-1} is shown, where ℓ = e, μ or τ. The VBF cross sections for M_h =110,130,150,170, and 190 GeV/c^2 are interpolations.

In this analysis the data sample has been tripled and more sophisticated multidimensional techinques attempt to use the dilepton events more efficiently. The standard model prediction of signal cross-sections and branching ratios, and the expected number of events in 1 fb^{-1} are shown in Table 1, for different Higgs masses for the gluon as well as vector boson fusion processes[1] The detector acceptances needs to be taken into account. The dilepton acceptance is of order 12% at $M_h = 160$ GeV/c^2.

This paper is organized as follows. First, the sources of dielpton events from the Standard Model are examined in Section 3. This motivates the analysis procedure that is described in Section 4: identification of leptons, jets and missing energy is required. The analysis is applied to data collected with high p_t lepton triggers or missing energy. It is also applied to simulations of the various sources of dileptons: Drell-Yan, WW, WZ and ZZ, Wγ, $t\bar{t}$, $b\bar{b}$ and Jets Faking leptons, plus $H^0 \to W^+W^-$ produced from gluon fusion or vector boson fusion. The datasets are described in Section 5. The validity of the dilepton identification is tested in Section 6. The method for determining the cross section for $\sigma(p\bar{p} \to Z^0) \times \mathrm{BR}(Z^0 \to l^+l^-)$ is described. This involves the definition of the method for determination of the dilepton acceptance, and in particular the weighting needed to incorporate the trigger, reconstruction and id efficienciences. The cross section is measured for all combinations of the various lepton types in CDF and uniformity to better than 1% is achieved. The Z^0 measurement is also used to determine the lepton energy scale. Given the ability to measure the dilepton efficienices correctly, further analysis to enhance the contribution of the Higgs to dileptons is done in Section 7. Systematic uncertainties in the acceptance are determined in Section 8. These include parton distribution

[1] In addition, this differs from the analagous table in CDF7708 [1] in that it contains the NNLO cross sections.

function effects, α_s, initial state radiation, jet energy scale and the weights. The resulting numbers of events from various subprocesses are give in Section 9. Distributions in the azimuthal separation of the dileptons are examined and fitted for the contribution of the Higgs in Section 10.

Having established the results with a simple cuts analysis, a multivariate approach is described in Section 11. A number of multivariate techniques are considered and the best for discriminating the contribution of the Higgs decays is chosen. Results of a fit to the output to a neural net trained first on Drell-Yan/Higgs discrimination and then to second neural net trained on WW/Higgs discrimination are fit using the same techniques as described in Section 10. Final results, a summary and conclusions are given in Section 12.

2 Worklist

Incomplete aspects of the documentation of the analysis include:

- Cosmic rejection algorithm and impact on acceptance
- Conversion rejection algorithm and impact on acceptance
- Update JP weight info on TCE and PHX.
- Description of problem in JP method for PDF uncertainties for $alpha_s$.
- Check References and ordering.
- Fill in table of average systematics for all sources from average $\Delta\phi_{ll}$ variation.
- Evaluate systematic from $\not\!\!E_T$ cut.

Incomplete aspects of the analysis itself are:

- Doing all PDF uncertainties for all backgrounds: needs coding
- Use 95.8% for Z vertex efficiency.
- Add systematics to Z cross sections.
- Tweak the Phx mass distribution.

Additional interesting analyses are:

- Reparing BMU stntuple or cutting on Lepton ID with -13 cm for BMU
- Examine the Z cross section after each cut used in the Higgs Analysis up to the Missing energy cut.
- Plot each of the quantities being cut upon in the cuts analysis before each cut is applied, not just the
- Plot the 40 eigenvector variations for each bin of $\Delta\phi_{ll}$ for each dilepton source – and decide if anything is interesting. Also, consider correlations. selected few.

3 Standard Model Processes Leading to Dilepton Final States

The aim of this analysis is to measure a contribution to the dilepton cross section from the process $p\bar{p} \to H \to W^+W^- \to \ell^+\ell^-\nu\bar{\nu}$, where $\ell = e, \mu$ or τ and $\tau \to eX$ or $\tau \to \mu X$. This process results in the final state of two leptons with an angle of less than 180^o between them due to neutrinos against which they recoil. In addition, there can be initial state radiation from the gluons in $gg \to H^0$ production which materialize as hadrons that recoil against the four leptons, changing the angles between the observable electrons and muons. For the case of vector boson fusion, two hard jets are also produced. Hence the emphasis of the analysis is the identification of dilepton events and the examination of the hard jet activity as well as the energy flow in those events as characterized by the Missing Et prescription. A major test of the correct identification of the leptons in these events is a measurement of the Drell-Yan cross section. This also represents a large but reducible background to identification of the Higgs contribution to the events.

3.1 Standard Model Processses

All possible standard model process resulting in dielptons are considered in this analysis. This includes

- Z/$\gamma \to$ ee
- Z/$\gamma \to \mu\mu$
- Z/$\gamma \to \tau\tau$
- non-resonant WW
- WZ
- ZZ
- W $\gamma \to e^+\nu\ \gamma$
- W $\gamma \to \mu^+\nu\gamma$
- t$\bar{t}$
- $b\bar{b} \to \ell^+\ell^- + X$
- QCD $\to \ell^+\ell^- + X$
- $gg \to H \to$WW
- $q\bar{q}' \to H \to$WWjj

The Z/γ processes tend to have leptons with large azimuthal separation. The WZ and ZZ events tend to have three or four leptons although when the leptons are not identified, then they can contribute to the dilepton events. Maximal lepton acceptance therefore not only enhances the search for the contribution of the Higgs to dileptons, but also reduces the misidentification of higher multiplicity sources of leptons as dilepton events.

The production of W events with a real photon that converts can also contribute to the dilepton sample. Clearly top events also provide a contribution but they are accompanied with hard jets. Therefore the identification of jets is necessary in this analysis in order to distinguish the contribution of top events to the sample of dileptons.

QCD production, especially of heavy flavors, will provide a contribution to dilepton events. In the case of heavy flavors, there can be pairs of semileptonic decays although the cross section is predominantly at lower transverse momentum. There can also be misidentification of jets as leptons, or fake leptons produced and make an apparent contribution to the dilepton sample. Both of these contributions are considered together in the indentification and measurement of "Fakes" described in [20].

4 Analysis Procedure

The analysis of dilepton final states proceeds according to the flow chart indicated in Figure 5. The input is either data or simulation of the processes described in 3.1 in either Topntuple or Stntuple format. The input formats are converted into an internal representation independent of the input and with all calibrations applied in the same way to give a set of uniform lepton and jet objects, called TDOtherToTop. The objects imitate the "make_class" format of the Gen5 Topntuple.

The TDOtherToTop objects allow for a study of muon classification and were used to produce the plots in [27]. When lepton identification is done, the resulting leptons are stored in a heirarchy that consists of a base class containing information that will eventually be stored in a dilepton ntuple and extra information that is stored in another tree in the same output file. Histograms of all distributions being cut upon with all cuts applied except for that in the indicated distribution ("N-1 Histograms") as well as the distributions of all the values after cuts are applied are made during the lepton ID process. The lepton selection is discussed in detail in section 4.1. Jet objects are formed from the jet collection objects if they have centroids further than $R \equiv \sqrt{\Delta\phi^2 + \Delta\eta^2} > 0.4$ from the lepton. $\Delta\phi$ is the azimuthal location of the lepton and $\Delta\eta$ the rapidity separation. Jets are then identified with respect to the existing leptons and stored in a format for writing out to a Tree. The Missing energy is corrected as described in Section 4.2. Cosmic ray rejection and trigger criteria are applied to pairs of dileptons and dileptons candidates are selected.

4.1 Lepton identification

Events with two leptons (electrons or muons) satisfying the criteria discussed below are selected. For the highest p_T lepton, the standard baseline cuts as recommended by the Joint Physics group [26] for intermediate and high p_t leptons, The identification of *electrons* in the *central part*

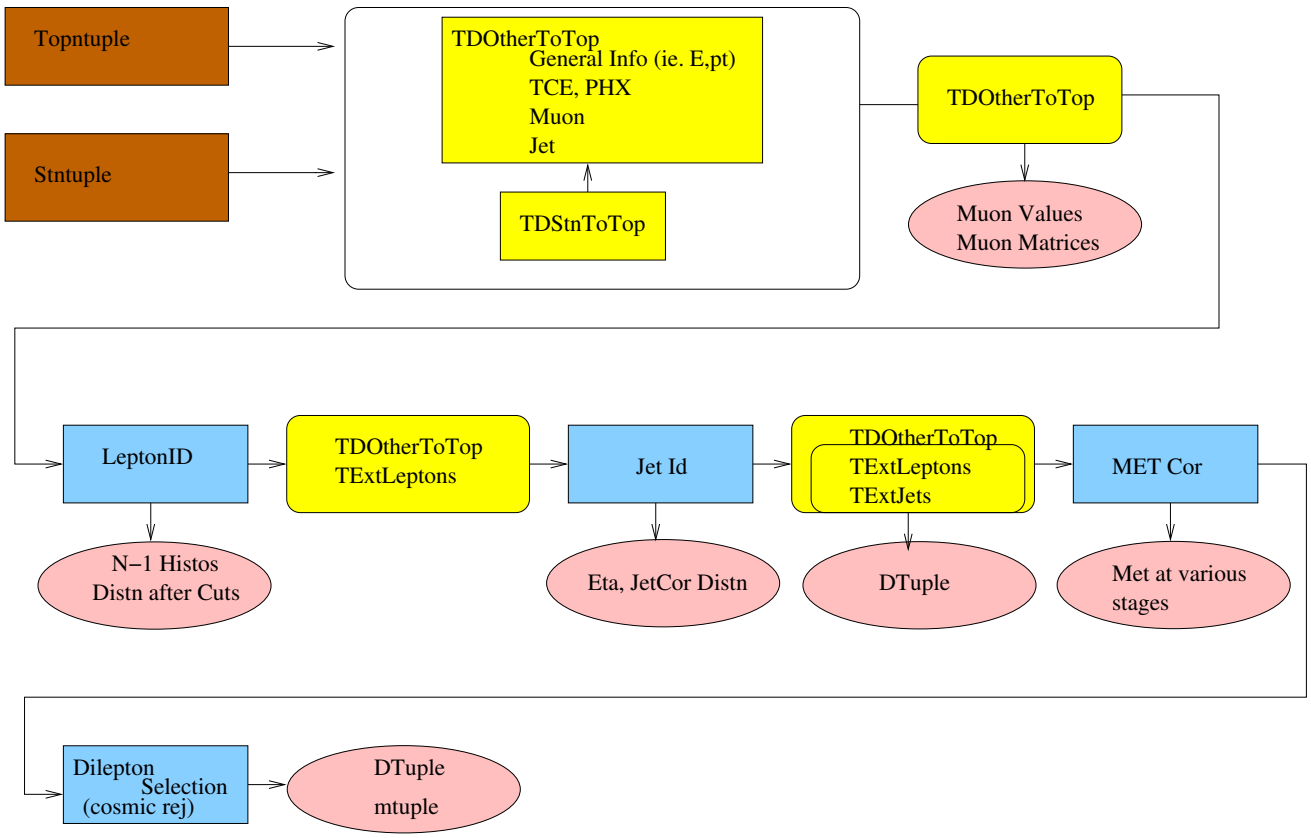

Figure 5: Analysis flow for dilepton selection. The input ntuple may be Topntuple or Stntuple. The quantities relevent to jets and leptons are converted to a common format with all corrections applied. The resulting TDOtherToTop object may then plot itself. Leptons are indentified according to the criteria approved of by the Joint Physics group. Jets are then identifiedwith respect to the existing leptons and stored in a format for writing out to a Tree. The Missing energy is corrected as described in Section 4.2. Cosmic ray rejection and trigger criteria are applied to pairs of dileptons and dileptons candidates are selected.

of the detector is based on the cuts listed in Table 2. The electrons are required not to be part of a conversion.

EM E_T	$>$ 20 GeV
E_{HAD}/E_{EM}	$< 0.055 + 0.00045 \cdot$E
L_{shr}	< 0.2
Track P_T	$>$10 GeV/c (if EM $E_T \leq$100 GeV) $>$50 GeV/c (if EM $E_T >$100 GeV)
E/p	$<$ 2 (if EM $E_T \leq$100 GeV)
$q \cdot \Delta x$	[-3.0, 1.5] cm
$\lvert\Delta z\rvert$	$<$ 3 cm
χ^2	$<$ 10
track $\lvert z_0\rvert$	$<$ 60 cm
Track quality	3 axial and 2 stereo SL with at least 5 hits out of 12 in each SL
Fiducial	*fidele*=1 (Ces $\lvert X\rvert <$21 cm, 9$<$ Ces $\lvert Z\rvert <$230 cm Tower 9 excluded, most of tower next to chimney included)

Table 2: Baseline cuts for central high-p_T electrons ($E_T >$ 20 GeV) (CEM) [26].

For the identification of *electrons* in the *plug region* of the detector the silicon tracks are reconstructed with the *Phoenix* algorithm [17]. If the plug electron passes all requirements described in Table 3, it is classified as Phoenix, denoted *PHX*. The cuts for lower E_T plug electrons ($E_T >$ 10 GeV) are identical with the ones for PHX.

EM E_T	$>$ 20 GeV
PhxMatch	true
E_{HAD}/E_{EM}	$< 0.05 + 0.026 \cdot \ln(\frac{E_{EM}}{100})$ (if $E_{EM} >$100 GeV) $<$ 0.05 (if $E_{EM} \leq$100 GeV)
PEM 3$\times$3 Fit tower	$\neq$0
PEM 3$\times$3 Fit χ^2	$<$10
PES 5$\times$9 U and V	$>$0.65
PES based Fiducial	1.2$<\lvert\eta\rvert<$2.0
Silicon track	2D Phoenix track
Number of Silicon Hits	$\geq$3
Track $\lvert z_0^{PHX}\rvert$	$<$ 60 cm
ΔR(Track, PES)	$<$3

Table 3: Baseline cuts for plug electrons (PHX) [26].

The selection of muons is described extensively in [27] and illustrated in Figure 6. Detailed confirmation of exact event by event categorization of muons consistent with that described in the CDF Muon trigger efficiency and id and reconstruction scale factors has been performed [27] and

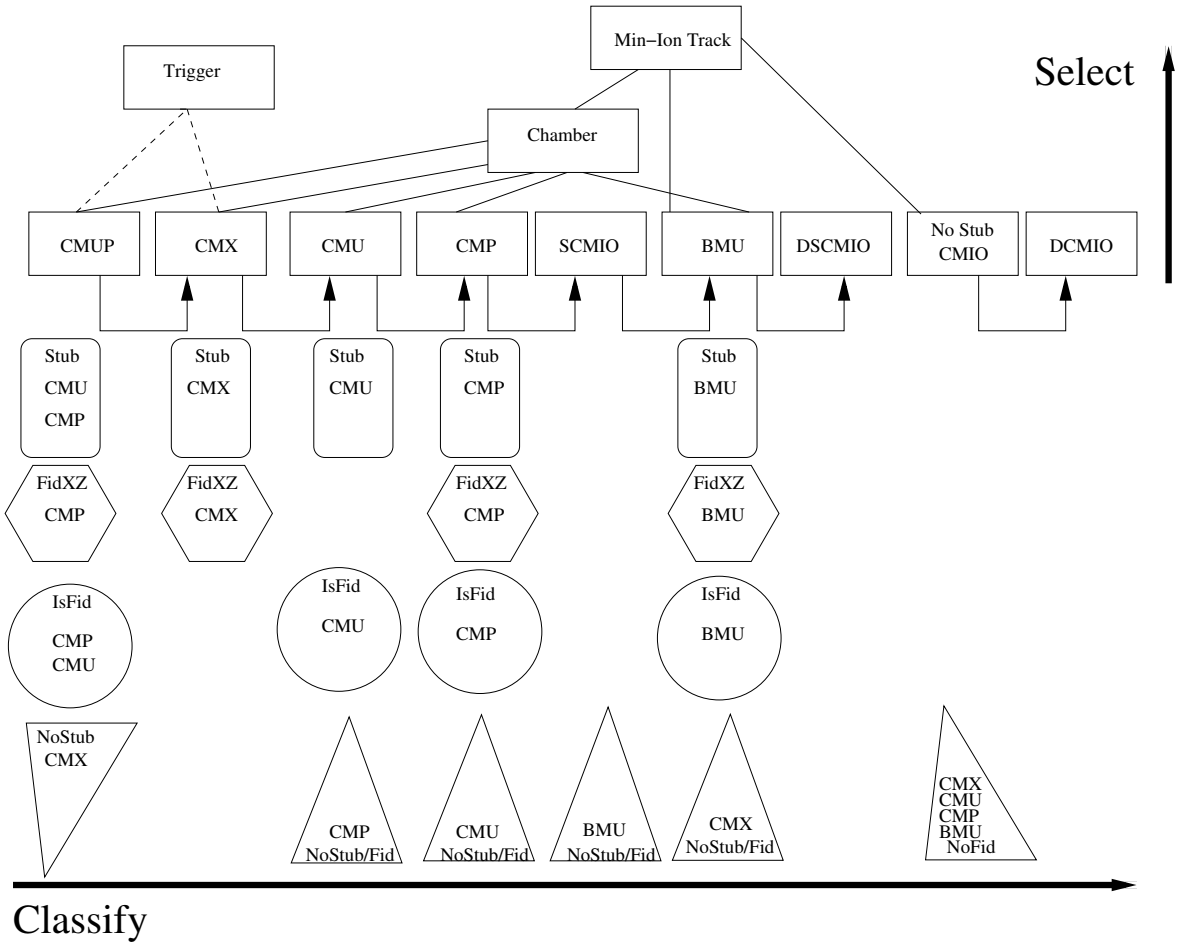

Figure 6: Muon Selection Scheme V

summarized here. The MuonLinkerModule takes by default the PADTracks collection. It looks at all the tracks with $p_t > 1.3$ GeV/c, $|d0| < 6.0$ cm and $|z_0| < 200.0$ cm and tries to associate them and the stubs. Then of the remaining unassociated PADTracks it takes those that have $p_t > 10.0$ GeV/c and adds them to the MuonColl. There is one CDFMuonColl but accessed via two MuonViews – defMuons for stubbed only, and defStublessMuons. Muon candidates are therefore minimum ionizing tracks either associated with stubs in the muon system or not associated with stubs. In either case, the tracks are further categorized by whether they are fiducial to a muon system or not.

Each candidate in the MuonColl is subjected to a combination of these stub and fiducial requirements to determine if they belong to a given muon category. The muon categories are: CMUP, CMX, CMU, CMP, SCMIO, BMU and DSCMIO for candidates having a stub associated with them, and CMIO or DSCMIO for those not having an associated stub. Stubbed muons are referred to as "chamber muons". Muons that can be triggered upon are called "Trigger Muons". Practically, this means that in the categorization of these muons, they will fall into

For CMUP:	x-fid(CMP) $<$ 0 cm, z-fid(CMP) $<$ -3 cm
For CMU-only:	-
For CMP-only:	x-fid(CMP) $<$ 0 cm, z-fid(CMP) $<$ -3 cm
For CMX	x-fid(CMX) $<$ 0 cm, z-fid(CMX) $<$ -3 cm

Table 4: Tight Baseline cuts categorizing minimum ionizing tracks [22].

their designated buckets only if they pass a 20GeV cut. The CMX trigger muon is required to have a $\rho_{COT} > 140$cm. This has the effect of putting low momentum (< 20GeV) CMUP and CMX muons into the SCMIO bucket. The high momentum CMX muons with $\rho_{COT} < 140$cm will end up in the DSCMIO bucket.

In the current analysis, no further action is taken with the DSCMIO or the DCMIO buckets.

The symbols in the diagram have the following meaning:

- A rounded rectangle contains the Stubs required.
- The hexagon indicates the tight Fiducial X,Z cuts required.
- The circle indicates the IsFiducial bit from MuonFiducialTool.
- The Triangles indicate veto:
  - If it points down, it is veto only on a stub (not used in this particular scheme);
  - if it points up, it is veto on fiducial and stub.

Hence, a muon will be considered CMUP if it has a stub in CMU and CMP and passes the CMP Fiducial cuts on X and Z Muons that fail to be put into the CMUP bucket are considered for the CMX bucket and so on down the line. Lose fiducial cuts correspond to the MuonFiducialTool bit being set and usually means x-fid< 0 and z-fid< 0. Tighter fiducial cuts are applied as listed in Table 4.

Once the muons are categorized, they are required to pass a set of baseline *muon* cuts (Table 5). CMIO and SCMIO also have a ρ_{COT} cut of 140cm plus an $E_{EM} + E_{HAD}$ cut. The chamber muons are subjected to a matching cut between the projected track position and the chamber stub position as per Table 6.

In addition a cosmic ray veto was applied.

The BMU alignment is off by 10 cm [28]. For Stntuple this was not taken into account for the data but was taken into account in the Monte Carlo.

When isolation is required for electrons or muons, it is defined as follows:

- $I_{cal} < 0.1$: the ratio of calorimeter energy, excluding the electron EM energy, in a cone of 0.4 around the electron, to the electron tower energy be less than 0.1. The isolation is leakage corrected.
- $I_{trk} < 0.1$: the ratio of the sum of the transverse momenta for all tracks in a cone of 0.4 around the lepton in the $\eta - \phi$ plane, excluding the lepton track, to the P_T of the lepton be less than 0.1.

Track $\|z_0\|$	$<$ 60 cm
E_{EM}	$<$ 2+Max(0,0.0115(P-100)) GeV
E_{HAD}	$<$ 6+Max(0,0.028(P-100)) GeV
Track $\|d_0\|$	0.2 cm (if no silicon hits attached by OI) 0.02 cm (if silicon hits attached by OI)
Track quality	3 axial and 2 stereo SL with at least 5 out of 12 in each SL
Track quality(BMU) Track $\|z_0\|$	3 axial and 2 stereo SL with at least 5 out of 12 in each SL $\|\eta\| \leq 1.25$ 2 axial and 2 stereo SL with at least 5 out of 12 in each SL $\|\eta\|$ >1.25 $<$ 60.0 cm
$E_{EM} + E_{HAD}$ (CMIO Only)	> 0.1

Table 5: Baseline cuts for minimum ionizing tracks [22].

$\|\Delta x_{CMU}\|$	$<$ 3.0 cm (CMUP or CMU)
$\|\Delta x_{CMP}\|$	$<$ 5.0cm (CMUP or CMP)
$\|\Delta x_{CMX}\|$	$<$ 6.0 cm (CMX)
$\|\Delta x_{BMU}\|$	$<$ 9.0 cm (CMX)

Table 6: Cuts for chamber muons [22].

4.2 Jets and Missing Energy

Once the leptons are identified, Jets objects can be formed and from these he Missing Energy can be computed.

Jets

The jets are the result of the fragmentation and hadronization of colored objects, such as quarks and gluons. There is assumed to be a one-to-one correspondence between a parton and its corresponding jet. The jets are clustered within a 0.4 cone and raw jet energies are applied level 5 energy corrections. Jets with E_T(L5 corrected) > 15 GeV and $\eta_{detector} < 2.5$ are selected[2].

Missing energy

The *raw* $\not\!\!E_T$ is defined as the negative vector sum of the transverse energy in the calorimeter, both electromagnetic and hadronic:

$$\vec{\not\!\!E_T} = -\sum_i [(E_i^{em} + E_i^{had}) sin\theta_i] \times \hat{n_i} \quad (1)$$

where E_i^{em}, E_i^{had} are the electromagnetic, respectively hadronic energy of the i^{th} tower, and $\hat{n_i}$ is a transverse unit vector pointing to the center of each tower. The θ_i is the polar angle of the i^{th} tower with respect to the z=0 coordinate frame. The sum in the above equation extends to $|\eta| < 3.6$, to avoid the forward calorimeter region.

On top of the raw $\not\!\!E_T$ there are few corrections applied, before using $\not\!\!E_T$ for an event selection:

[2]From now on, unless explicitly stated, by *jet* we will refer to such an object, with E_T(L5 corrected) > 15 GeV and $\eta_{detector} < 2.5$.

- *Primary vertex correction*: The raw missing energy stored in CdfMet bank assumes that the event primary vertex is z = 0; using the full offline event information one reconstruct the event primary vertex and then recalculate ($\not\!\!E_{Tx}, \not\!\!E_{Ty}$). This is done by choosing the vertex corrected $\not\!\!E_T$ in Stntuple and is already corrected in this way for top ntuple.

- *Muon correction*: The muons are minimum ionizing particles. Corrections are applied for Muons that pass a calorimeter and tracking isolation cut of Isolation$<$ 0.1. The light generated by these particles leads to a charge deposit on the calorimeter amplifiers that is interpreted as electromagnetic and hadronic energy. This apparent energy is added back to ($\not\!\!E_{Tx}, \not\!\!E_{Ty}$) the transverse energy deposited in the electromagnetic and hadronic calorimeter. Then the COT beam constrained muon momentum components, (P_{Tx}, P_{Ty}) are subtracted from the missing energy.

- *Jet correction*: Every jet is corrected for detector effects such as to get closer to parton level energies (as described above), before using it in the event selection. The missing energy is then corrected for the difference between the corrected and uncorrected jet transverse energies.

- *Electron Correction*: For electrons passing the calorimeter Isolation$<$ 0.1, the small corrections applied to obtain the Z mass are removed so as not to create false missing energy.

From this point on $\not\!\!E_T$ will refer to the corrected missing energy, unless explicitly stated otherwise.

4.3 Dilepton categories

A Dilepton event is built with two baseline isolated leptons according to the categorizations in Table 7.

The treatment of trileptons in this analysis is simple: events with three isolated leptons are classified as trileptons and saved in the dilepton ntuple although they are rejected in the final anlaysis.

5 Data and Monte Carlo Datasets

The processes described in Section 3.1 were simulated using releases 5.3.3_ewk and 6.1.4. The samples used to estimate the Wγ contribution were generated using Baur and Berger's WGAMMA program [34], using the following cuts: $|\eta^{lepton}| < 10$, $E_T^{\gamma} > 5.0$ GeV, $|\eta^{gamma}| < 10$ and $\Delta R(l, \gamma) > 0.2$ [33].

The samples used for signal and backgrounds, the MC generator, their dataset ids and the cross-sections are shown in Tables 8 and 9.

ee		$\mu\mu$		$e\mu$	
1st leg	2nd leg	1st leg	2nd leg	1st leg	2nd leg
TCE	**TCE**	**CMUP**	**CMUP**	**TCE**	**CMUP**
	PHX		**CMX**		**CMX**
			CMU		CMU
			CMP		CMP
			BMU		BMU
			SCMIO		SCMIO
			CMIO		CMIO
		CMX	**CMX**	**CMUP**	PHX
			CMU	**CMX**	PHX
			CMP		
			BMU		
			SCMIO		
			CMIO		
				PHX	CMU
					CMP
					BMU
					SCMIO
					CMIO

Table 7: Dilepton categories included in the current analysis. Shown in bold are the triggerable lepton in the data samples studied.

5.1 Fakes

The main source of fakes is W + multi-jet processes, with one jet/track misidentified as a lepton. The determination of fake rates is described in [20] and summarized here. A fake electron is essentially a cluster of electromagnetic energy and the jet sample is used to determine how often that was really a jet. A muon is an isolated track in the jet sample. The application of the fake rates determined by this method is described in [21] and summarized here. As each data and Monte Carlo sample dilepton selection is done, if there is only a single real lepton in the event, then the real lepton is paired with each fake candidate and the event is saved as a fake event for as many times as there are fake candidates. If there are no real leptons identified, then a dilepton would require two fakes so that case is neglected. If there are already two real leptons in the event, it is possible that a fake could cause a veto of a good event. This has not been considered.

Data samples rich in the dilepton processes described in Section 3.1 are obtained from events triggered on inclusive high-P_T leptons or *met*. These samples were processed with version 5.3.1 Production for runs 138425 to 186598 and version 6.1.4 for runs 190697 to 206989 and 206990 to 212133. These three run periods are referred to as the 0d, 0h and 0i periods [3] The central elec-

[3]Stntuple uses run 203799 as the break between 0h and 0i. For this analysis, Stntuple datasets are processed

Process	M_h(GeV/c^2)	Run Range		Parent Dataset ID	Gen	$\sigma(pb)$	# Events
gg	110	141572	179056	wexobw	5	0.006	1169876
gg	120	141572	179056	wexocw	5	0.014	1169876
gg	130	141572	179056	wexo5w	5	0.024	1155385
gg	140	141572	179056	wexo6w	5	0.033	1151850
gg	150	141572	179056	wexo7w	5	0.038	1167055
gg	160	141572	179056	wexo8w	5	0.041	1120599
gg	170	141572	179056	wexo9w	5	0.036	1106451
gg	180	141572	179056	wexoaw	5	0.029	1156264
gg	190	141572	179056	wexodw	5	0.020	1169876
gg	200	141572	179056	wexoew	5	0.016	1169876
gg	110	182843	203797	wexofw	6	0.006	1135132
gg	120	195346	203797	wexogw	6	0.014	653961
gg	130	182843	203799	wexohw	6	0.024	1263255
gg	140	182843	198695	wexoiw	6	0.033	1255785
gg	150	183077	199652	wexojw	6	0.038	956652
gg	160	182843	203799	wexokw	6	0.041	1333970
gg	170	183843	203799	wexolw	6	0.036	766537
gg	180	183843	203799	wexomw	6	0.029	1281142
gg	190	183843	203799	wexonw	6	0.020	1094778
gg	200	182843	203799	wexoow	6	0.016	849024
vbf	120	182843	194460	wexoqw	6	0.0150	474426
vbf	130	182843	203799	wexorw	6	0.0231	1308042
vbf	140	182843	203799	wexosw	6	0.0355	1315469
vbf	150	182843	194460	wexotw	6	0.0398	474426
vbf	160	182843	203799	wexouw	6	0.0445	1341456
vbf	170	182843	203506	wexovw	6	0.0378	1310384
vbf	180	183142	203457	wexoww	6	0.0320	1314737
vbf	190			wexonw	6	0.020	1094778

Table 8: Higgs Monte Carlo datasets used for HWW analysis.

Process	Run Range		Parent Dataset	$\sigma(pb)$	K	FF	Gen	# Events
$Z/\gamma \rightarrow$ ee	143980	186598	ze0s6d	355±3	1.4	1.0	5	2255968
	190753	203799	zewkad	355±3	1.4	1.0	6b	6915989
$Z/\gamma \rightarrow \mu\mu$	141572	186598	zewk6m	355±3	1.4	1.0	5	3247142
	190753	212133	zewk9m	355±3	1.4	1.0	6b	6924095
$Z/\gamma \rightarrow \tau\tau$	141572	186598	zewk8t	355±3	1.4	1.0	5	9219648
	190936	212133	zewkat	355±3	1.4	1.0	6b	6916050
WW	141572	186598	wewk5d	12.4	1.0	1.0	5	1608243
	190753	212133	wewkbd	12.4	1.0	1.0	6c	3469910
WZ	141572	186598	wewk6d	3.65	1.0	0.76	5	1747960
	191205	212133	wewkcd	3.65	1.0	0.76	6c	3598792
ZZ	141572	186598	wewk7d	1.39	1.0	0.23	5	1687299
	190753	212011	wewkdd	1.39	1.0	0.23	6c	3456173
W $\gamma \rightarrow e^+\nu\ \gamma$	141572	186598	rewk06	21.48	1.34	1.0	5	2981272
W $\gamma \rightarrow e^+\nu\ \gamma$	190753	203348	rewk08	21.48	1.34	1.0	6	3916626
W $\gamma \rightarrow \mu^+\nu\gamma$	141572	186598	rewk07	21.48	1.34	1.0	5	2804380
W $\gamma \rightarrow \mu^+\nu\ \gamma$	190753	203799	rewk09	21.48	1.34	1.0	6	4236385
$t\bar{t}$	141579	186598	tewk0z	6.7	1.0	1.0	5	2896611
$t\bar{t}$	190753	193051	tewk1z	6.7	1.0	1.0	6	106576

Table 9: Background Monte Carlo datasets used for HWW analysis. The Stntuple ID consists of the directory and the dataset needed to access the catalog. "K" is the factor to use for the higher order terms in the cross section. FF is the Filter Factor used to select events for simulation. Gen is the version of the Monte Carlo. "5" means that version 5.3.3_ewk was used. "6" means that version6.1.4 was used and the letter after it gives the subtag. The number of events is the number of simulated events on the stntuple.

trons (CEM) came in on $ELECTRON_CENTRAL_18$ trigger and correspond to the datasets bhel0d, bhel0h and bhel0i. The corresponding stntuple datasets are bexo4h, bexo1h and bhelbi respectively The muons were collected on the four triggers: MUON_CMUP18, MUON_CMX18, MUON_CMUP18_L2_PT15, MUON_CMX18_L2_PT15, from the bhmubd, bhmu0h and bhmu0i datasets. The corresponding stntuple datasets are bhmubd, bexo2h and bhmubi. The plug electron samples were bpel0d, bpel0h and bpel0i with stntuple samples bexo4d bexo3h and bpelbi. These were collected with MET_PEM trigger, which additionally requires large missing energy ($\not\!\!E_T > 15$ GeV), to keep the rates low.

Version 13 of the DQM good run list of the Top, EWK and Exotics groups is applied [4]. This covers all the runs numbers up to 212133 and does not include the "COT-compromised" period, where the lower gains affected the COT tracking efficiency (run range 179096-182842). In order to maximize the available data:

- In the ee channel the good run list without muon requirements is applied.
- The good run list without silicon checks is applied to the events that do not contain a PHX in the dilepton category.
- For dilepton events with a PHX (TCE-PHX, PHX-PHX, CMUP-PHX, CMX-PHX, PHX-CMU, PHX-CMP, PHX-CMIO) the good run list with good silicon has been applied.

Dilepton Combination Type	Good Run List	Offline $\mathcal{L}_{int}$ (pb^{-1}) +1.9% correction and ±5.9% errors
TCE-TCE	1001	1080 ± 65
PHX-{TCE, PHX}	1101	998 ± 60
TCE-{CMUP, CMU, CMP, CMIO}	1031	1052 ± 63
TCE-CMX	1021	1001 ± 60
PHX-{CMUP, CMU, CMP, CMIO}	1131	973 ± 58
PHX-CMX	1121	1033 ± 62
CMUP-{CMUP, CMU, CMP, CMIO}	0031	1105 ± 66
CMX-{CMUP, CMX, CMU, CMP, CMIO}	0011	1033 ± 62

Table 10: Luminosities of the different di-lepton categories used in the analysis.

.

The luminosities relevant for our dilepton categories are summarized in Table 10. For the Monte Carlo, the acceptances are scaled to the refernce TCE_TCE luminosity of:

$$\mathcal{L}_{HWW} = (1080 \pm 65)\,\mathrm{pb}^{-1}$$

Index	Sample Selection Cut
1	CMX wedge 14 not used if run > 190000
2	two leptons with $p_T^{l_{trigger,non-trigger}} > 20$, 10 GeV
3	calorimeter and track isolation < 0.1

Table 11: Cuts placed on the Dilepton input variables before the Z^0 analysis.

6 Z^0 analysis

In order to check the lepton selection, the Z^0 cross section is computed for all same-flavor dilepton categories. The selection cuts in Table 11 are applied to the dilepton candidates.

The Z cross section multiplied by branching ratio was calculated using the equation:

$$\sigma \cdot BR(Z \to l^+l^-) = \frac{I_2}{I_1} \frac{N_{obs} - N_{bg}}{A_Z^{weighted} \cdot \epsilon_{zvtz} \cdot \int Ldt}$$

where:

- I_2/I_1: Converts the calculation for Z/$\gamma^* \to l^+l^-$ over the mass region 66-116 GeV into that for $Z \to l^+l^-$ over the whole invariant mass range.
- N_{obs}: the number of signal events is the number of selected data events in which the leptons are oppositely charged.
- N_{bg}: the number of background events is estimated by counting the number of selected data events in which the leptons have the same charge.
- $A_Z^{weighted}$: A weigthed Acceptance is calculated using events which are weighted event by event with $A_Z^{weighted} = A_Z \cdot SF \cdot \epsilon_{trig}$. It is the number of selected, weighted Monte Carlo events divided by the total number of Generator-level good Monte Carlo events.
- The total number of Generator level good Monte Carlo events is the denominator of the Acceptance, and is found by counting the events in which the hepg Z mass lies in the Z Mass window. This is to account for the electroweak γ^* contribution and γ/Z interference.
- SF: the scale factor corrects for the difference in efficiency of the ID selection cuts between the Data and Monte Carlo. For muons, this is also multiplied by the reconstruction efficiency, SF_{rec}, which is the probability for the muon stubs to be associated with a track correctly.
- ϵ_{trig}: adds the trigger efficiency measured in data to reweight the Monte Carlo events. The sources of the values for these efficiencies are detailed in Table 13.

together and the run periods described above are used in indicating 0d, 0h and 0i.

[4] http://www-cdf.fnal.gov/internal/dqm/goodrun/v13/goodv13.html

- ϵ_{zvtz}: the efficiency of the Z vertex cut on z_0, as in CDF note 7935, is 0.951 for Gen 5

- $\int Ldt$: the integrated luminosity is found by summing the luminosities of the runs in the good run list from the ROOT file supplied in the version 13 good run list webpage: http://www-cdf.fnal.gov/internal/dqm/goodrun/v13/RunSummary.root. The Gen6 value in CDF Note 8313 is the same within uncertainties. This is then multiplied by 1.019.

6.1 Acceptance Denominator

There is a large γat low dilepton mass and γ/Z^0 contribution around the Z^0 resonance. The number of events generated is found by counting events containing Z^0 particles with a mass within the Z^0 mass window. The definition of the cross sections remove this contribution and consider only the contribution from Z^0 exchanage. This is achieved in this analysis by computing the dilepton mass mass from the Z^0 generator level (hepg) 4-vector. The cut on the lepton $|z_0|$ on the MC must also be accounted for in the denominator of the acceptance by requiring the primary vertax to have $|V_z| < 60$ cm. This information is taken from the Obsp bank. The event is also only counted if there exists two leptons originating from a Z^0 particle.

In total, the cuts which the generator-level event must pass to be part of the acceptance denominator are:

Acceptance denominator requirements

Z Mass	$116 < M_Z < 116$ GeV
leptons	2 leptons which have a Z ancestor
Primary Vertex	$\|\text{Vrtx}_z^{prim}\| < 60cm$

Table 12: *Acceptance denominator requirements.*

6.2 Dilepton Weighting

Each lepton is weighted with a Scale Factor separately, and these are multiplied together for the diletpon SF. This is then multiplied by the trigger efficiency for the triggerable lepton, and in the case where there are two triggerable leptons, the trigger efficiency for the dilepton pair becomes:

$$\epsilon_{trig}^{dilepton} = 1 - (1 - \epsilon_{trig}^{1})(1 - \epsilon_{trig}^{2})$$

The sources of the Efficiencies used are shown in Table 13.

Phoenix electrons have a charge misidentification probability [23]. The weights in Table 14 are applied to the simulated events to account for this.

Lepton Type	Efficiency	Run Range	Source	Location	Value
TCE	ϵ_{SF}		CDF Note 7950	Table 8 (p11)	0.981
	ϵ_{trig}		CDF note 7401	Table 19 (p42)	Depends on E_T
			CDF note 7939	Table 14 (p27)	
				Table 27 (p67)	
PHX					
CMUP	ϵ_{trig}		CDF Note 7956	Table 14 (p17)	0.905
	ϵ_{rec}	0d	CDF Note 8262	Table 22 (p17)	0.9482
	ϵ_{rec}	0h	CDF Note 8262	Table 22 (p17)	0.9403
	ϵ_{rec}	0i	CDF Note 8262	Table 22 (p17)	0.9401
	ϵ_{id}	0d	CDF Note 8262	Table 17 (p15)	0.9450
	ϵ_{id}	0h	CDF Note 8262	Table 17 (p15)	0.9507
	ϵ_{id}	0i	CDF Note 8262	Table 17 (p15)	0.9420
	$\epsilon_{sf} = \epsilon_{rec} \cdot \epsilon_{id}$	0d			0.8960
	$\epsilon_{sf} = \epsilon_{rec} \cdot \epsilon_{id}$	0h			0.8939
	$\epsilon_{sf} = \epsilon_{rec} \cdot \epsilon_{id}$	0i			0.8856
CMX (Arches)	ϵ_{trig}		CDF Note 7956	Table 14 (p17)	0.96
	ϵ_{rec}	0d	CDF Note 8262	Table 22 (p17)	0.9931
	ϵ_{rec}	0h	CDF Note 8262	Table 22 (p17)	0.9903
	ϵ_{rec}	0i	CDF Note 8262	Table 22 (p17)	0.9898
	ϵ_{id}	0d	CDF Note 8262	Table 17 (p15)	1.0058
	ϵ_{id}	0h	CDF Note 8262	Table 17 (p15)	1.0005
	ϵ_{id}	0i	CDF Note 8262	Table 17 (p15)	1.0055
	$\epsilon_{sf} = \epsilon_{rec} \cdot \epsilon_{id}$	0d			0.9989
	$\epsilon_{sf} = \epsilon_{rec} \cdot \epsilon_{id}$	0h			0.9908
	$\epsilon_{sf} = \epsilon_{rec} \cdot \epsilon_{id}$	0i			0.9952
CMU	ϵ_{rec}	0d	CDF Note 8262	Table 31 (p30)	0.9233
	ϵ_{rec}	0h	CDF Note 8262	Table 31 (p30)	0.9005
	ϵ_{rec}	0i	CDF Note 8262	Table 31 (p30)	0.8985
	ϵ_{id}	0d	CDF Note 8262	Table 40 (p33)	0.9729
	ϵ_{id}	0h	CDF Note 8262	Table 40 (p33)	0.9626
	ϵ_{id}	0i	CDF Note 8262	Table 40 (p33)	0.9684
	$\epsilon_{sf} = \epsilon_{rec} \cdot \epsilon_{id}$	0d			0.8983
	$\epsilon_{sf} = \epsilon_{rec} \cdot \epsilon_{id}$	0h			0.8668
	$\epsilon_{sf} = \epsilon_{rec} \cdot \epsilon_{id}$	0i			0.8701
CMP	ϵ_{rec}	0d	CDF Note 8262	Table 31 (p30)	0.9506
	ϵ_{rec}	0h	CDF Note 8262	Table 31 (p30)	0.9542
	ϵ_{rec}	0i	CDF Note 8262	Table 31 (p30)	0.9509
	ϵ_{id}	0d	CDF Note 8262	Table 40 (p33)	0.9711
	ϵ_{id}	0h	CDF Note 8262	Table 40 (p33)	0.9760
	ϵ_{id}	0i	CDF Note 8262	Table 40 (p33)	0.9776
	$\epsilon_{sf} = \epsilon_{rec} \cdot \epsilon_{id}$	0d			0.9231
	$\epsilon_{sf} = \epsilon_{rec} \cdot \epsilon_{id}$	0h			0.9313
	$\epsilon_{sf} = \epsilon_{rec} \cdot \epsilon_{id}$	0i			0.9296
CMIO	$\epsilon_{sf} = \epsilon_{id}$	0d	CDF Note 8262	Table 41 (p34)	1.0366
	$\epsilon_{sf} = \epsilon_{id}$	0h	CDF Note 8262	Table 41 (p34)	1.0340
	$\epsilon_{sf} = \epsilon_{id}$	0i	CDF Note 8262	Table 41 (p34)	1.0423
SCMIO	$\epsilon_{sf} = \epsilon_{id}$	0d	CDF Note 8262	Table 41 (p34)	0.9909
	$\epsilon_{sf} = \epsilon_{id}$	0h	CDF Note 8262	Table 41 (p34)	0.9897
	$\epsilon_{sf} = \epsilon_{id}$	0i	CDF Note 8262	Table 41 (p34)	0.9750

Table 13: *Lepton Trigger efficiencies and Scale Factors, their sources and values.*

$\lvert\eta_{\text{PHX PES}}\rvert$ Range	Data/MC Scale Factor	
	(Run<190000)	(run>190000)
$1.2 < \lvert\eta\rvert < 1.4$	$(1. - 0.061)/(1. - 0.061)$	$(1. - 0.059)/(1. - 0.066)$
$1.4 < \lvert\eta\rvert < 1.6$	$(1. - 0.099)/(1. - 0.097)$	$(1. - 0.092)/(1. - 0.113)$
$1.6 < \lvert\eta\rvert < 1.8$	$(1. - 0.150)/(1. - 0.143)$	$(1. - 0.151)/(1. - 0.157)$
$1.8 < \lvert\eta\rvert < 2.0$	$(1. - 0.168)/(1. - 0.138)$	$(1. - 0.149)/(1. - 0.168)$
$2.0 < \lvert\eta\rvert < 2.2$	$(1. - 0.112)/(1. - 0.105)$	$(1. - 0.187)/(1. - 0.194)$
$2.2 < \lvert\eta\rvert < 2.4$	$(1. - 0.112)/(1. - 0.105)$	$(1. - 0.264)/(1. - 0.272)$
$2.4 < \lvert\eta\rvert < 2.6$	$(1. - 0.112)/(1. - 0.105)$	$(1. - 0.307)/(1. - 0.371)$
$2.6 < \lvert\eta\rvert < 2.8$	$(1. - 0.112)/(1. - 0.105)$	$(1. - 0.374)/(1. - 0.438)$

Table 14: PHX charge mis-identification scale factors [16].

6.3 Lepton Energy Scale

The analysis of Z^0 also yields a measurement of the lepton energy scale. The Z^0 invariant masses for all lepton types are showin in Figures 7 to 9 where the histogram is the Monte Carlo prediction and the points are the data. Contribution from all processes listed in Section 3.1 are shown. The dominant source of dileptons is clearly Z^0 decays: logarithmic plots are provided to enable one to see contributions from all the processes.

The phoenix electron energy has been corrected with scale factors as listed in Table 15, bringing the $Z \to e_{\text{TCE}} e_{\text{PHX}}$ mass peak to 91 GeV as shown in Figure 9. The values of the masses are given in Table 17. Deviations from the average are used in the determination of the lepton energy scale systematic. Plots of the mean Z^0 mass for Data and Monte Carlo for each dielpton type are show in Figure 10.

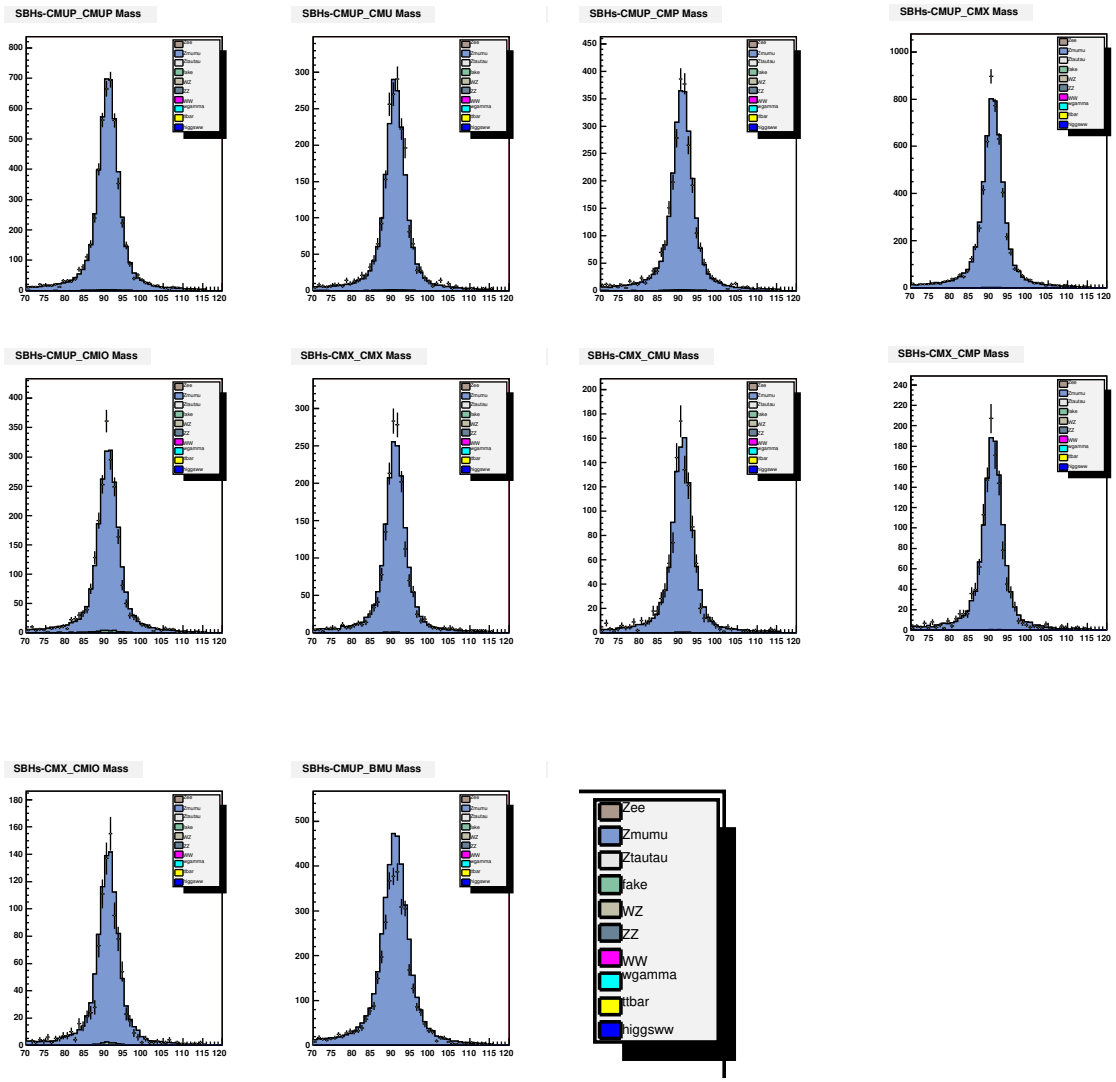

Figure 7: The dimuon mass peak after selection for Drell-Yan for all muon systems (linear scale).

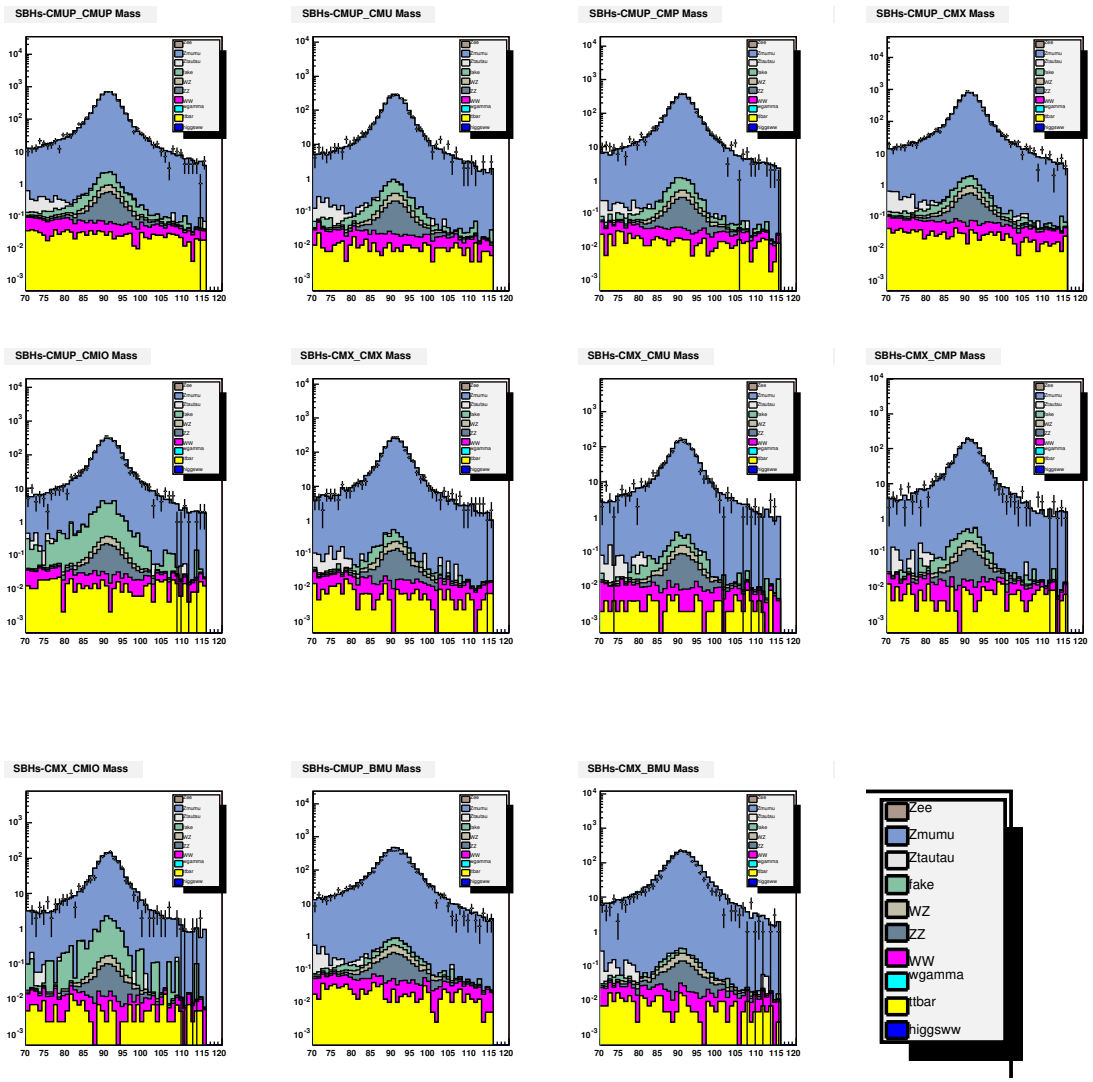

Figure 8: The dimuon mass peak after selection for Drell-Yan for all muon systems (log scale).

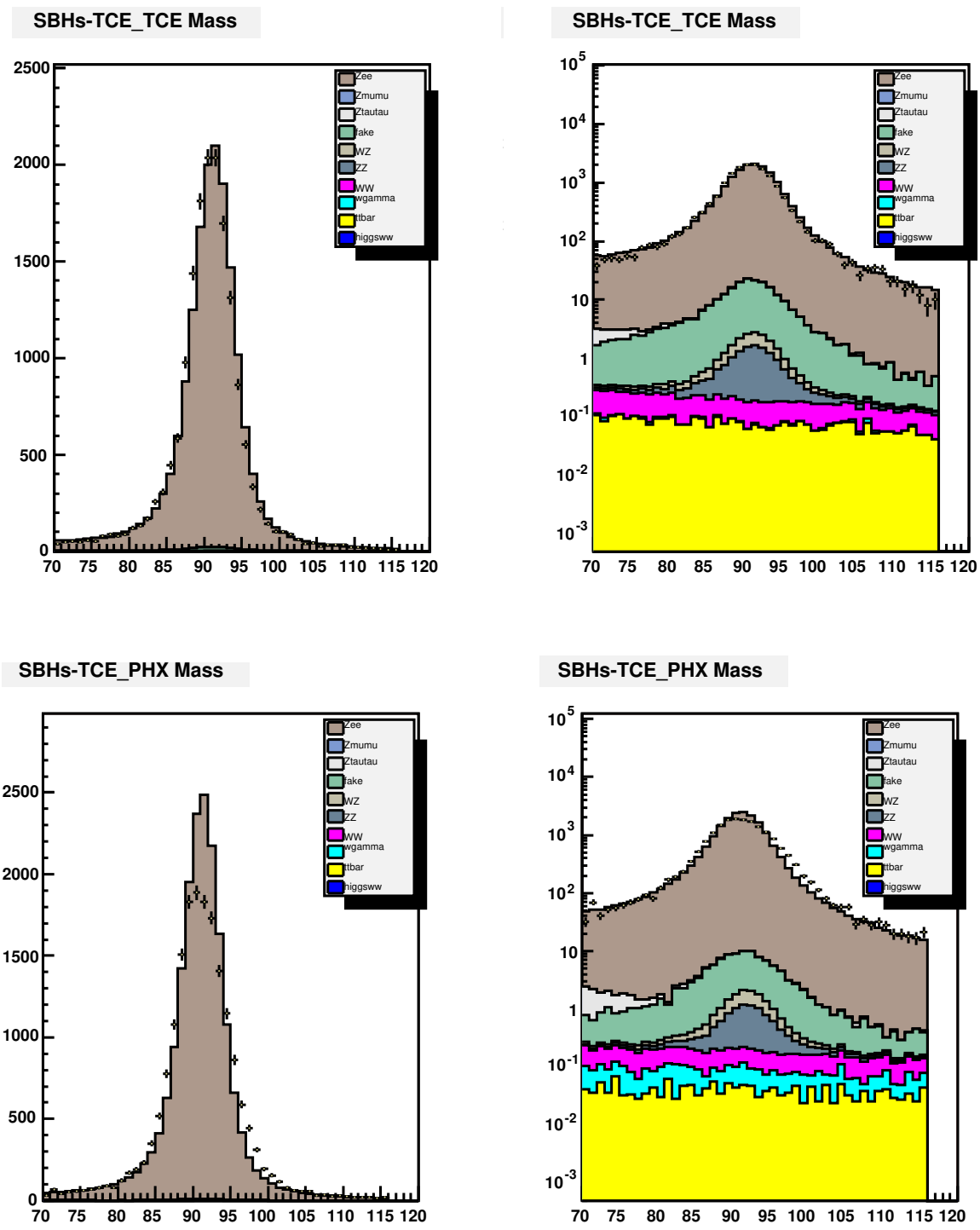

Figure 9: The mass peak of $Z \to e_{\rm TCE} e_{\rm PHX}$ with phoenix electron energies scaled up as listed in Table 15.

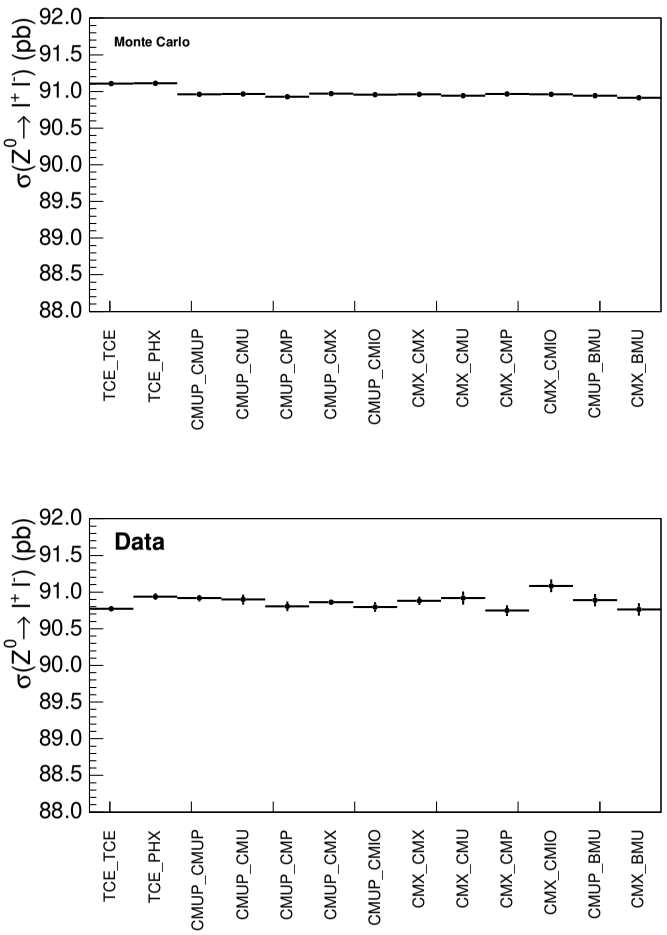

Figure 10: Z^0 mass in Monte Carlo and Data for each dilepton type

	MC		Data	
Low Run	$\eta < 0$	$\eta > 0$	$\eta < 0$	$\eta > 0$
141544	1.039	1.039	1.014	1.014
156487	1.032	1.034	1.014	1.014
168889	1.036	1.038	1.014	1.014
190696	1.037	1.044	1.014	1.014
195408	1.035	1.038	1.014	1.014
198380	1.030	1.043	1.014	1.014
201349	1.035	1.034	1.014	1.014
203818	1.035	1.035	1.014	1.014
206989	1.037	1.038	1.014	1.014
210011	1.040	1.032	1.014	1.014

Table 15: Phoenix electron energy scale factors divided by run range, plug side ($\eta > 0$ for east; $\eta < 0$ for west) and data/MC.

6.4 $\sigma(p\bar{p} \to Z^0) \times \mathrm{BR}(Z^0 \to l^+l^-)$

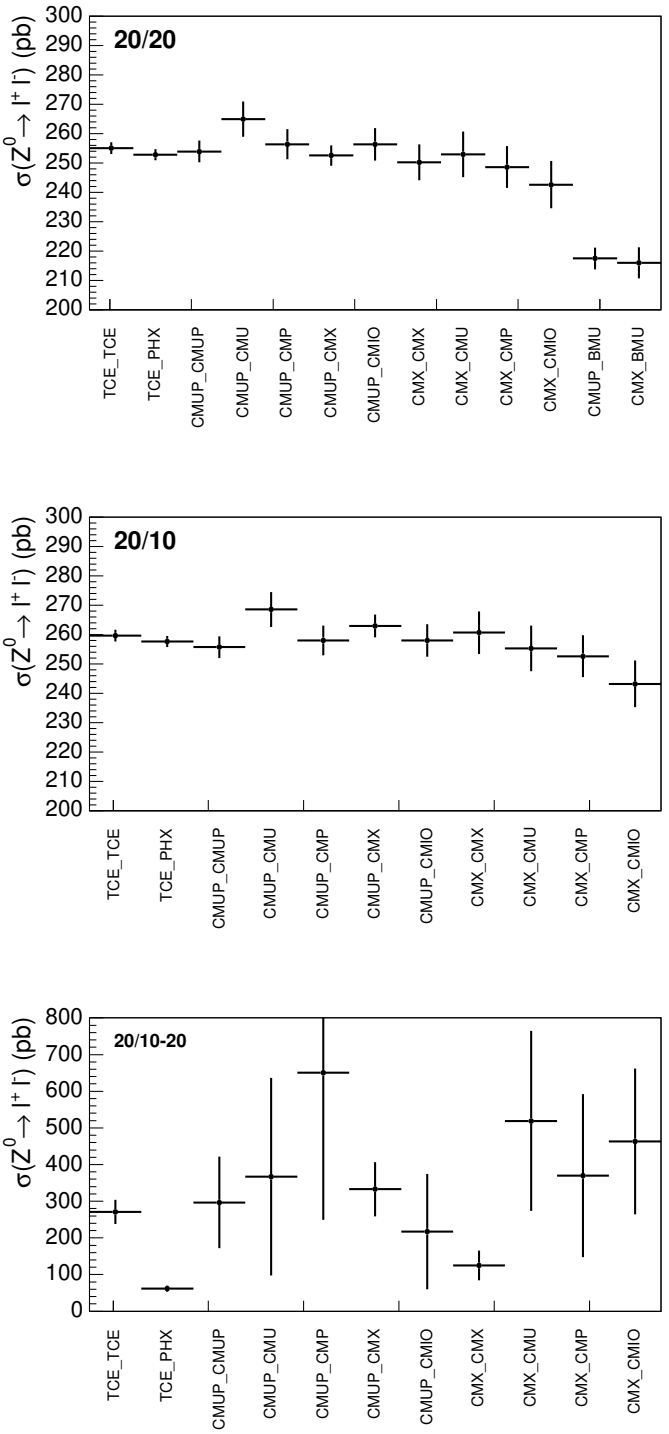

Figure 11: $\sigma(p\bar{p} \to Z^0) \times \mathrm{BR}(Z^0 \to l^+l^-)$ for each dilepton type. The top figure is for dileptons where both leptons have $p_t > 20$ GeV/c. The middle is for dileptons where one lepton satisfies $p_t > 20$ GeV/c and the other $p_t > 10$ GeV/c. The bottom figure is for dileptons where one lepton satisfies $p_t > 20$ GeV/c and the other $20 > p_t > 10$ GeV/c.

The results for the Z^0 cross section measurement are shown in Figure 11. The agreement across all combinations agree very well within the statistical errors with the exception of the BMU muons. The BMU cross sections are very low because of the missing alignment correction in the data for Stntuple and are not considered further. Taking the universal systematic uncertainty of 6% into account, the measurements agree with the NNLO calculation $\sigma(p\bar{p} \to Z^0) \times \mathrm{BR}(Z^0 \to \ell\ell) = 250.5 \pm 3.8$ pb.

Cross sections for combinations with SCMIO muons have been examined and are shown to disagree strongly with the rest of the cross sections. These are therefore also disregarded for the present analysis. The cross sections for one lepton having $p_t > 20$GeV/c and the other between 10 and 20GeV/c are not statistically powerful and no conclusions may be drawn from this check on the leptons in this range. There were so few events in the TCE-PHX and CMX-CMX combinations that the fits failed.

There are few events in the Drell-Yan production with one lepton having $p_t > 20$ GeV/c and the other with $10 < p_t < 20$ GeV/c; however, small shifts in the mean values are observed and these are added to the scale factor systematic uncertainties in the Higgs result.

Dilepton Type	σ_Z pb	σ_Z pb	σ_Z pb
Lepton2 Pt	20	10	10-20
TCE_TCE	255 ± 2	260 ± 2	271 ± 33
TCE_PHX	253 ± 2	258 ± 2	61 ± 9
CMUP_CMUP	254 ± 4	256 ± 4	300 ± 130
CMUP_CMU	265 ± 6	269 ± 6	370 ± 270
CMUP_CMP	256 ± 5	258 ± 5	650 ± 400
CMUP_CMX	253 ± 4	263 ± 4	330 ± 74
CMUP_CMIO	256 ± 6	258 ± 6	220 ± 160
CMX_CMX	250 ± 6	261 ± 7	125 ± 40
CMX_CMU	253 ± 8	255 ± 8	520 ± 250
CMX_CMP	249 ± 7	253 ± 7	370 ± 220
CMX_CMIO	243 ± 8	243 ± 8	463 ± 200
CMUP_BMU	218 ± 4		
CMX_BMU	216 ± 5		

Table 16: Summary of Z cross-section measurements for both lepton p_t above 20 GeV/c and for lepton p_t allowed to go as low as 10 GeV/c, and for one lepton above 20 GeV/c but the other between 10 and 20 GeV/c. Uncertainties are statistical only. A systematic uncertainty from luminosity of 6% is present for all measurements.

Dilepton Type	M_Z GeV/c^2	M_Z GeV/c^2
Lepton2 Pt	Data	MC
TCE_TCE	90.77 ± 0.03	91.107 ± 0.008
TCE_PHX	90.94 ± 0.04	91.114 ± 0.006
CMUP_CMUP	90.92 ± 0.05	90.960 ± 0.010
CMUP_CMU	90.90 ± 0.07	90.966 ± 0.014
CMUP_CMP	90.80 ± 0.07	90.928 ± 0.014
CMUP_CMX	90.86 ± 0.04	90.970 ± 0.009
CMUP_CMIO	90.80 ± 0.06	90.955 ± 0.016
CMX_CMX	90.88 ± 0.06	90.959 ± 0.015
CMX_CMU	90.92 ± 0.09	90.941 ± 0.019
CMX_CMP	90.75 ± 0.07	90.965 ± 0.018
CMX_CMIO	91.09 ± 0.09	90.959 ± 0.022
CMUP_BMU	90.89 ± 0.08	90.940 ± 0.019
CMX_BMU	90.76 ± 0.08	90.916 ± 0.023

Table 17: Summary of Z mass measurements for Data and Monte Carlo.

7 Event Selection: Cuts analysis

Index	Event Selection	Plot Before Cut
0	two leptons with ${p_T}^{\ell_{\text{trigger, non-trigger}}} > 20$, 10 GeV	
1	Isolation	
2	$M_{\ell\ell} > 16$ GeV	
3	nJets($E_T > 15$ GeV) $= 0$ || nJets($E_T < 55$) $= 1$ || nJets($E_T < 40$) $= 2$	X
4	opposite lepton charge signs	
5	$\not\!\!E_T > M_H/4$	X
6	$M_H > 150$ GeV || ($\not\!\!E_T > 50$ GeV || $\Delta\phi(\not\!\!E_T$, lep/jet) > 0.35)	
7	$M_{ll} < M_H/2 - 5$ GeV	X
8	${E_T}^{\ell_1} + {E_T}^{\ell_2} + \not\!\!E_T < M_H$	X

Table 18: Event Selection for the HWW analysis. Plot comparing data and Monte Carlo before a cut is applied may be found for the selections indicated with an "X".

Following the procedure in the previous analysis [1], a search for the contribution of $p\bar{p} \to H \to W^+W^- \to \ell^+\ell^-\nu\bar{\nu}$, where $\ell = e, \mu$ or τ and $\tau \to eX$ or $\tau \to \mu X$ to the dilepton cross section is performed by cutting on quantities that enhance the contribution of this process. After the selection of dileptons described in Section 4 the cuts in Table 18 are applied.

Isolation is applied as described in Section 4.1. 76% of the Higgs events for $M_h = 160$ GeV/c^2 are kept after this cut.

A cut on the lower bound of the $M_{\ell\ell}$ is applied to eliminate backgrounds from J/Ψ's, Upsilons and $b\bar{b}$. 96% of the Higgs events for $M_h = 160$ GeV/c^2 are kept after this cut.

The distribution of the computed sources of dilepton events at this stage in the analysis is compared to the data in Figures 12 and in Figure 13, in the graph labelled "Number of Jets in before Jet cut". The contribution from the Higgs is computed for $M_h = 160$ GeV/c^2. Similar graphs for the Higgs-mass depenent cuts are available in Figures 47 to 55.

The jet veto is applied to tight jets: *reclustered* jets with the JetClu 0.4 algorithm using the primary vertex and excluding towers from TCE and PHX isolated electrons, with corrected $E_T > 15$ GeV and $|\eta| < 2.5$. We correct jets using level 5 corrections. The high jet E_T threshold used increases our signal acceptance without significantly impacting our backgrounds. Only the events with 0, 1 and 2 jets, with further energy requirements, are selected. 87% of the Higgs events for $M_h = 160$ GeV/c^2 are kept after this cut.

The leptons are required to have opposite sign and trileptons are rejected. 99% of the Higgs events for $M_h = 160$ GeV/c^2 are kept after this cut.

The distribution of the computed sources of dilepton events at this stage in the analysis is compared to the data in Figure 13, in the graph labelled "Missing Et before missing et cut". The contribution from the Higgs is computed for $M_h = 160$ GeV/c^2. Similar graphs are available for the remaining Higgs masses in Figures 47 to 55.

Significant missing energy is expected in the Higgs contribution to dileptons while it should be small for the Drell-Yan process. Therefore a cut on the missing energy is applied. 80% of the Higgs events for $M_h = 160$ GeV/c^2 are kept after this cut.

For dilepton pairs having a mass below $M_h = 150$ GeV/c^2, the missing energy is required in addition to be larger than 50 GeV/c^2 or there should be a large angle between the missing energy or the closest lepton or jet.

The distribution of the computed sources of dilepton events at this stage in the analysis is compared to the data in Figure 13 in the graph labelled "dilepton mass before dilepton mass cut". The contribution from the Higgs is computed for $M_h = 160$ GeV/c^2. Similar graphs are available for the remaining Higgs masses in Figures 47 to 55.

An M_h-dependent upper bound on the dilepton mass pair is placed on the dilepton mass. 97% of the Higgs events for $M_h = 160$ GeV/c^2 are kept after this cut.

The distribution of the computed sources of dilepton events at this stage in the analysis is compared to the data in Figure 13 in the graph labelled "total Et before total et cut". The contribution from the Higgs is computed for $M_h = 160$ GeV/c^2. Similar graphs are available for the remaining Higgs masses in Figures 47 to 55.

Finally, an M_h-dependent cut on $H_t \equiv {E_T}^{\ell_1} + {E_T}^{\ell_2} + \not\!\!E_T$ is applied. 99% of the Higgs events for $M_h = 160$ GeV/c^2 are kept after this cut.

Events passing these cuts are then used in the fits of the $\Delta\phi(\ell, \ell)$ distributions, discussed later.

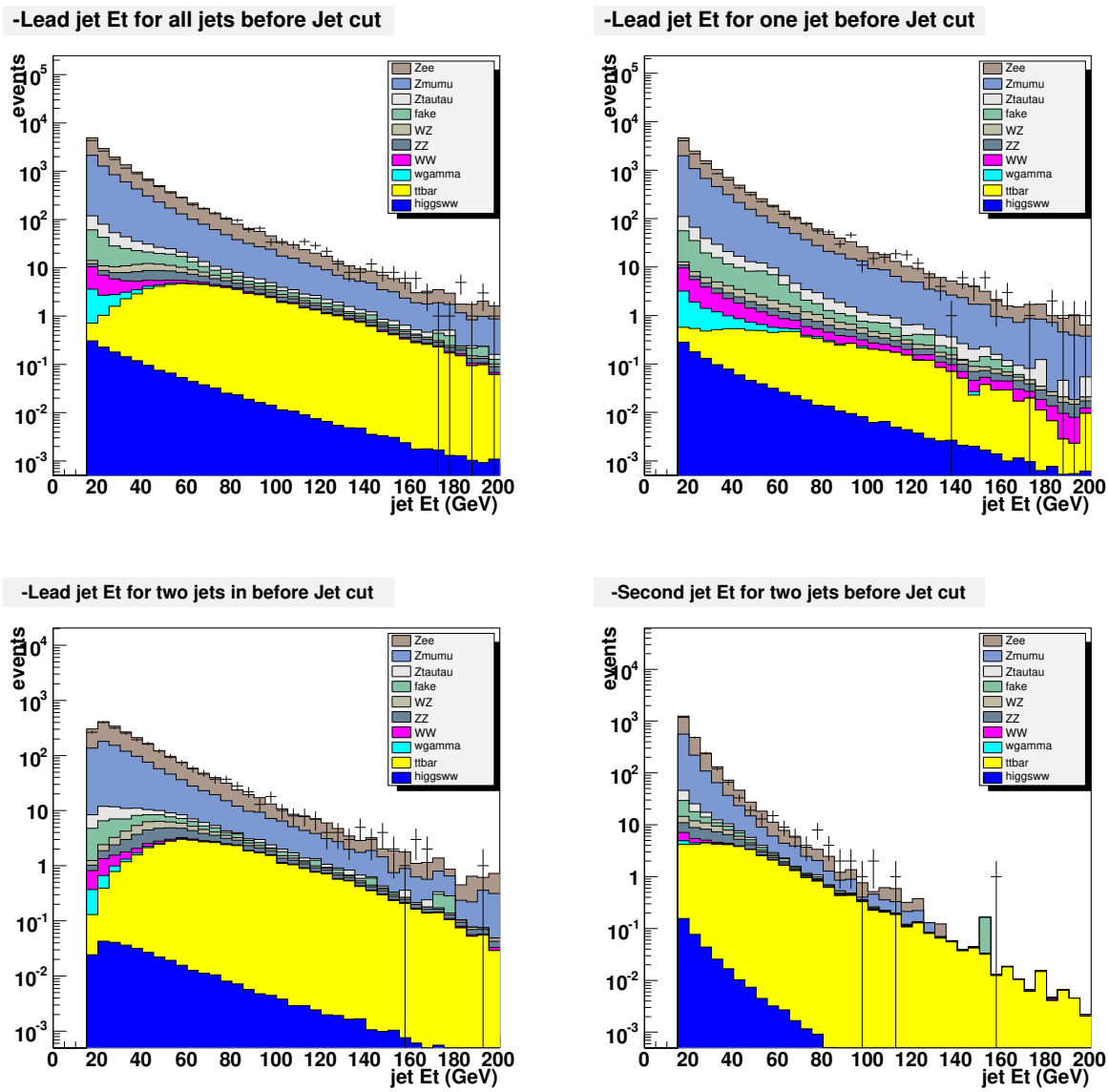

Figure 12: Jet variables used in the event selection (for $M_H = 160$ GeV) are shown before cutting on the Jets. (upper-left) Jet Et for any number of Jets, (upper-right) Jet Et for events with 1 jet, (lower-left) Leading Jet Et for events with 2 jets, and (lower-right) sub-leading Jet Et for Events with 2 jets.

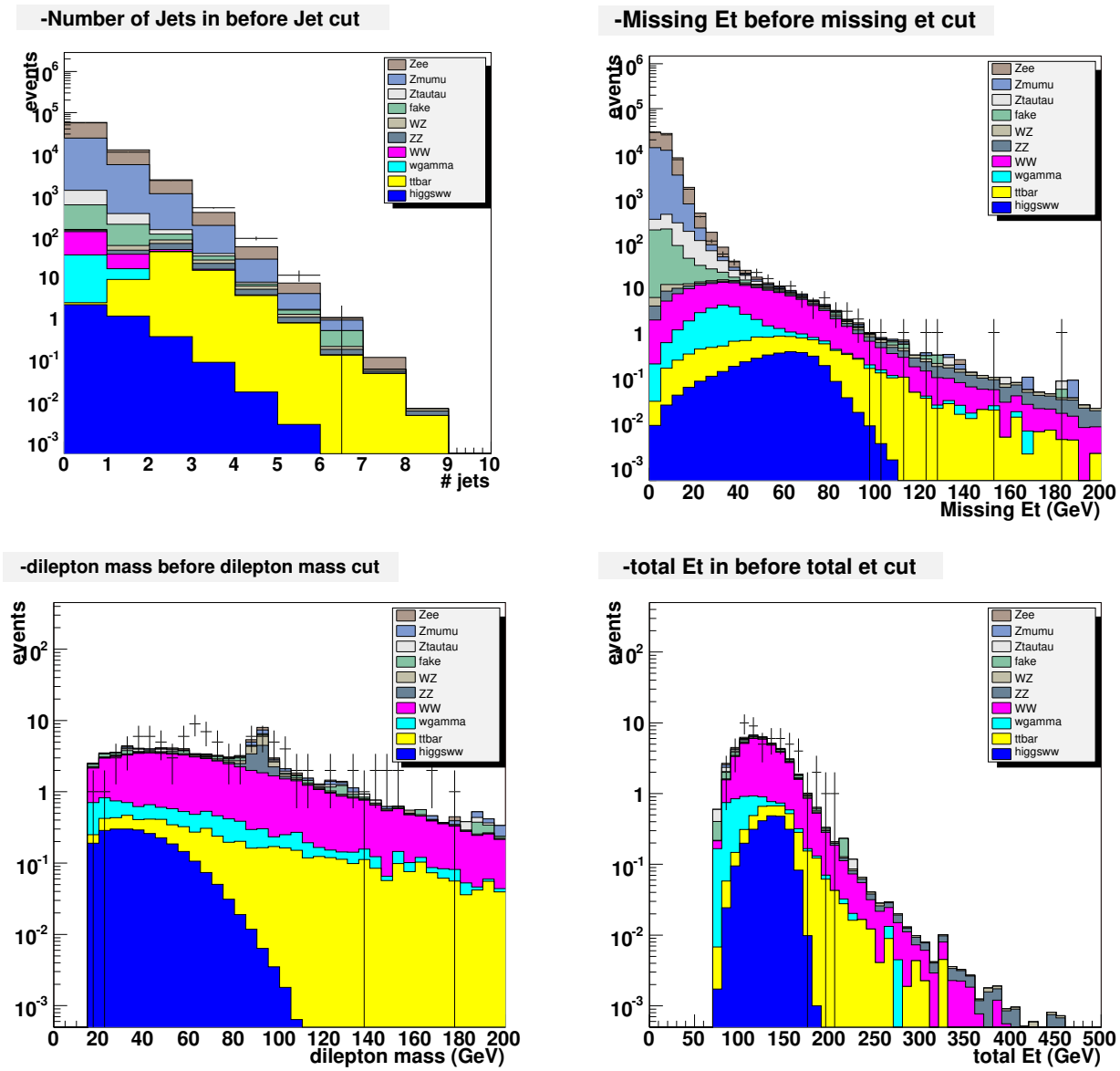

Figure 13: Four of the variables used in the event selection (for $M_H = 160$ GeV) are shown before cutting on that variable: (upper-left) number of jets; (upper-right) missing energy; (lower-left) dilepton invariant mass and (lower-right) $P_T(lep1) + P_T(lep2)+\not\!\!E_T$.

After all cuts, 43.9% of the dilepton events reconstructed in the Higgs contribution are kept. Detailed numbers for events surving each cut for each Higgs mass, dilepton category, run period and source of dileptons are given in Section C. The acceptance for $p\bar{p} \to H \to W^+W^- \to \ell^+\ell^-\nu\bar{\nu}$, where $\ell = e, \mu$ or τ and $\tau \to eX$ or $\tau \to \mu X$. is summarized in Fig 14 for the dilepton selection and afster all cuts are applied.

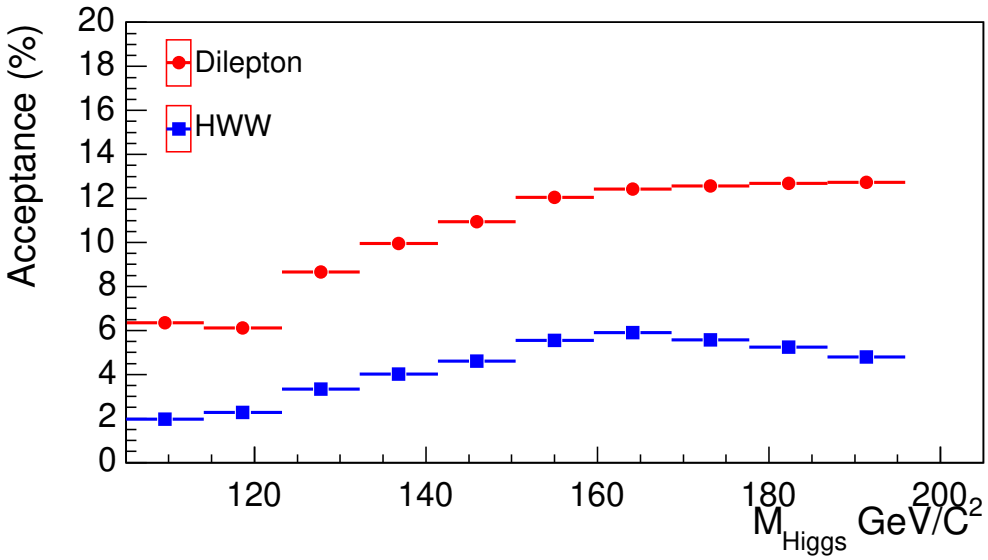

Figure 14: Signal acceptance for various Higgs masses. The dilepton selection efficiency is shown as well as the efficiency after all cuts.

Table ?? shows the detailed signal efficiencies after every single cut, for a Higgs mass of 160 GeV/c^2.

The impact of the cuts on all the other sources of dileptons are now considered.

- WW Table ??, for $M_H = 160$ GeV criteria. The cuts $M_{\ell\ell} < M_H/2$ and requiring large missing energy are relatively effective on reducing the inclusive WW dilepton contribution.
- $t\bar{t}$ Acceptance of the $t\bar{t}$ through each of the cuts for HWW search is in Table ??, for $M_H = 160$ GeV criteria. The 0-jet cut is very effective in reducing the $t\bar{t}$ contribution to dileptons. Generall, jets are a very good discriminant against $t\bar{t}$.
- **Drell-Yan** Acceptance of the DY ll dielpton source through each of the cuts for HWW search is in Table ??, for $M_H = 160$ GeV criteria. The cut on missing energy discriminates strongly between this source of dileptons and the Higgs mediated production of dileptons.

The same scale factors used in the measurement of the Z^0 cross section were applied to the Higgs Monte Carlo.

8 Acceptance Systematic Uncertainties

Potential sources of systematic uncertainty on the prediction of the acceptance for the various sources of dileptons are considered here.

8.1 General Algorithms

The computation of the systematic uncertainties is closely coupled with the treatement of errors in the fitting procedures described in Section 10. The $\Delta\phi_{ll}$ serves to emphasize the contribution of the $H \to WW \to l^+l^-\nu\bar{\nu}$ to the dileptons when after the cuts described in Section 7 are applied. Hence this distribution is fit for a contribution of the Higgs intermediated production of W pairs. In doing the fit, the contribution of each process described in 3.1 is computed. For each of the systematic uncertainties considered, events are added or depleted from the $\Delta\phi_{ll}$ as a result of the impact of the uncertainty on the parameters that describe the event. This change in the number of events is implemented by changing the weight of the events as a function of the parameters of the events. The fractional maximum change in the weight of the event relative to the nominal weight computed as described in Section 6.2 gives an upwards variation. Hence for a weight w_0 that is varied to a new larger value w^+, or a smaller value, w^- the variation is given by:

$$w^+ = \frac{w_{max} - w_0}{w_0} + w_0 \tag{2}$$

$$w^- = w_0 - \frac{w_0 - w_{min}}{w_0} \tag{3}$$

$$\tag{4}$$

This is computed for each bin and is put into the fit described in Section 10 in a variety of ways.

The following sections describe the general ways in which the systematic uncertaintes affecting various processes are computed. Following this is a description of additional uncertainties peculiar to specific dilepton production modes.

8.2 PDF Uncertainty

The pdf uncertainties using the recommended Hessian method [7] also described on the Joint Physics webpage [8] and in [9]. With the new PDF set CTEQ6M, the CTEQ group made available 40 complementary PDF sets CTEQ6M.01...CTEQ6M.40, each of which represents an up/down variation along one of the twenty eigenvectors (corresponding to 20 free parameters used in the fit). They form an orthonormal basis set spanning the full PDF parameter space [5]. Each up and down variation pair represents the range of PDF behavior that is consistent with the current global data used in the fit.

The acceptance systematic prescription use is that given in [7] and clarified in equations 5-7 of CDF 7051 [10]. This requires computing the sum of the weights for all events for each PDF set. To do the summing in quadrature, it is necessary to take Equation 7 of CDF 7051 and plug in AC(A,i) in as the observable, where A= parton set number and i=bin of $\Delta\phi_{ll}$. For a given bin, the uncertainty is given by the "master equation" (Eq 38) of [9] which is the same on the Joint Physics web page [8]. The weights for equation Equation 5 of CDF 7051 are stored in a 46-bin histogram for the events that fail the dilepton selection. For events that are selected, all 46 weights are stored for each event. Those weights are then and added to 46-bin histogram for the dielepton events which are not selected and summed according to Equation 6 of CDF 7051 for those that are accepted. For each bin in $\Delta\phi_{ll}$ there are the 40 variations of the eigenvectors and the master equation is applied to determine the up and down systematics. Plots of the changes in the contribution of the various processes leading to dileptons are given in Figure 15.

8.3 α_s

The impact of α_s comes as part of the PDF variation studies. While there are 20 eigenvectors giving 40 variations, there are also variations for α_s avaiable in the full set of 46 variations. This was included in the fitting using the method described for 8.1. Plots of the changes in the contribution of the various processes leading to dileptons are given in Figure 16.

8.4 Initial State Radiation

Pythia was run with variations in Parp(62), Parp(64) and Parp(91) for the processes $gg \to H^0$, $p\bar{p} \to W^+W-$ and $p\bar{p} \to Z^0$. The variations were based on those found in CDF 7332 [11] and are given in Table 19. The method is that of cdf7332 (sections V B and V G). The parameters are varied in pythia and the resulting Z pt distribution compared to the Run I measurement [12]. A χ^2 is formed and central and 3-sigma values found. Variations used are slightly larger than in the most recent version of the CDF Note. The results are shown in Figures 17, 18 and 19. The

parp	Description	minus	central	plus
62	K_t cutoff in initial Parton shower	0.7	1.15	1.6
64	Q^2 =PARP(64)$\times k_t^2$ for $\alpha_s(Q^2)$ in parton shower	0.2	0.32	0.4
91	Gaussian width of primordial parton k_t distribution	1.4	1.9	2.4

Table 19: Pythia parameter variations used in computation of the ISR sysetmatic uncertainties.

dominant variation was seen in Parp(64) and hence this was taken in the reweighting method described in 8.1. Plots of the changes in the contribution of the various processes leading to dileptons are given in Figure 20.

8.5 Jet Energy Scale

To estimate the systematic uncertainty associated with the jet energy scale, the prescription for variations described in [29] are used as implemented in the JetUser package. A histogram of $\Delta\phi_{ll}$ for the upward and downward variation is saved for use with the fitting procedure. Plots of the changes in the contribution of the various processes leading to dileptons are given in Figure 21.

8.6 Trigger efficiency, Lepton ID, including Isolation

Using the trigger efficiency, identification and reconstruction efficiencies scale factors (data/MC) shown in Table 13 which include the Isolation cuts, histograms of $\Delta\phi_{ll}$ are made for these variations and used in the fitter. Plots of the changes in the contribution of the various processes leading to dileptons are given in Figure 22.

8.7 Lepton Energy Scale

The largest deviation in the Z mass is 0.3 GeV/c^2. This shift in scale is used to change the lepton p_t and the missing energy is recomputed as well. The change in the acceptance is then computed. A histogram of $\Delta\phi_{ll}$ for the variation is saved for use with the fitting procedure. Plots of the changes in the contribution of the various processes leading to dileptons are given in Figure 23.

8.8 Systematic Uncertainties Peculiar to Specific Processes

- The dependence of the acceptance on MC generator for $t\bar{t}$ is taken as 6% and was determined in the context of top dilepton analysis [36].

- For Wγ we use an uncertainty due to the events unweighting and K-factor error, described in [33], page 14.

- Since the Drell-Yan acceptance is impacted so strongly by the missing energy, there is concern about the simulation of missing energy and hence the sensitivity of the cut. The

ratio of missing energy cut efficiency for data and MC for various thresholds is studied. The numbers agree well within the errors. A systematic uncertainty do to this cut is added.

- $\frac{\epsilon_{data}}{\epsilon_{MC}} = 0.92 \pm 0.06$, for $\not\!\!E_T > 20$ GeV
- $\frac{\epsilon_{data}}{\epsilon_{MC}} = 1.02 \pm 0.15$, for $\not\!\!E_T > 30$ GeV
- $\frac{\epsilon_{data}}{\epsilon_{MC}} = 1.13 \pm 0.13$, for $\not\!\!E_T > 40$ GeV

- Similarly the cut on the jets was varied and compared in MC and Data.

The average systematic uncertainties on the acceptance for all processes leading to dileptons are given in Table 20. This is computed by taking the average deviation over all the bins in the $\Delta\phi_{ll}$ plots.

Figure 15: Variation in the $\Delta\phi_{ll}$ plot due to PDF changes

Figure 16: Variation in the $\Delta\phi_{ll}$ plot due to α_s changes.

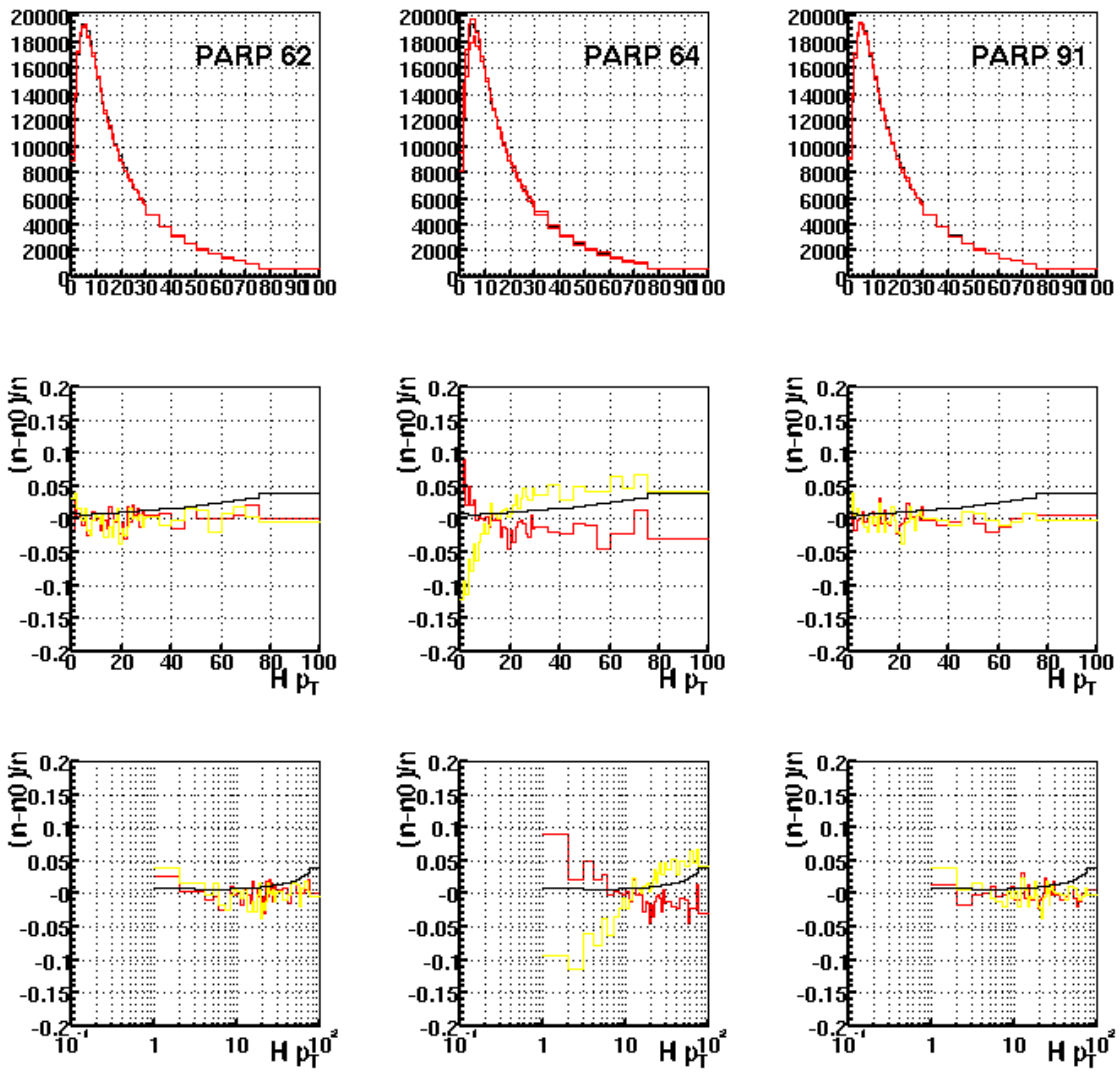

Figure 17: Variation of the p_t spectrum of the Higgs in $gg \to H^0$. The spectra are shown for variations of three of the pythia parameters in the top row of plots. The difference with respect to the default is shown as a function of p_t in the second and third row of plots.

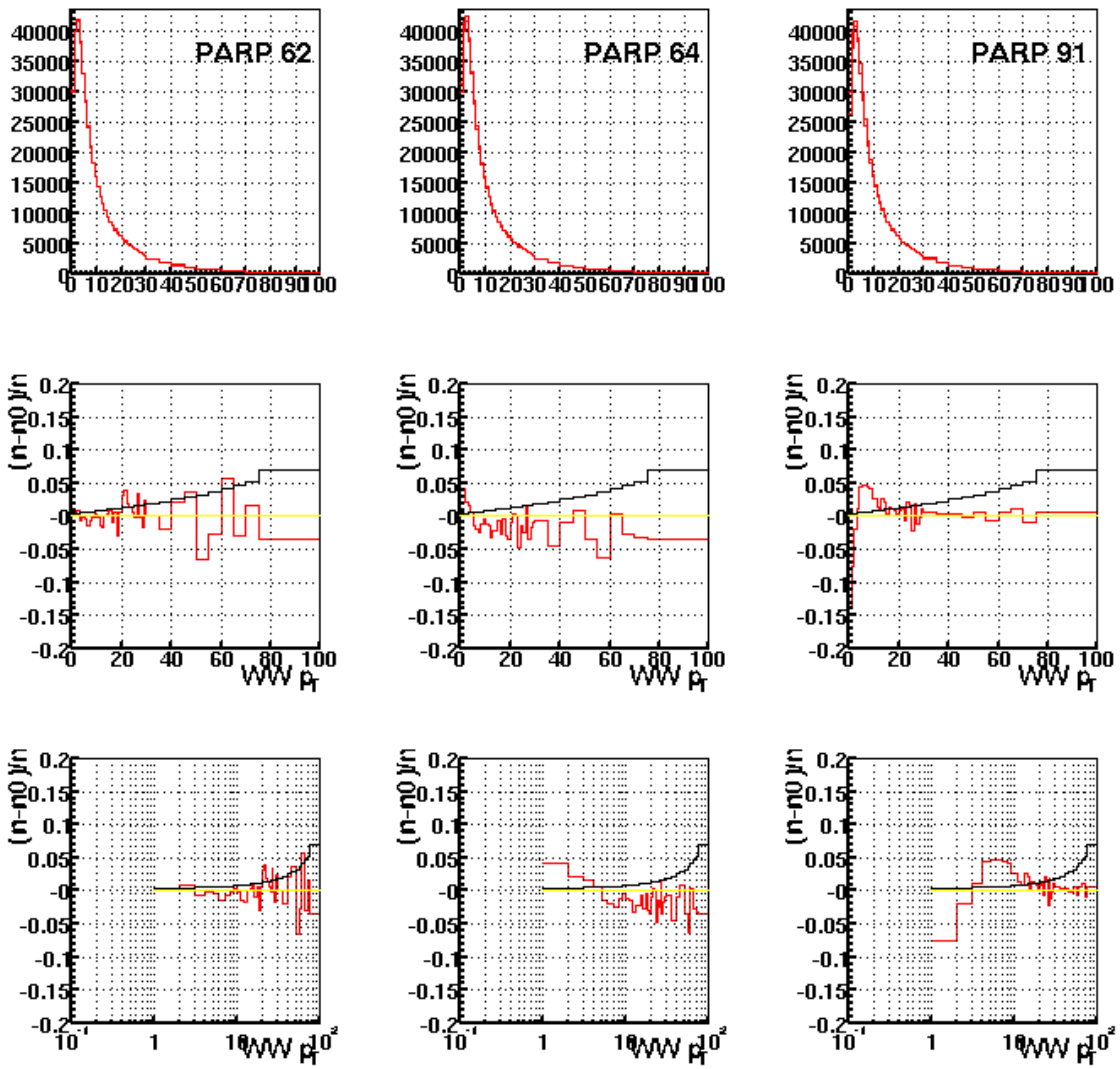

Figure 18: Variation of the p_t spectrum of WW production. The spectra are shown for variations of three of the pythia parameters in the top row of plots. The difference with respect to the default is shown as a function of p_t in the second and third row of plots.

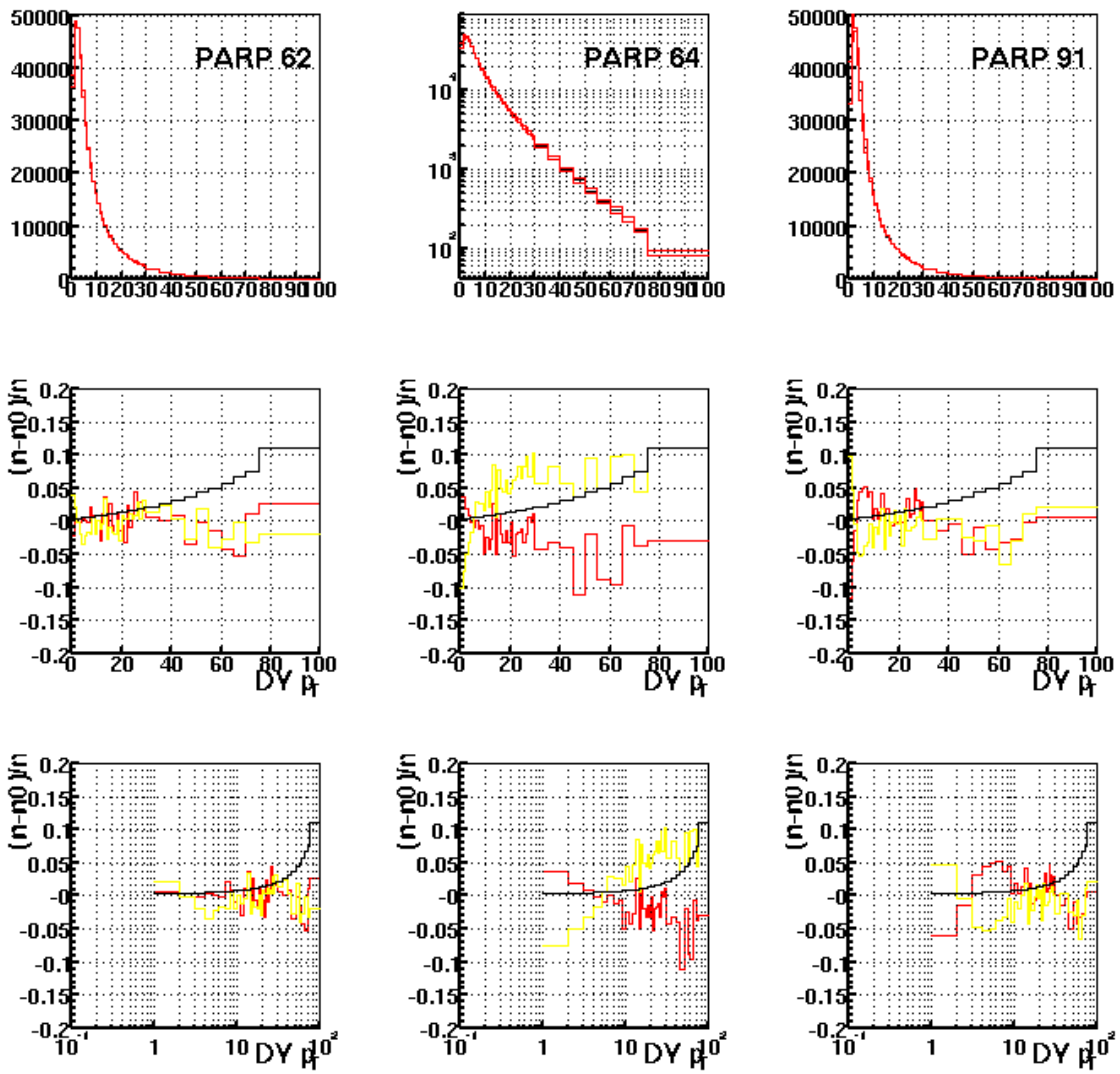

Figure 19: Variation of the p_t spectrum of the Higgs in Z^0 production. The spectra are shown for variations of three of the pythia parameters in the top row of plots. The difference with respect to the default is shown as a function of p_t in the second and third row of plots.

Figure 20: Variation in the $\Delta\phi_{ll}$ plot due to ISR changes.

Figure 21: Variation in the $\Delta\phi_{ll}$ plot due to Jet Energy Scale changes.

Figure 22: Variation in the $\Delta\phi_{ll}$ plot due to changes in the trigger efficiency and lepton reconstruction and id scale factors.

Figure 23: Variation in the $\Delta\phi_{ll}$ plot due to Lepton energy scale changes.

Dilepton Process	Source	Uncertainty(%) 7708	Ave
Higgs	ISR	3	
	α_s	3	
	PDF Acceptance	3	
	Jet Energy Scale	1	
	Lepton ID	2	
	Track Isolation	2	
	Trigger Efficiency	1	
Higgs	**Total**	**6**	
WW	Jet Veto ("jet modeling")	6	
	PDF/Q^2 Effect on $\sigma(WW)$	5	
	Generator/Parton Shower Model	4	
	Lepton ID SF	2	
	Jet Energy Scale	1	
	PDFs on Acceptance	1	
	Track Isolation	2	
	Trigger Efficiency	1	
WW	**Total**	**9**	
WZ/ZZ	**Total** (same as WW)	**9**	
Fakes	Different Jet Samples	**50**	
$t\bar{t}$	Lepton ID SF	2	
	Jet Energy Scale	5	
	MC Generators (Pythia vs Herwig)	6	
	PDF's	1	
	ISR/FSR	2	
$t\bar{t}$	**Total**	**8**	
Drell-Yan	Jet Energy Scale	1	
	Lepton ID SF	2	
	Track Isolation	2	
	PDF on Acceptance	2	
	Trigger Efficiency	1	
	Missing Energy Data/MC	20	
Drell-Yan	**Total**	**20**	
W γ	Factorization scale	2	
	Renormalization scale	3	
	PDF	5	
	Jet Energy Scale	1	
	Unweighting and k-factor error	2	
W γ	**Total**	**7**	

Table 20: Sources of systematic uncertainties on the backgrounds. In addition there is a common systematic of 6% coming from luminosity.

9 Grand Summary

The result of the event selection described in Section 2, applied to the datasets described above, are shown in Tables 21, 22, 32-41. The contribution of the Higgs process depends on the particular mass of the Higgs boson.

The summary of all the backgrounds, signal acceptances, and data analysis for 1fb^{-1}are shown in Table 21 and 22. Tables 34-39 show the distributions of the signal and backgrounds per ee, $e\mu$ and $\mu\mu$ channels.

M_H	110	120	130	140	150
WW	10.432+-3.230	14.372+-3.791	18.225+-4.269	21.502+-4.637	23.944+-4.893
WZ	0.392+-0.626	0.536+-0.732	0.677+-0.823	0.805+-0.897	0.911+-0.954
ZZ	0.215+-0.464	0.259+-0.509	0.296+-0.544	0.327+-0.572	0.353+-0.594
ttbar	0.260+-0.510	0.374+-0.612	0.606+-0.778	0.772+-0.879	0.970+-0.985
wgamma	6.629+-2.575	6.111+-2.472	5.440+-2.332	4.555+-2.134	3.711+-1.926
DYll	9.504+-3.083	7.751+-2.784	5.564+-2.359	4.598+-2.144	3.402+-1.845
Background Total	27.433+-5.238	29.403+-5.422	30.807+-5.550	32.560+-5.706	33.292+-5.770
higgsww	0.115+-0.339	0.309+-0.556	0.784+-0.885	1.301+-1.140	1.729+-1.315
data	35	37	37	40	44

Table 21: The estimated backgrounds and HWW signal in 1fb^{-1}, and the number of events observed in the data, for each of the dilepton categories. The HWW expectation uses the theoretical cross-sections and BRs discussed in Section 1. The error on luminosity (6%) it is not included.

M_H	160	170	180	190	200
WW	25.443+-5.044	25.910+-5.090	25.501+-5.050	24.564+-4.956	23.231+-4.820
WZ	0.991+-0.996	1.056+-1.028	1.143+-1.069	1.589+-1.261	2.385+-1.544
ZZ	0.377+-0.614	0.419+-0.647	0.525+-0.725	1.169+-1.081	2.384+-1.544
ttbar	1.198+-1.095	1.409+-1.187	1.626+-1.275	1.772+-1.331	1.866+-1.366
wgamma	2.986+-1.728	2.412+-1.553	2.042+-1.429	1.660+-1.288	1.307+-1.143
DYll	2.895+-1.701	2.358+-1.536	2.116+-1.455	2.495+-1.579	3.196+-1.788
Background Total	33.890+-5.822	33.564+-5.793	32.954+-5.741	33.248+-5.766	34.369+-5.862
higgsww	2.241+-1.497	2.114+-1.454	1.592+-1.262	1.036+-1.018	0.767+-0.876
data	47	47	48	48	44

Table 22: The estimated backgrounds and HWW signal in 1fb^{-1}, and the number of events observed in the data, for each of the dilepton categories. The HWW expectation uses the theoretical cross-sections and BRs discussed in Section 1. The error on luminosity it is not included.

10 Cross-Section Limit Calculation

The senstitivity of this analysis to the contribution of the higgs production to the measurement of dilepton final states is studied here and a 95% credibility limits (C.L.) on the Standard Model $\sigma \times BR(p\bar{p} \to H \to WW^*)$ is extracted.

10.1 $\Delta\phi$ Distributions

The distributions of $\Delta\phi$ between the 2 leptons in events passing the selection criteria described in Section 7 are used to set limits on the $p\bar{p} \to H \to WW^*$ cross section. These distributions are given in Figures 25-34. The scalar nature of the Higgs boson gives a tendency of the leptons to be closer in ϕ than that from WW production, making this variable a good discriminator. Rather than simply cut on the variable (and hence lose some signal acceptance), a binned likelihood of the observed spectrum to a combination of signal and background, and use this to extract cross section limits. The results of the analysis are given in Tables 23 and 24 and shown graphically in Figure 24. For the figure, the results have been scaled to the NNLO computations of $\sigma(gg \to H^0) \times \mathrm{BR}(H^0 \to W^+W^-)$ shown in Table 1. A description of the methods indicated in each row are discussed here.

The procedure used is discussed in detail in the previous version of this analysis [1]. A second similiar Bayesian method is also used and a corresponding frequentist menthod has also been employed [37]. For this method 1000 pseudo experiments are performed. In addition, the treatement of systematic uncertainties has been treated in a variety of ways. Finally, ee, eμ, and $\mu\mu$ dileptons have been treated separately since the unlike flavor dileptons are not subject to Drell-Yan contributions and the systematics for electrons and muons differ. In the "7708 method", the average systematic uncertainties in the expected number of events for all sources are added in quadrature with the statistical uncertainties and the fluctuations of the pseudoexperimental statistics is based on this. In the "Tom Style" method, the average of the systematic uncertainties are allowed to vary within their bounds. For both the "7708 method" and "Tom Style", the systematic uncertainties determined in the previous analysis [1] were used. For the "emu" fitting, the histograms of the upwards and downwards variations for each bin and systematic are treated in the pseudoexperiments. The values determimined in this analysis were used. In each case expected and actual limits are given.

In all these cases four histogram categories are used: the data, WW, Higgs and remaining contributions to dileptons. The number of histograms depends on the details of the differences in the methods with many histograms used in the "Tom Style". The luminosity systematic is handled as a separate error in all cases.

The results do not vary considerably for any of these methods; however, there is a signficant excess in the data over the predicted backgrounds.

M_H	110	120	130	140	150
7708 expected limit	5.328	4.868	3.413	2.903	2.495
7708 actual limit	9.025	7.575	4.875	3.775	3.475
Tom expected tomstyle on TomdilDphi, frequentist	5.949	5.470	3.981	3.459	2.978
Tom actual tomstyle on TomdilDphi, frequentist	10.221	8.623	5.404	4.084	3.501
Tom expected tomstyle Bayes on TomdilDphi	6.086	5.771	4.105	3.487	3.020
Tom actual tomstyle Bayes on TomdilDphi	10.275	8.823	5.571	4.302	3.822
Tom expected emu Bayes	5.810	5.509	3.991	3.397	2.851
Tom actual emu Bayes	10.340	8.628	5.450	4.247	3.715

Table 23: Results of the cuts analysis for various fitting procedures and handling of systematic uncertainties

M_H	160	170	180	190	200
7708 expected limit	2.050	1.966	2.104	2.250	2.533
7708 actual limit	3.275	3.325	4.125	4.875	4.375
Tom expected tomstyle on TomdilDphi, frequentist	2.362	2.255	2.448	2.618	2.815
Tom actual tomstyle on TomdilDphi, frequentist	3.400	3.407	4.427	5.590	5.102
Tom expected tomstyle Bayes on TomdilDphi	2.397	2.278	2.501	2.734	2.887
Tom actual tomstyle Bayes on TomdilDphi	3.557	3.632	4.738	5.640	5.069
Tom expected emu Bayes	2.304	2.197	2.329	2.519	2.823
Tom actual emu Bayes	3.508	3.546	4.471	5.348	4.813

Table 24: Results of the cuts analysis for various fitting procedures and handling of systematic uncertainties

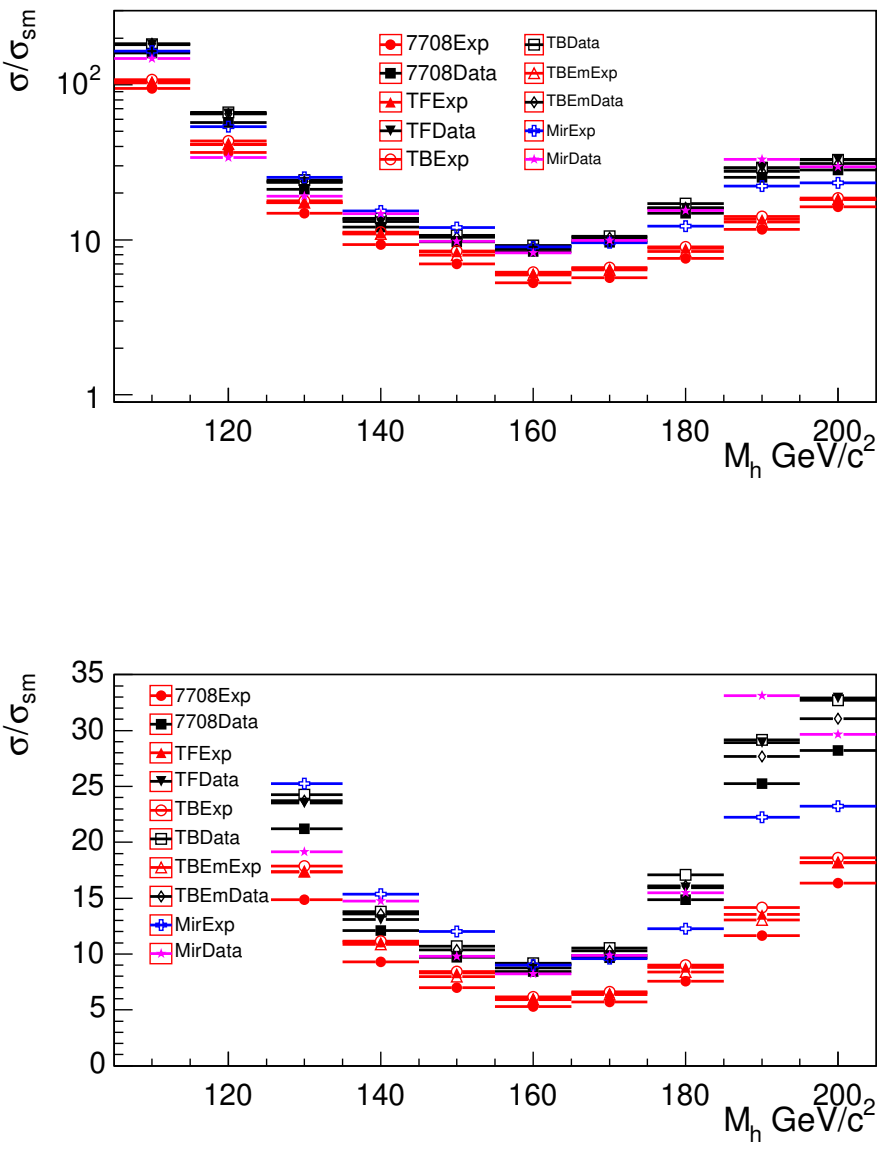

Figure 24: Expected (red) and Actual (black) limits for $\sigma(gg \to H^0) \times \mathrm{BR}(H^0 \to W^+W^-)$ relative to that expected in the NNLO computation of Table 1. The blue points are taken from CDF7708 for the expected limits and the magenta points for the actual limits in CDF7708.

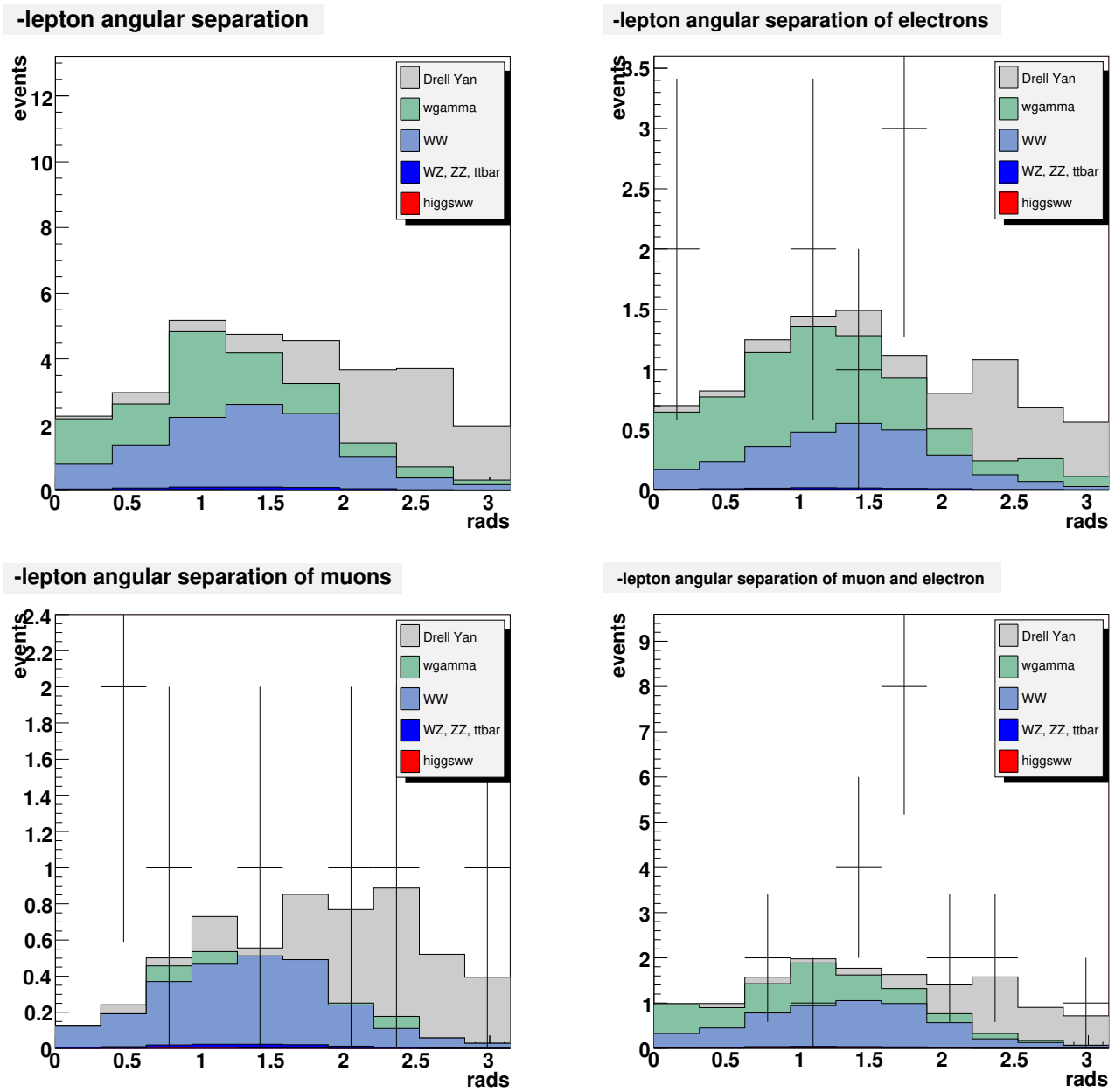

Figure 25: Azimuthal angular separation between the leptons, $\Delta\phi(\ell,\ell)$, from the decay of $H \rightarrow WW^* \rightarrow \ell\nu\ell\nu$. Distributions of data, HWW^* signal ($M_H = 110$ GeV) MC, WW MC and the sum of other considered background MC samples are shown. The MCs are normalized to the expectations for the integrated luminosity for analyzed data of 1fb^{-1}. We use the upper-left $ee + e\mu + \mu\mu$ plot to fit for a limit on the cross-section of SM HWW production at Tevatron, at the Higgs mass of $M_H = 110$ GeV.

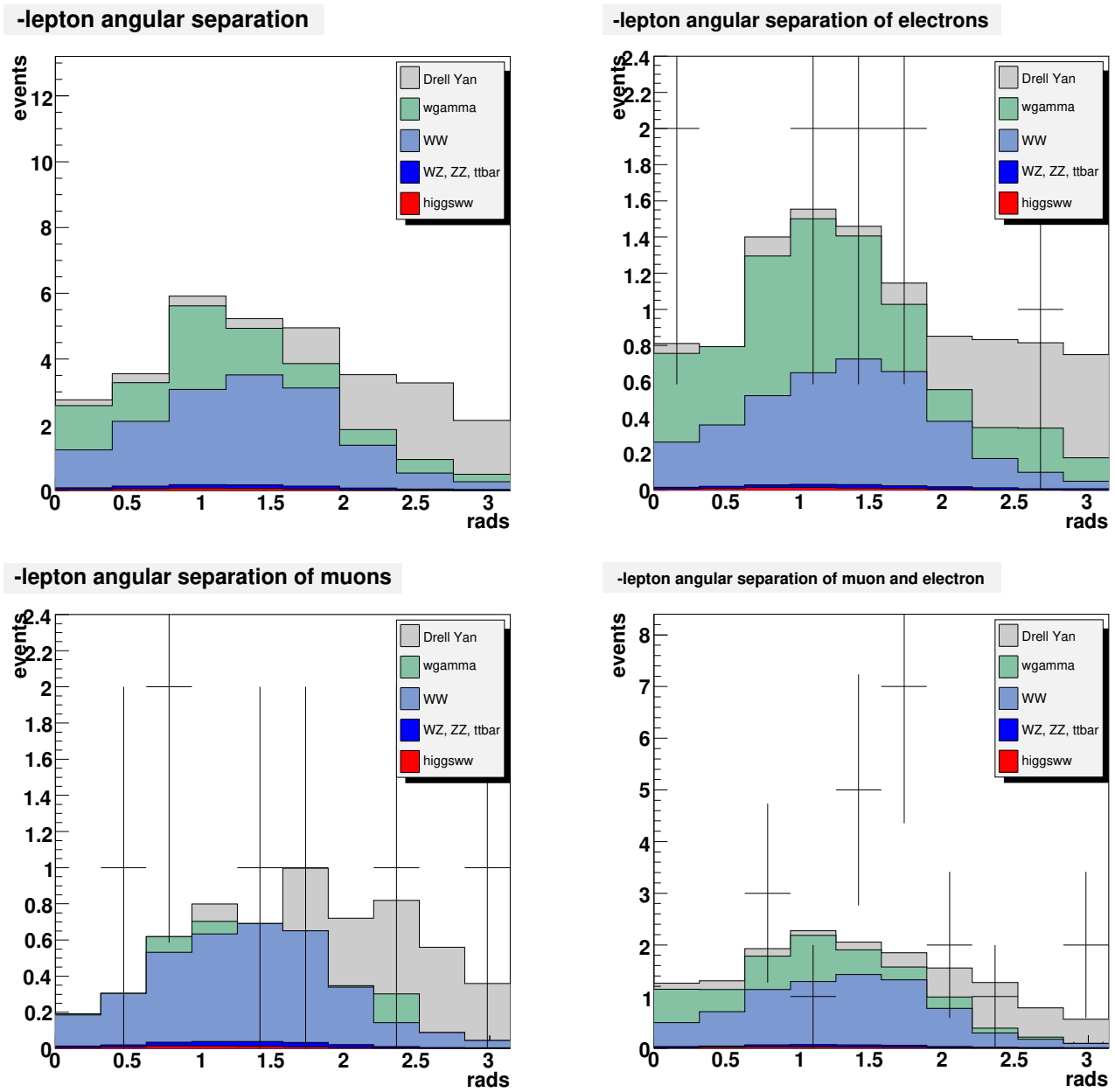

Figure 26: Azimuthal angular separation between the leptons, $\Delta\phi(\ell,\ell)$, from the decay of $H \to WW^* \to \ell\nu\ell\nu$. Distributions of data, HWW^* signal ($M_H = 120$ GeV) MC, WW MC and the sum of other considered background MC samples are shown. The MCs are normalized to the expectations for the integrated luminosity for analyzed data of 1fb^{-1}. We use the upper-left $ee + e\mu + \mu\mu$ plot to fit for a limit on the cross-section of SM HWW production at Tevatron, at the Higgs mass of $M_H = 120$ GeV.

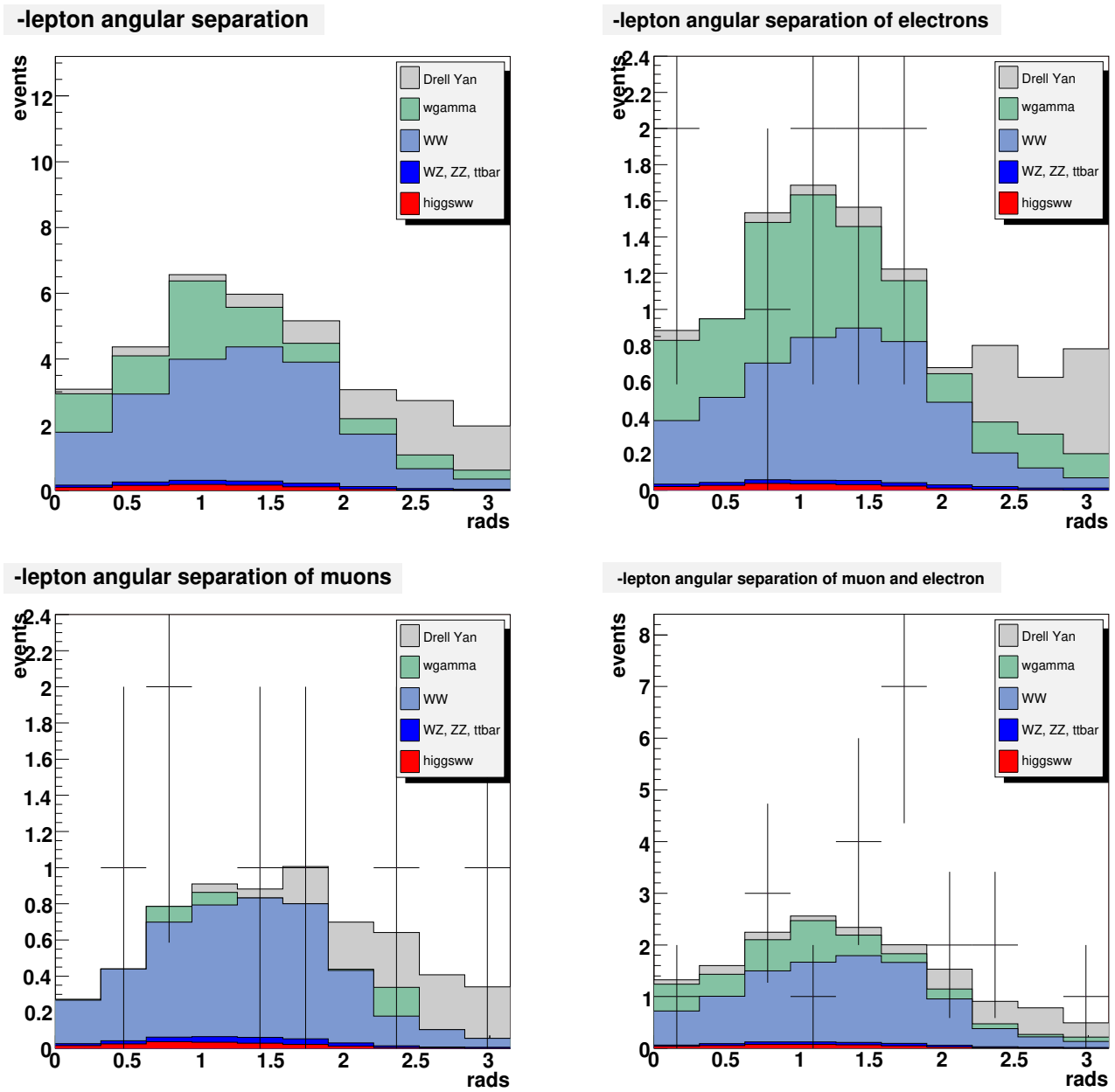

Figure 27: Azimuthal angular separation between the leptons, $\Delta\phi(\ell,\ell)$, from the decay of $H \to WW^* \to \ell\nu\ell\nu$. Distributions of data, HWW^* signal ($M_H = 130$ GeV) MC, WW MC and the sum of other considered background MC samples are shown. The MCs are normalized to the expectations for the integrated luminosity for analyzed data of 1fb^{-1}. We use the upper-left $ee + e\mu + \mu\mu$ plot to fit for a limit on the cross-section of SM HWW production at Tevatron, at the Higgs mass of $M_H = 130$ GeV.

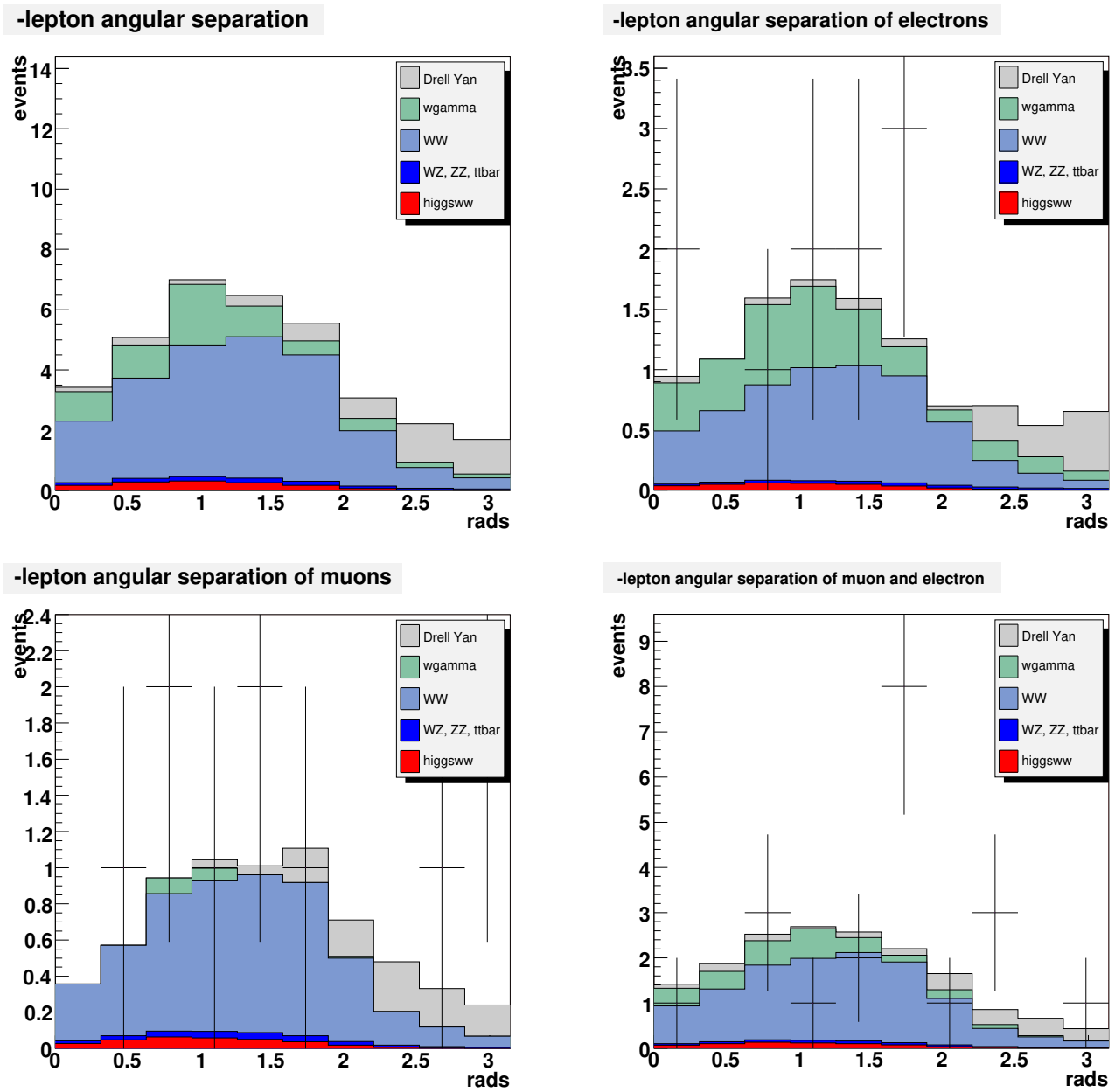

Figure 28: Azimuthal angular separation between the leptons, $\Delta\phi(\ell,\ell)$, from the decay of $H \to WW^* \to \ell\nu\ell\nu$. Distributions of data, HWW^* signal ($M_H = 140$ GeV) MC, WW MC and the sum of other considered background MC samples are shown. The MCs are normalized to the expectations for the integrated luminosity for analyzed data of 1fb^{-1}. We use the upper-left $ee + e\mu + \mu\mu$ plot to fit for a limit on the cross-section of SM HWW production at Tevatron, at the Higgs mass of $M_H = 140$ GeV.

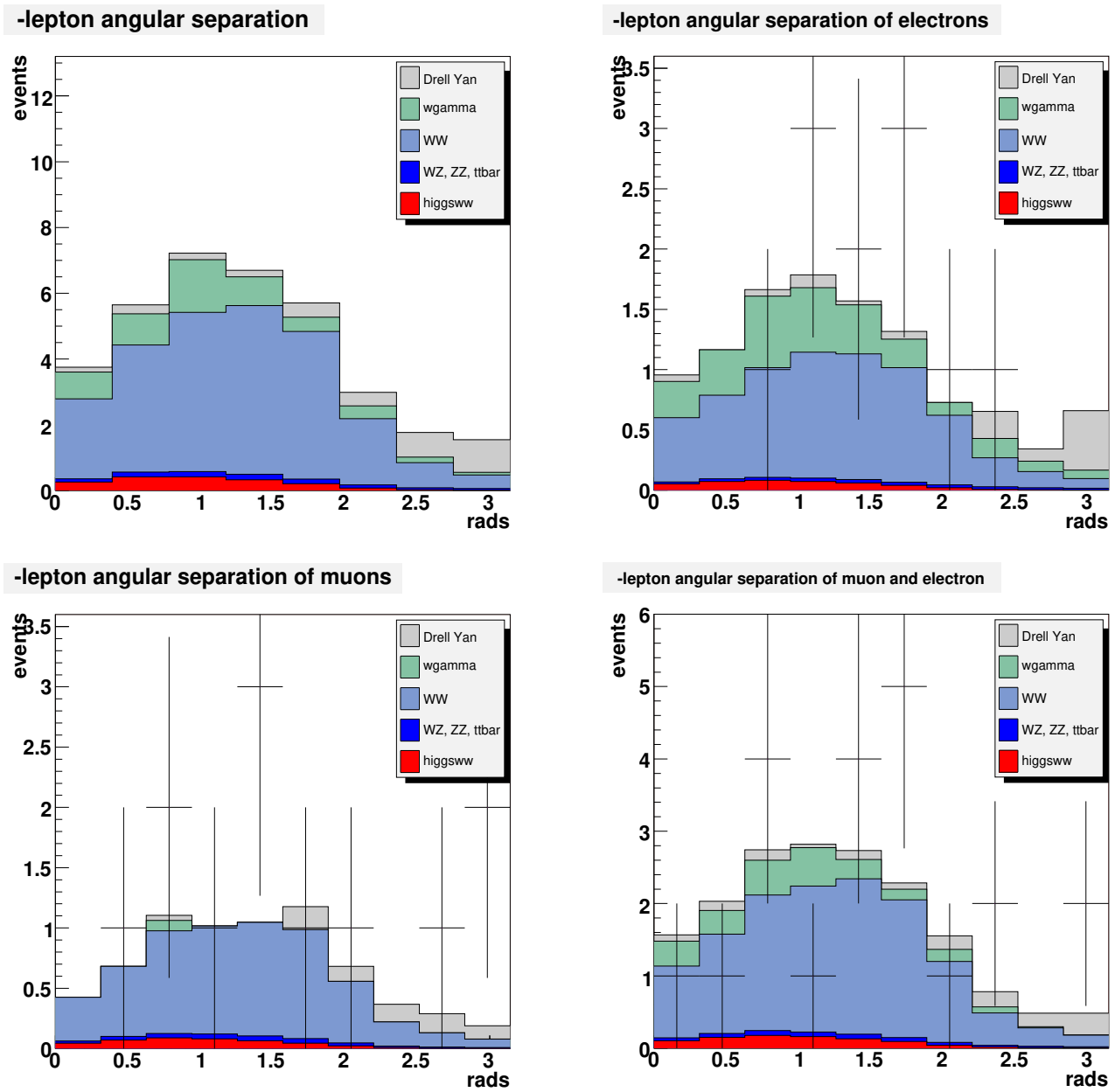

Figure 29: Azimuthal angular separation between the leptons, $\Delta\phi(\ell,\ell)$, from the decay of $H \to WW^* \to \ell\nu\ell\nu$. Distributions of data, HWW^* signal ($M_H = 150$ GeV) MC, WW MC and the sum of other considered background MC samples are shown. The MCs are normalized to the expectations for the integrated luminosity for analyzed data of 1fb^{-1}. We use the upper-left $ee + e\mu + \mu\mu$ plot to fit for a limit on the cross-section of SM HWW production at Tevatron, at the Higgs mass of $M_H = 150$ GeV.

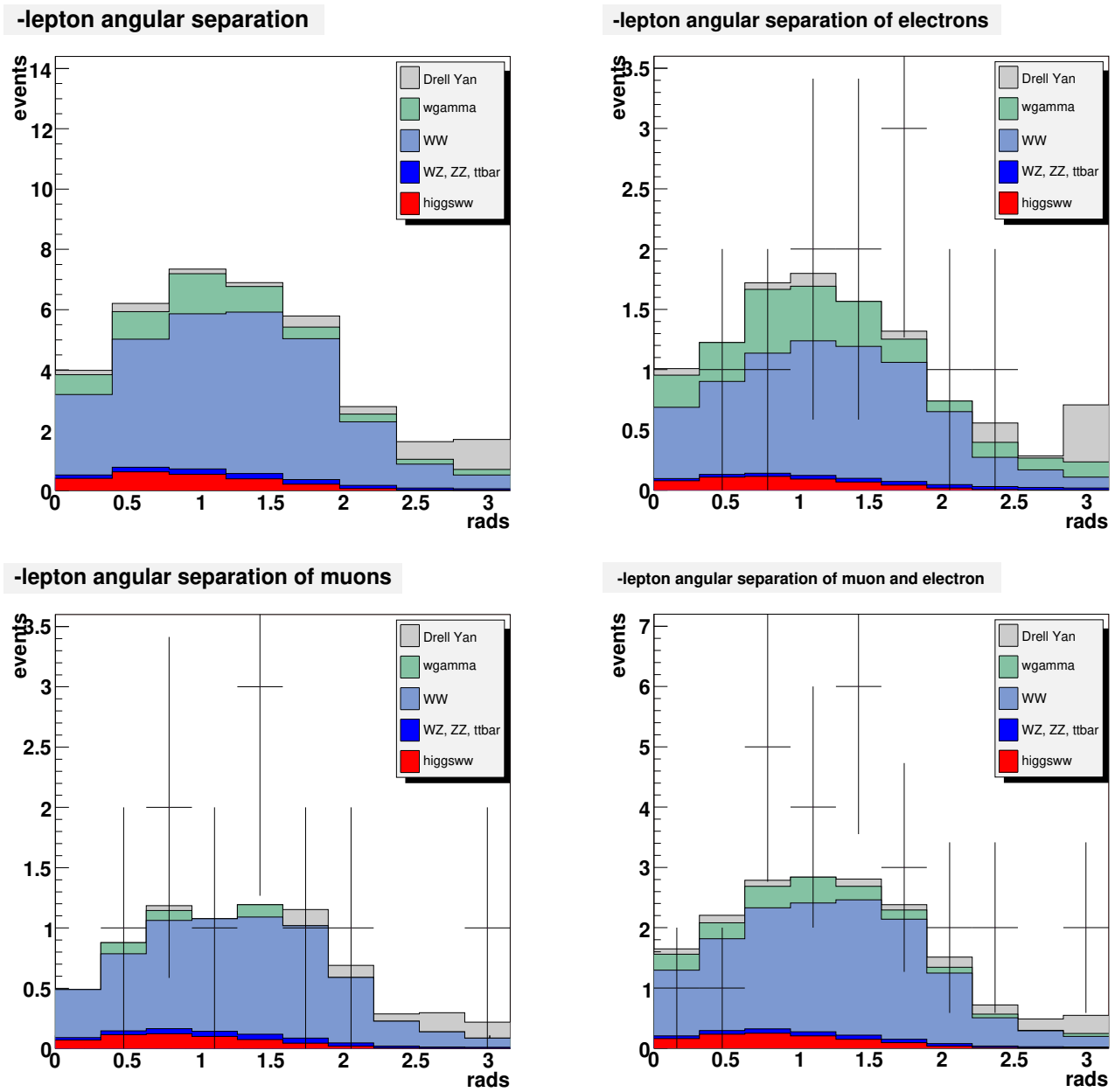

Figure 30: Azimuthal angular separation between the leptons, $\Delta\phi(\ell,\ell)$, from the decay of $H \to WW^* \to \ell\nu\ell\nu$. Distributions of data, HWW^* signal ($M_H = 160$ GeV) MC, WW MC and the sum of other considered background MC samples are shown. The MCs are normalized to the expectations for the integrated luminosity for analyzed data of 1fb^{-1}. We use the upper-left $ee + e\mu + \mu\mu$ plot to fit for a limit on the cross-section of SM HWW production at Tevatron, at the Higgs mass of $M_H = 160$ GeV.

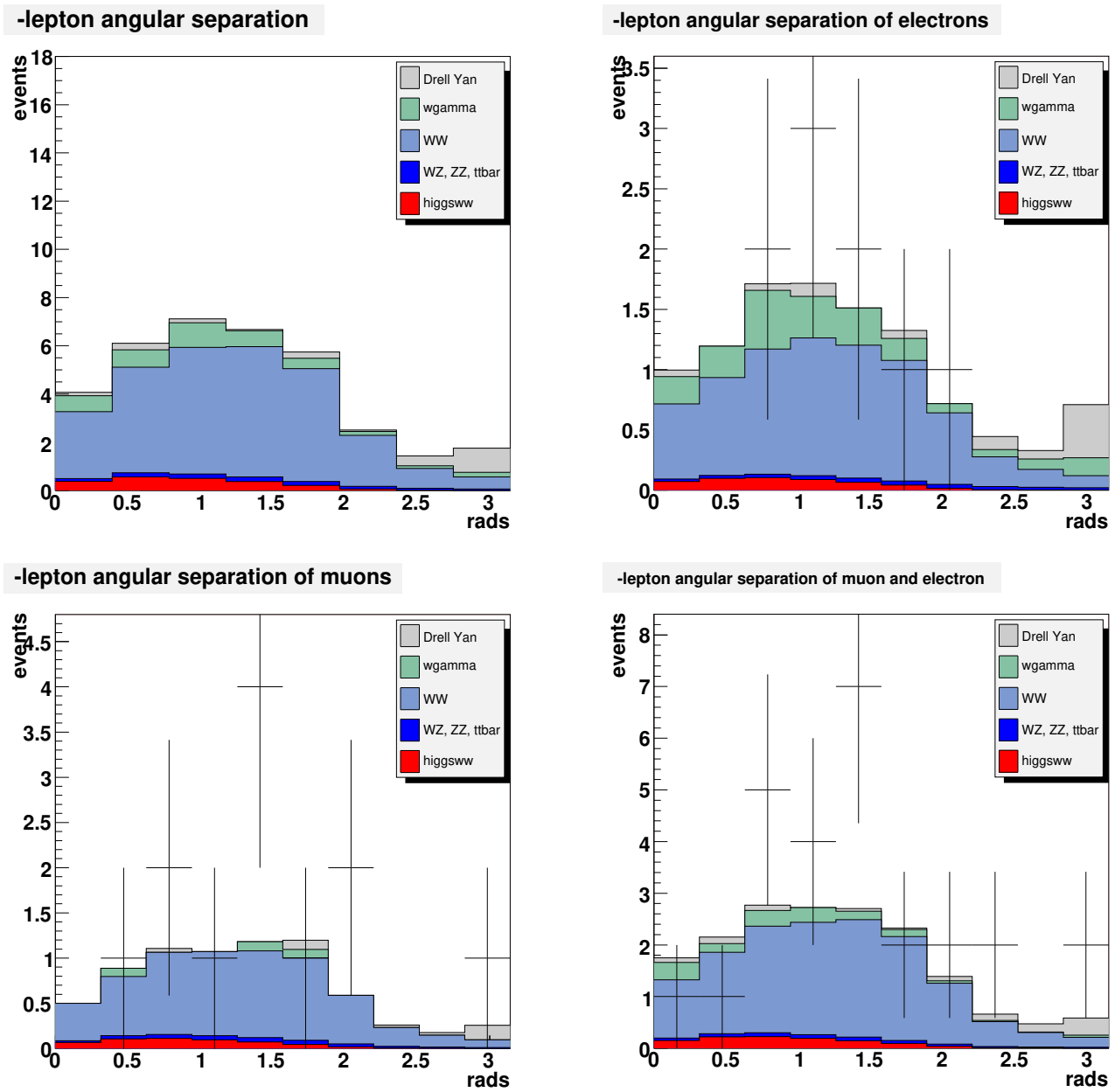

Figure 31: Azimuthal angular separation between the leptons, $\Delta\phi(\ell,\ell)$, from the decay of $H \to WW^* \to \ell\nu\ell\nu$. Distributions of data, HWW^* signal ($M_H = 170$ GeV) MC, WW MC and the sum of other considered background MC samples are shown. The MCs are normalized to the expectations for the integrated luminosity for analyzed data of 1fb^{-1}. We use the upper-left $ee + e\mu + \mu\mu$ plot to fit for a limit on the cross-section of SM HWW production at Tevatron, at the Higgs mass of $M_H = 170$ GeV.

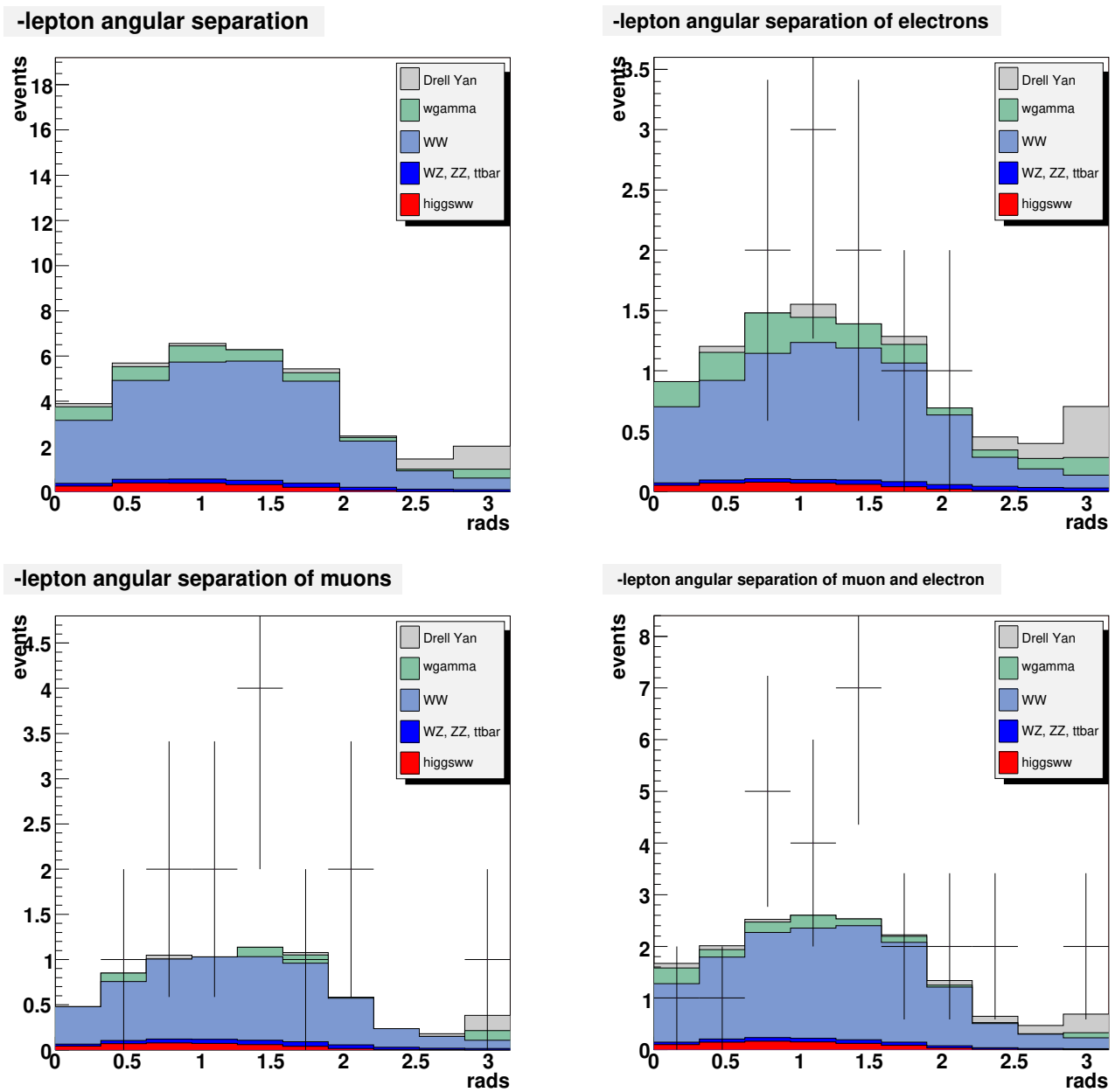

Figure 32: Azimuthal angular separation between the leptons, $\Delta\phi(\ell,\ell)$, from the decay of $H \to WW^* \to \ell\nu\ell\nu$. Distributions of data, HWW^* signal ($M_H = 180$ GeV) MC, WW MC and the sum of other considered background MC samples are shown. The MCs are normalized to the expectations for the integrated luminosity for analyzed data of 1fb^{-1}. We use the upper-left $ee + e\mu + \mu\mu$ plot to fit for a limit on the cross-section of SM HWW production at Tevatron, at the Higgs mass of $M_H = 180$ GeV.

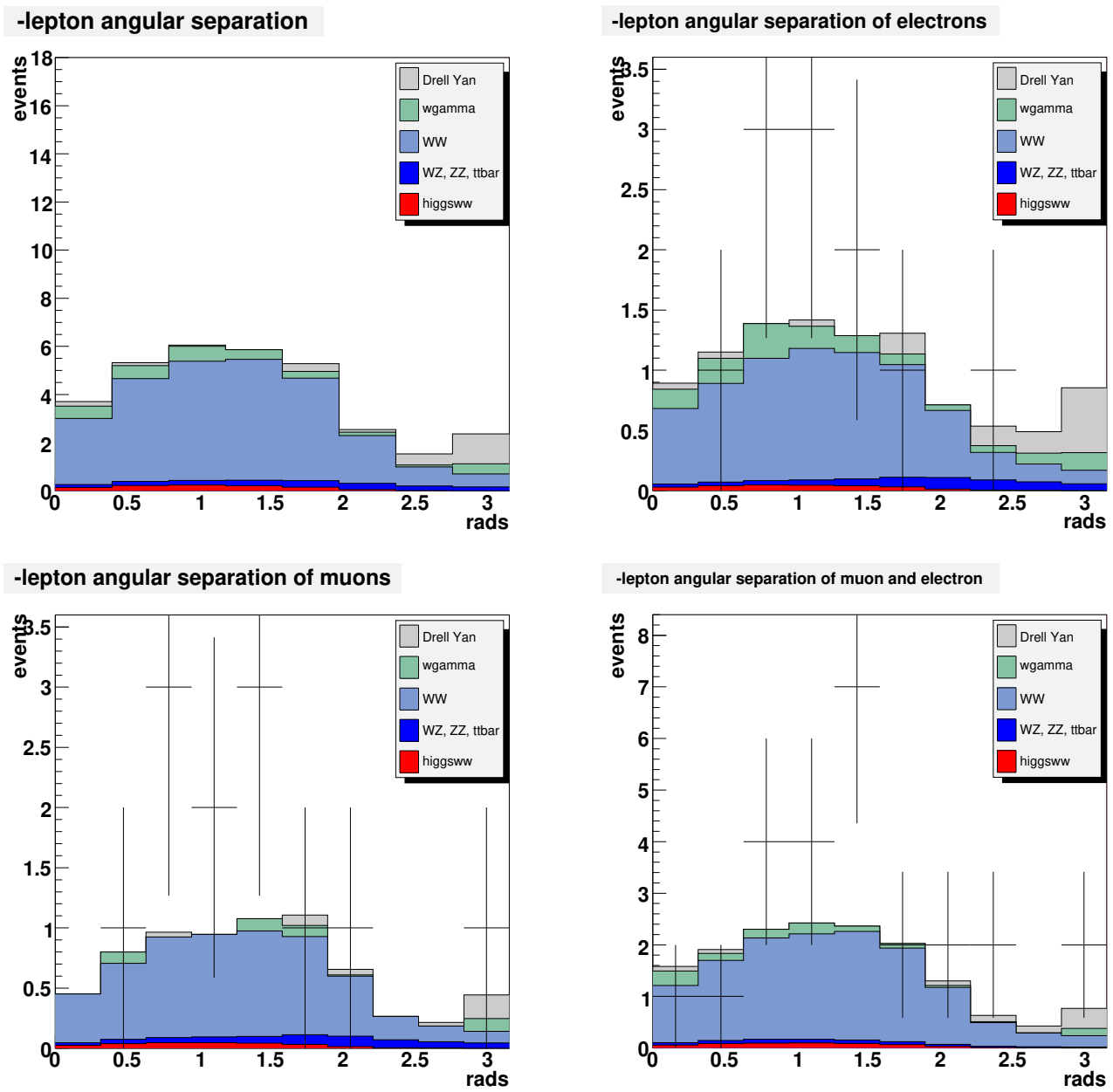

Figure 33: Azimuthal angular separation between the leptons, $\Delta\phi(\ell,\ell)$, from the decay of $H \to WW^* \to \ell\nu\ell\nu$. Distributions of data, HWW^* signal ($M_H = 190$ GeV) MC, WW MC and the sum of other considered background MC samples are shown. The MCs are normalized to the expectations for the integrated luminosity for analyzed data of 1fb^{-1}. We use the upper-left $ee + e\mu + \mu\mu$ plot to fit for a limit on the cross-section of SM HWW production at Tevatron, at the Higgs mass of $M_H = 190$ GeV.

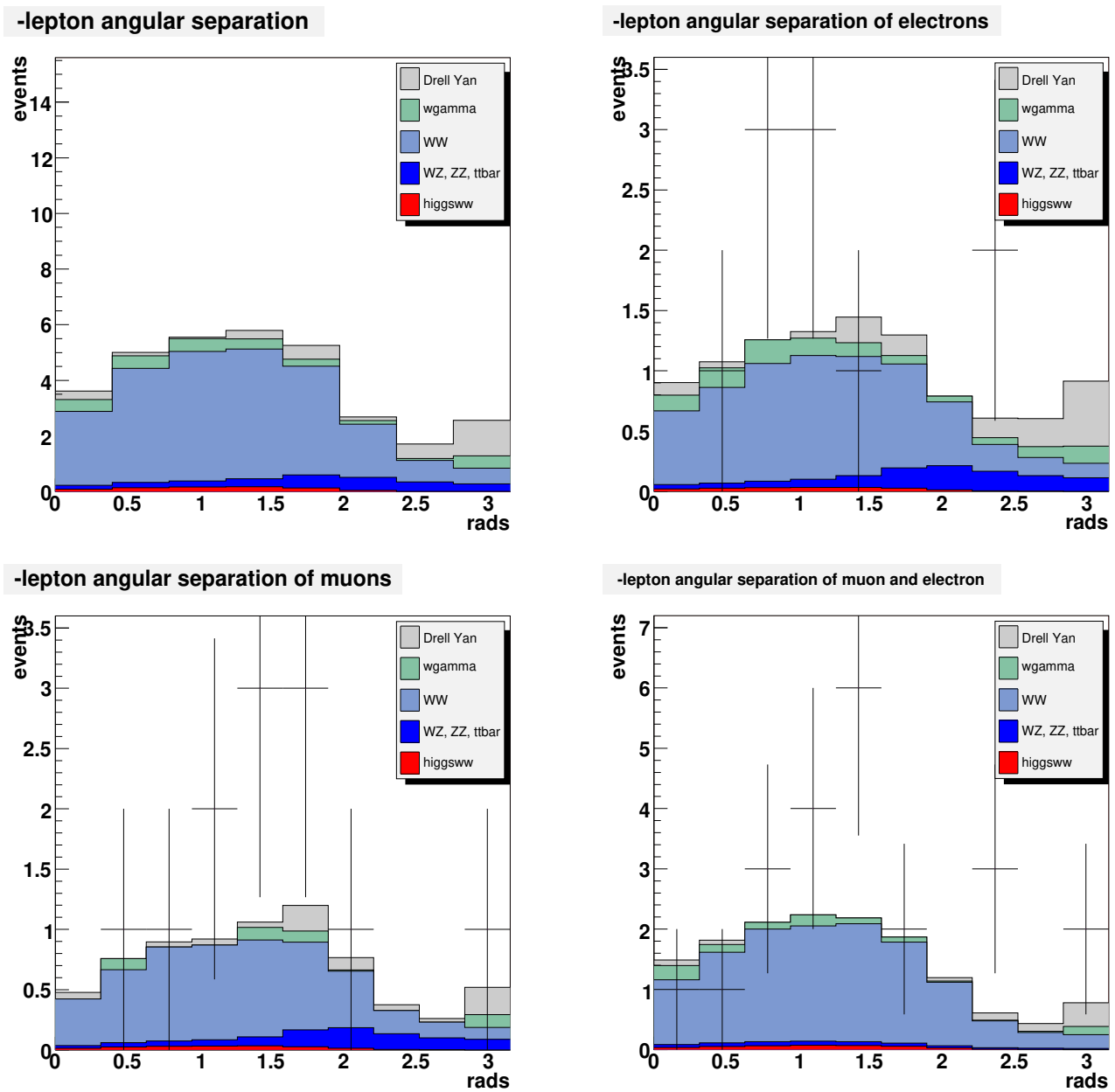

Figure 34: Azimuthal angular separation between the leptons, $\Delta\phi(\ell,\ell)$, from the decay of $H \to WW^* \to \ell\nu\ell\nu$. Distributions of data, HWW^* signal ($M_H = 200$ GeV) MC, WW MC and the sum of other considered background MC samples are shown. The MCs are normalized to the expectations for the integrated luminosity for analyzed data of 1fb^{-1}. We use the upper-left $ee + e\mu + \mu\mu$ plot to fit for a limit on the cross-section of SM HWW production at Tevatron, at the Higgs mass of $M_H = 200$ GeV.

11 Multi-variate Signal Descrimination

The results of the previous section are straight forward to interpret, but determining a cross section or a limit on a cross section by placing cuts on a single discriminant variable limits the analysis strength. Signal is lost in the cuts, cutting on the sample increases statistical errors, and any extra information that may be used to separate the signal and background is not used. Analyses based on a multi-variate discrimination were therefore investigated. The Program TMVA, (T-Multi-Variate-Analysis) which is now packaged in versions of ROOT from 5.00.00 onwards, was used to find the relative discrimination power of a range of methods. A comparison of the strength of discrimination methods available by TMVA wre initially performed on the 0d dataset (run number < 186599). As investigations were starting using TMVA, the current release was not completely functional. The code was modified for certain methods in order to make it work, so the TMVA used does not match any version, but was based on version 2.1 (Tagged 00.00.10). As an investgatory measure, any variable that had been used in the cut-based analysis was used as an input variable, as in Table 25.

variable	meaning
LepAEn	first lepton energy
LepBEn	second lepton energy
ntightjets	number of tight jets
jet1_Et	first highest energy jet energy
jet2_Et	second highest energy jet energy
metmag	$\not\!\!E_T$
addEt	sum of $\not\!\!E_T$ and the lepton E_Ts
dilmass	dilepton mass
dPhiMetLJ	phi angle between $\not\!\!E_T$ and the nearest lepton or jet
dildphi	phi angle between leptons
lepR	$\sqrt{\Delta\eta^2 + \Delta\phi^2}$
metsig	metmag/addEt

Table 25: Input variables used in the multivariate analysis

The dilepton events were selected as in the cut based analysis, using version v2_05 of the Hww selection code. The input events were required to pass all the analysis cuts up to, but not including, the missing transverse energy cut. The leptons were also required to be oppositely charged. Thus, the events has the cuts in Table 26 placed on them. Plots of the data and Monte Carlo for these variables are shown in Figures 35, 36 and 37.

Due to the difficulty of differentiating the Higgs signal from WW in the best discriminating variable, $\Delta\phi_{ll}$, comparison of the methods was performed with signal as the $M_h = 160$ GeV Higgs $\rightarrow W^+W^-$ sample as signal, with the WW Monte Carlo as background. In all TMVA analyses, the number of training events and test events were set to half of the smallest test sample. In comparing the available methods on the 0d sample, approxmately 6000 test events were used in training. Methods tested comprised of those in Table 27. In reality, there is a large amount of Drell-Yan background that needs to be removed, and it was suggested that a missing transverse energy cut should be placed on the training samples, to simulate the sample

Index	Sample Selection Cut
0	two leptons with $p_T^{l_{trigger,non-trigger}} > 20.\ 10$ GeV
1	Isolation
2	$M_{ll} > 16$ GeV
3	nJets($E_T > 15$ GeV) =0 —— nJets($E_T < 55$ GeV) =1 —— nJets($E_T < 40$ GeV) = 1
4	opposite lepton charge signs

Table 26: Cuts placed on the input variables before the multivariate analysis.

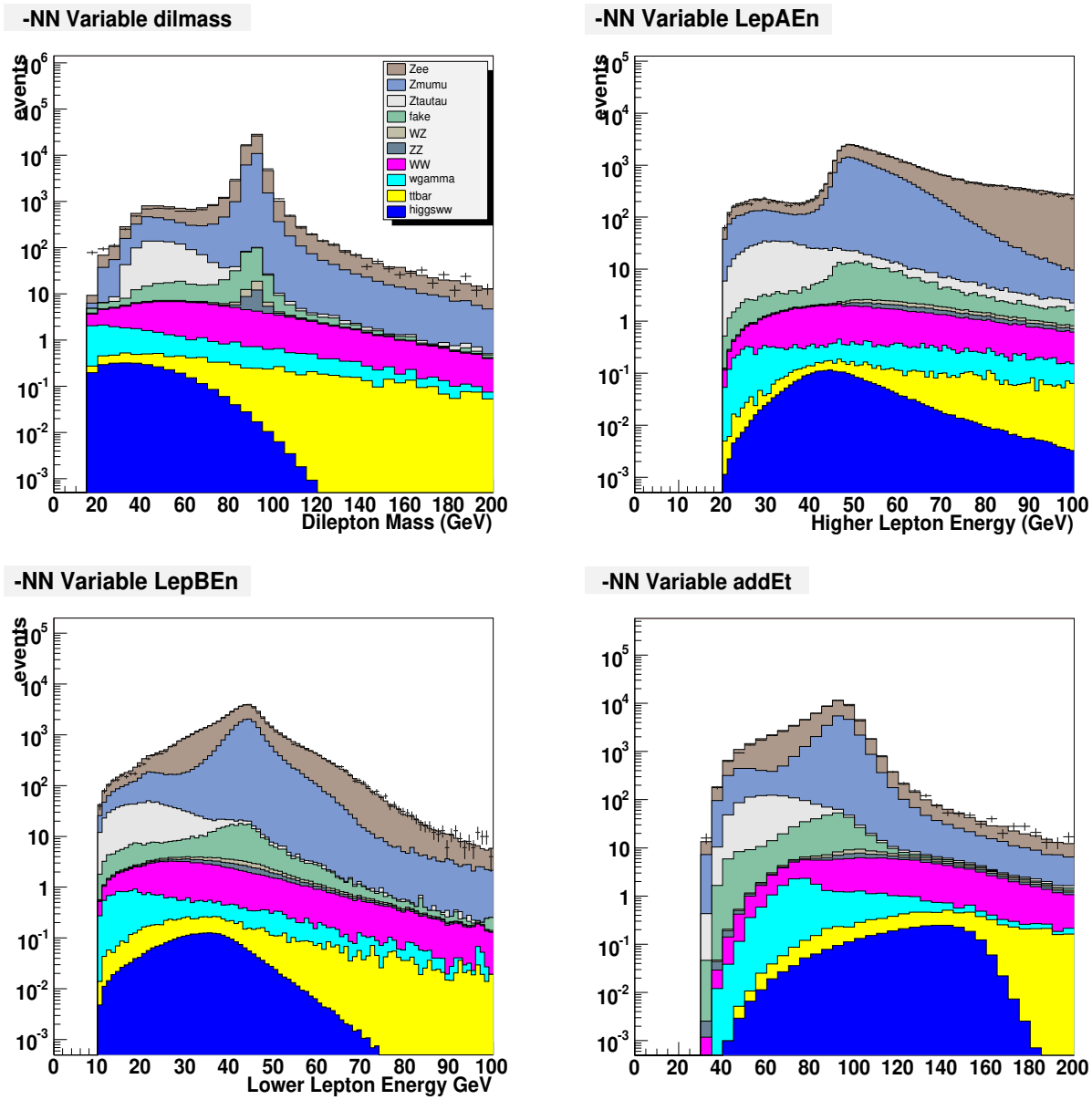

Figure 35: Plots of the input variables for 0d+0h+0i data, with 0d+0h Monte Carlo

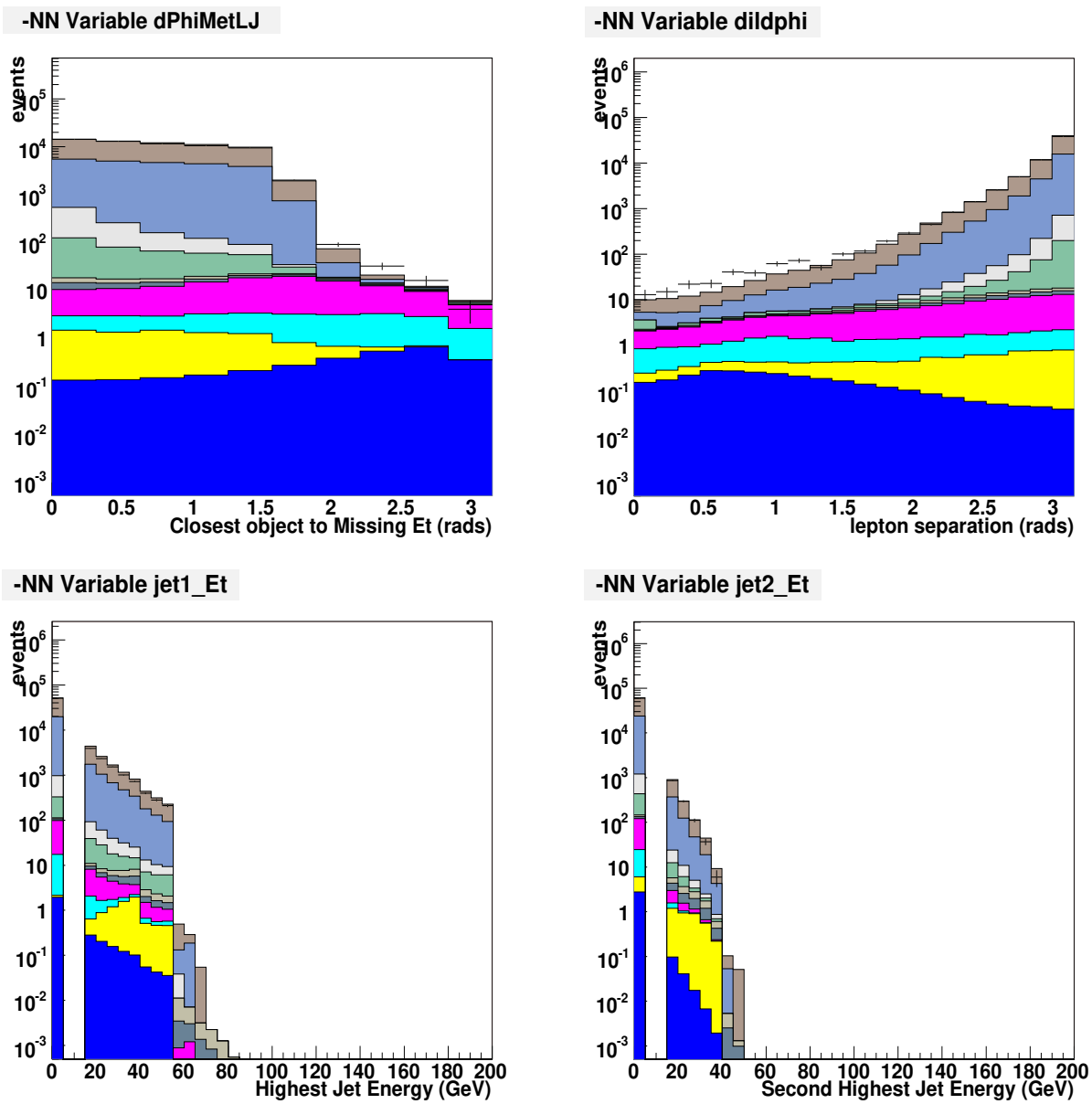

Figure 36: Plots of the input variables for 0d+0h+0i data, with 0d+0h Monte Carlo

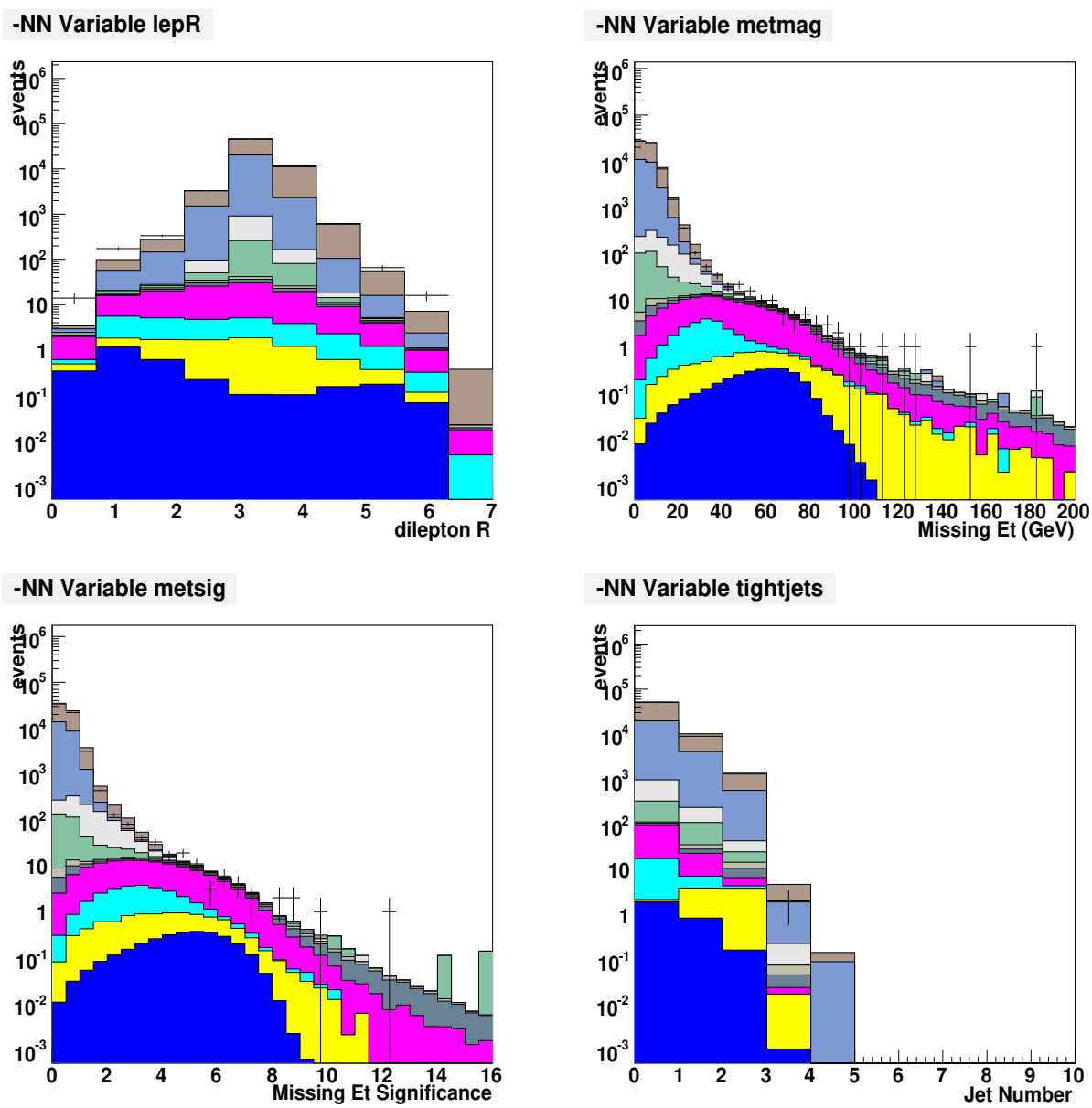

Figure 37: Plots of the input variables for 0d+0h+0i data, with 0d+0h Monte Carlo

TMVA Method Name	description
Likelihood	simple likelihood test on each variable
LikelihoodD	likelihood test with the input variables decorrelated
Fisher	Fisher descriminant analysis
CFMlpANN	Clemont Ferrand Neural Net
H Matrix	Hessian Matrix element Method
PDERS	Multi-dimentional Likelihood fit
BDTGini	Boosted Decision Tree Method

Table 27: Multivariate analyses available and inverstigated with TMVA

for which the differentiation would be most important; there were too few events to train on once this cut had been placed, so the whole of the sample was used. The plot in Figure 38 is a background rejection vs signal efficiency plot, and shows that the Neural Net was the best method for separating the signal and background. TMVA. This was performed with with TMVA v3.3.3, and events selected using v2_53 of the Hww selection code in the 0d run range, as before.

The three Neural nets available to TMVA were compared: TMV is a neural net prgrammed by the authors of TMVA; CFMlpANN is once again the Clemont-Ferrand neural net, and TMLpANN is the TMLP Neural net supplied with ROOT, here using the BFGS Training method. The MLP and the TMLpANN methods were both trined with 200 epochs, and and two hidden layers of N+1 and N nodes where N is the number of input variables. The Clemont Ferrand Neural net requires more epochs for the training to be effective, so this was trained over 5000 epochs; this net also had two hidden layes of nodes, both of dimension N where N is the number of input variables. Once the neural net had been established as the best decriminating method, the analysis was performed for the 0d+0h runranges. With a large amount of training events, it was impractical to continue with the Clemont Ferrand neural net as the number of epochs required is much higher (around 25 times more) than other neural nets. The analysis preceeded with the TMLP neural net, which is available with ROOT. The various training methods were compared using TMVA v3.3.3, and events selected using v2_61 of the Hww code. All events available were used in the training, for which samples in the 0d and 0h runranges were available (run number < 203799). This resulted in approx. 200,000 training and test events. In performing the comparison, the stochastic learning method was abandoned due to long running times when using a large training set. A key which explains the TMVA names for the training methods tested can be found in Table 28. The results in Figure 39 which plots background rejection vs signal efficiency show B FGS to be the best method for signal separation. All training methods were performed with 200 epochs, and two hidden layers of N+1 and N nodes where N is the number of input variables. A comparison of the input variables with a decorrelated input variable set (using a diagonalised covariance matrix) was performed, but as Figure 40 shows, there is little performance gain to be obtained with this operation. Two neural nets were then trained using TMVA v3.3.3. The sample set in each was selected with Hww code v2_61, with the same variables as stated in Table 25, with cuts as stated in Table 26, from the 0d and 0h runranges (run number < 203799). In each, the TMLP neural net was used, with trining method

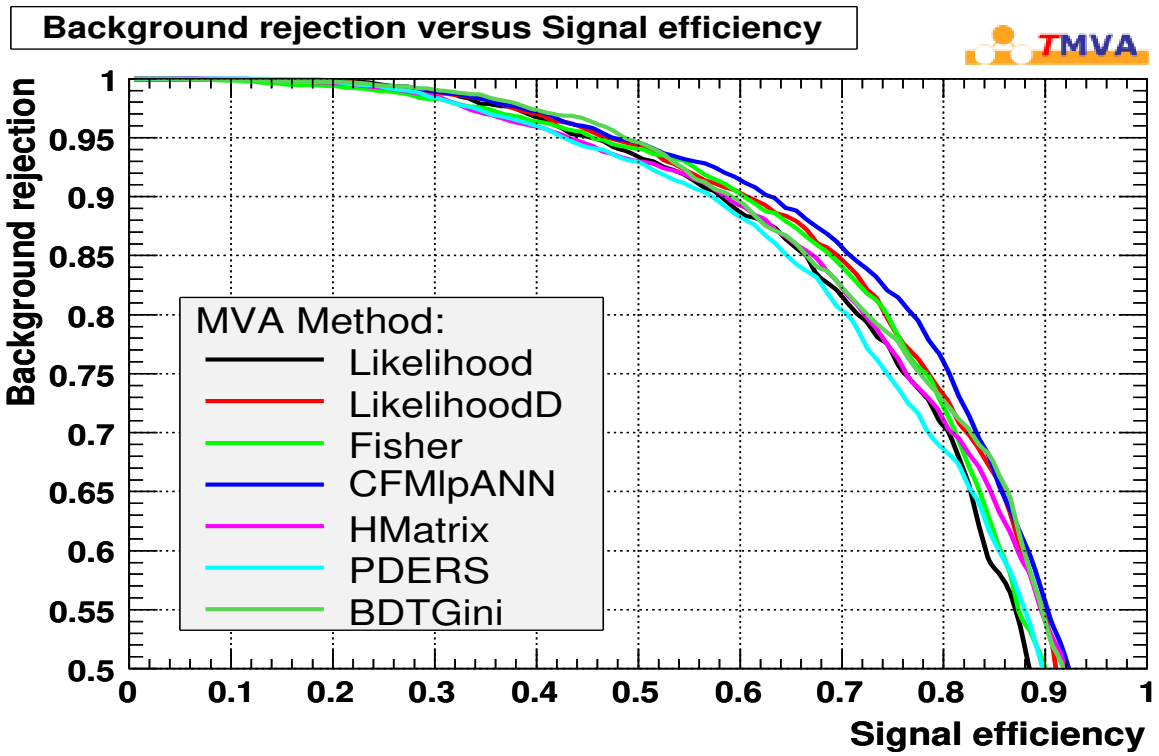

Figure 38: Background rejection vs signal efficiency plots for the methods available in TMVA v2.1 after training on Higgs $\rightarrow$ WW (signal) and WW (background) Monte Carlo smaples form the 0d run range at at M_h of 160 GeV

TMVA Method Name	description
TMLpANNBat	Batch Learning
TMLpANNSD	Steepest Descent
TMLpANNRP	Ribiere Polak Learning algorithm
TMLpANNFR	Fletcher Reeves Learning algorithm
TMLpANNBFGS	Broyden, Fletcher, Goldfarb, Shanno (BFGS)

Table 28: Cuts placed on the input variables before the multivariate analysis

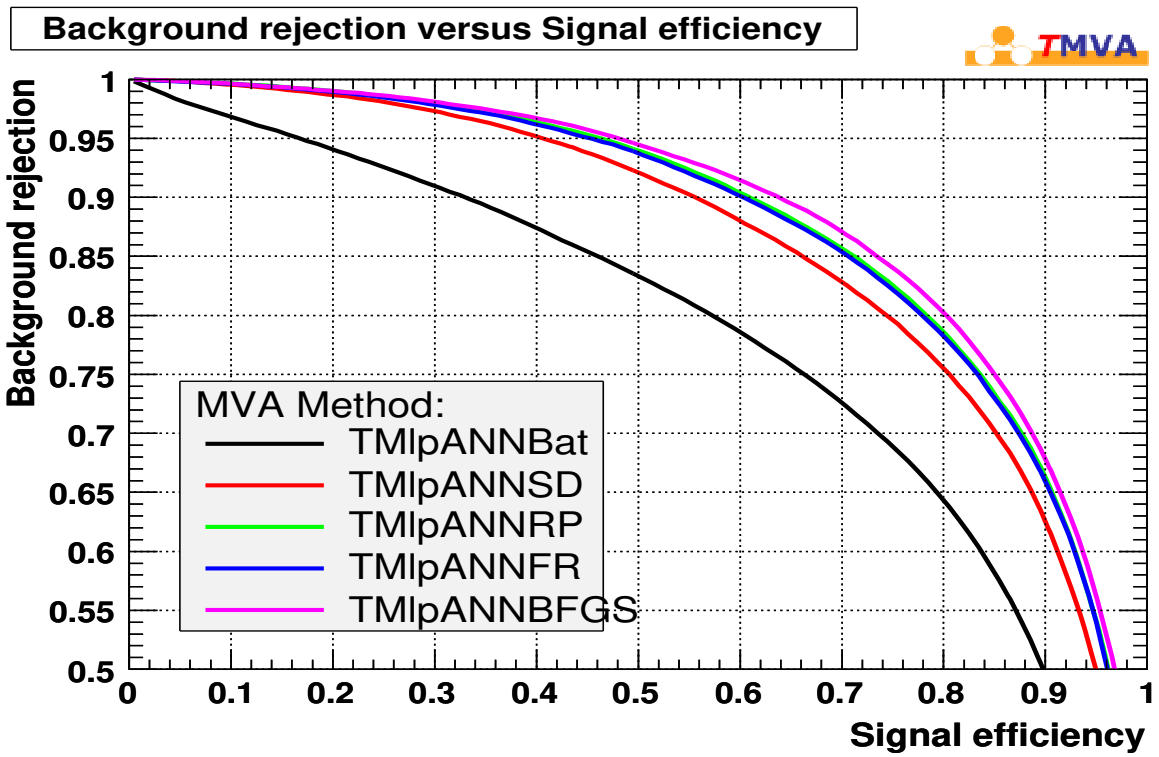

Figure 39: Background rejection vs signal efficiency plots for the training methods available with TMLP using TMVA v3.3.3 after training on Higgs $\rightarrow$ WW (signal) and WW (background) Monte Carlo samples form the 0d+0h run range at at M_h of 160 GeV. A guide to the trining methods can be found in Table 28

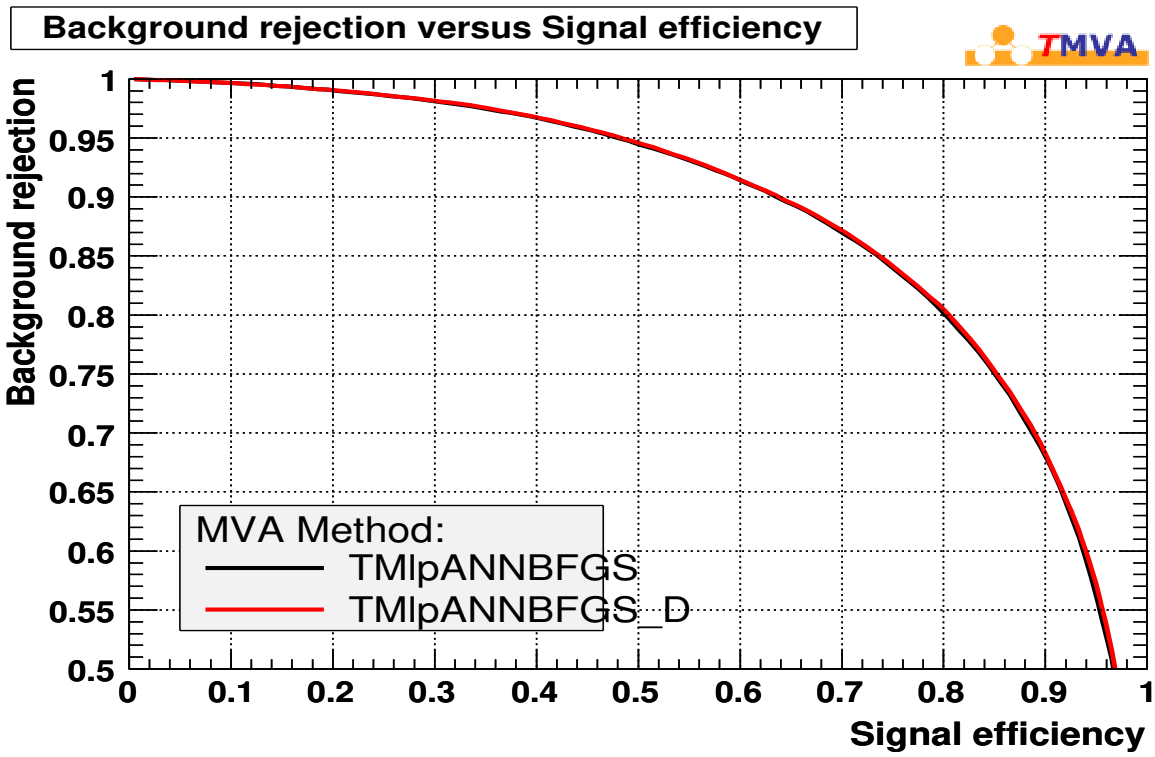

Figure 40: Background rejection vs signal efficiency plots for the TMLP using the BFGS training method, showing the improvement afforded by decorrelating the input variables. This uses TMVA v3.3.3 and is trained on Higgs $\rightarrow$ WW (signal) and WW (background) Monte Carlo samples form the 0d+0h run range at at M_h of 160 GeV. The suffix '_D' signifies the training done with decorrelated input variables

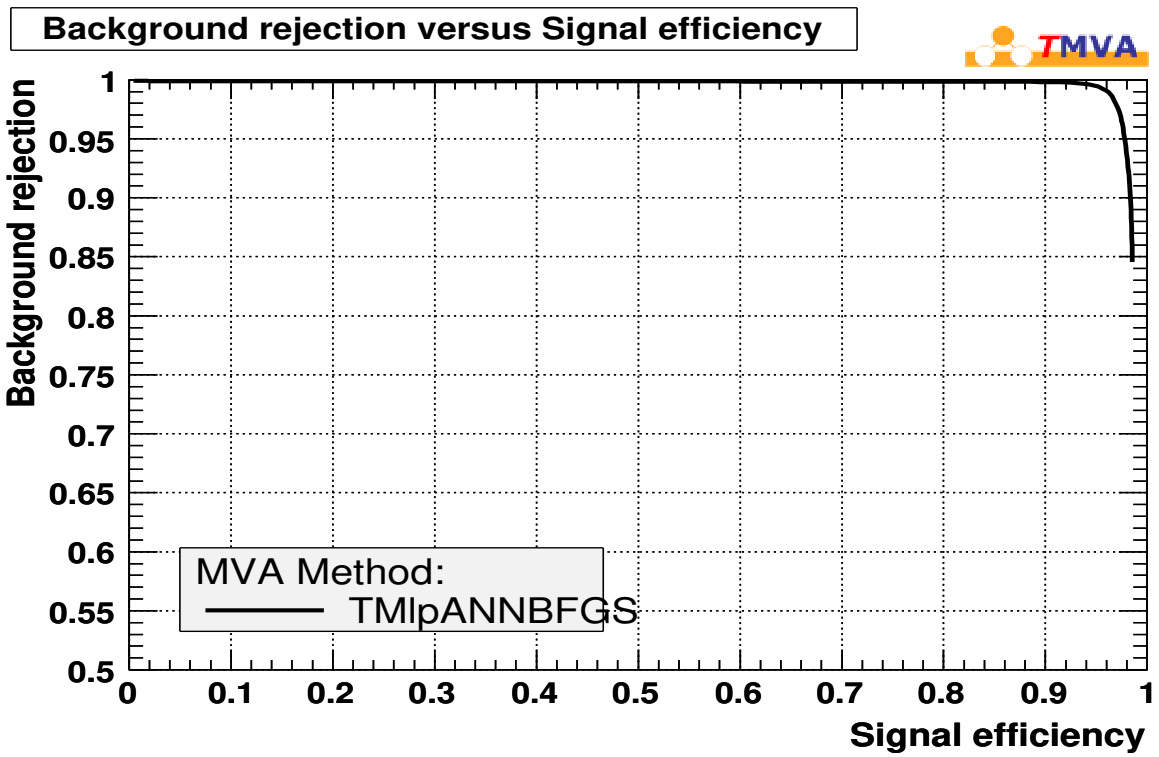

Figure 41: Background rejection vs signal efficiency plots for the TMLP using the BFGS training method. This uses TMVA v3.3.3 and is trained on Higgs → WW (signal) and Z→ee, Z→ $\mu\mu$, and Z→ $\tau\tau$,(background) Monte Carlo samples form the 0d+0h run range at at M_h of 160 GeV.

BFGS, 200 epochs and two hidden layers of N+1 and N nodes, where N is the number of input variables. The signal sample in each was H → WW Monte Carlo with a M_h of 160 GeV. The background for the first neural net was randomly taken from the three Drell-Yan Monte Carlo samples, to electrons, muons and taus, scaled to their relative crossections. The second neural net was trained on WW Monte Carlo. In each, the number of events for training was the same as that for testing, and the same number of events was used for signal and background. In each, the number was limited by the sample with the least number of events, which was the Higgs → WW sample, so each were both trained and tested with 100,000 events. Figures 39 and 41 show the background rejection vs signal efficiency for the two nets, and Figures 42 and 43 show the normalised separation of the test events by the neural nets. These two neural net were then applied to all the background and signal Monte Carlo events, and the data, to give each event two weights. Figure 44 shows the data and the Monte Carlo superimposed using the Higgs → WW sample of M_h=160 GeV for the two neural nets. In the first figure, all events are shown. In the second figure, only those events with score greater than 0.985 are shown. The fitting procedure described in Section 10 was applied to the WW/Higgs neural net output in Figure 44 in order to detemrine the contribution of the Higgs signal. The results are shown in Tables 29 and 30 and graphically in Figure 46.

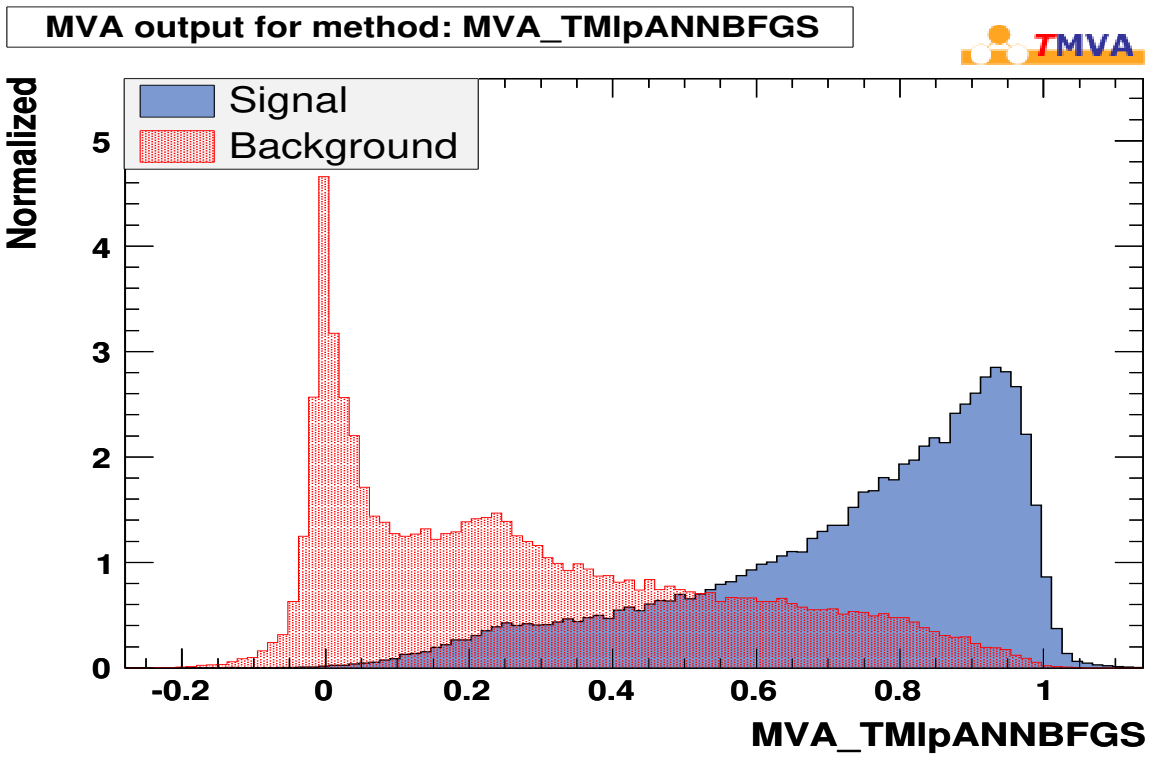

Figure 42: Background and Signal separation plots for the training methods available with TMLP using TMVA v3.3.3 after training on Higgs $\rightarrow$ WW (signal) and WW (background) Monte Carlo samples form the 0d+0h run range at at M_h of 160 GeV.

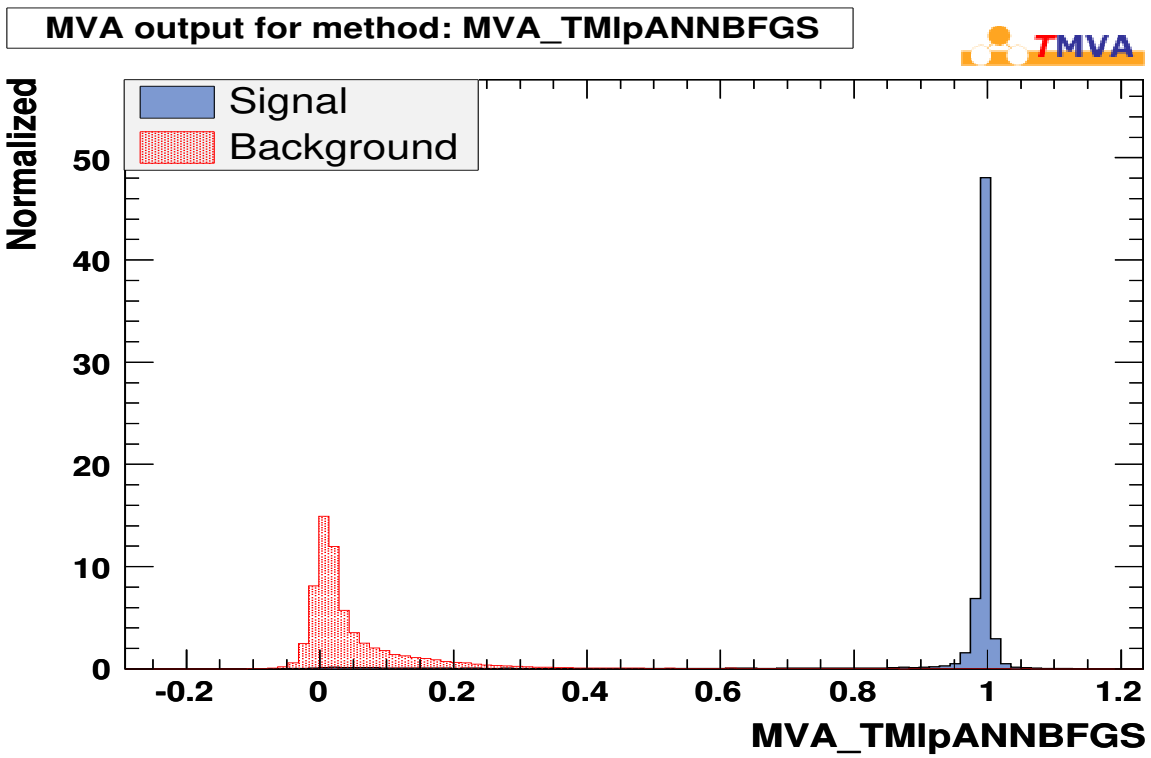

Figure 43: Background and Signal separation plots for the TMLP using the BFGS training method. This uses TMVA v3.3.3 and is trained on Higgs $\rightarrow$ WW (signal) and Z$\rightarrow$ee, Z$\rightarrow \mu\mu$, and Z$\rightarrow \tau\tau$,(background) Monte Carlo samples form the 0d+0h run range at at M_h of 160 GeV.

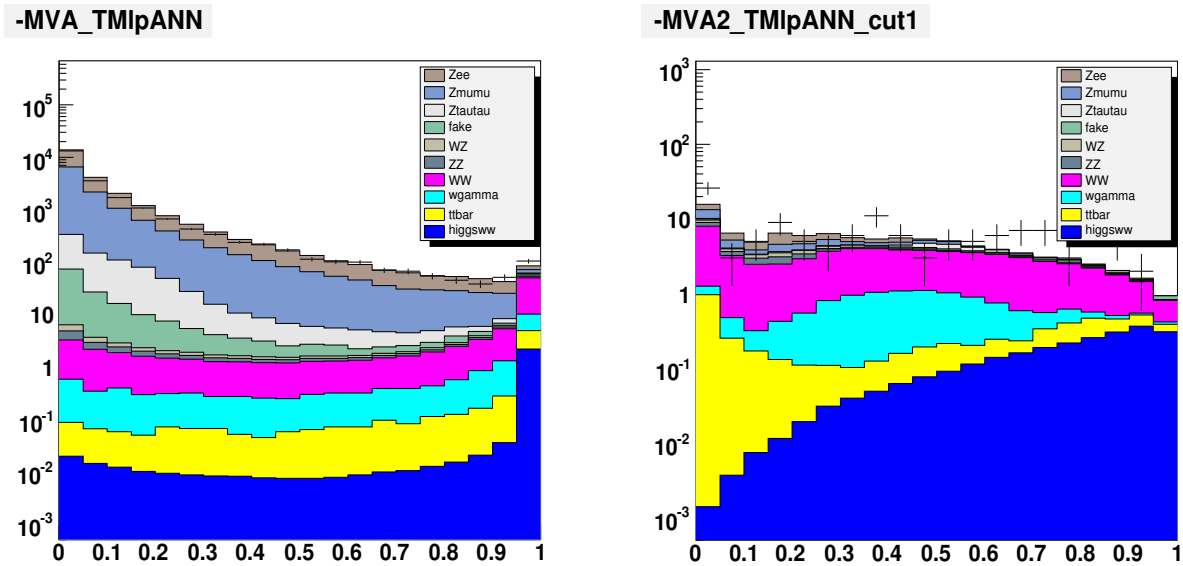

Figure 44: Plots of the neural net scores for data and Monte Carlo. Drell-Yan background descrimination is on the left and the WW background descrimination, on theright, has a cut on the first plot at a score of 0.985 to illustrate the separation in the absence of the Drell-Yan background

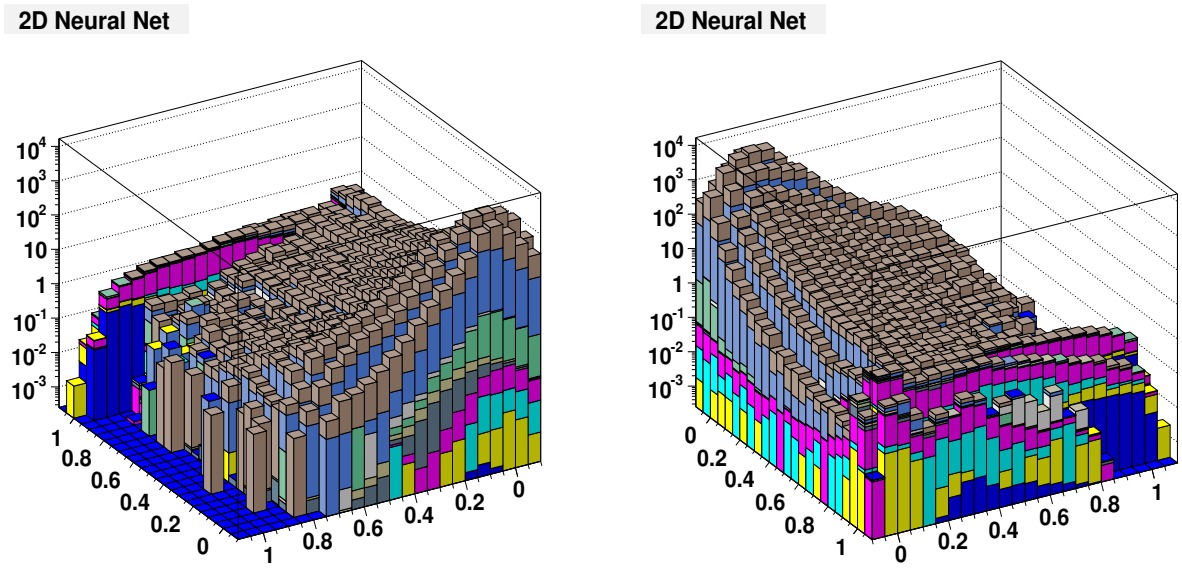

Figure 45: Plots of the neural net scores for data and Monte Carlo. This is the same plot from two differnt angles. Drell-Yan background descrimination is on the left and the WW background descrimination, on theright, has a cut on the first plot at a score of 0.985 to illustrate the separation in the absence of the Drell-Yan background

A two dimensional plot of these were then created, and Figure 45 shows the distribution of the Monte Carlo samples.

M_H	110	120	130	140	150
Tom expected tomstyle on MVA2_TMlpANN_cut1		7.608	4.448	3.464	2.676
Tom actual tomstyle on MVA2_TMlpANN_cut1		12.895	8.398	6.314	4.623
Tom expected tomstyle Bayes on MVA2_TMlpANN_cut1		7.670	4.585	3.435	2.695
Tom actual tomstyle Bayes on MVA2_TMlpANN_cut1		12.772	8.549	6.420	4.837
Tom expected emu Bayes					
Tom actual emu Bayes					

Table 29: Results of the cuts analysis for various fitting procedures and handling of systematic uncertainties

M_H	160	170	180	190	200
Tom expected tomstyle on MVA2_TMlpANN_cut1	1.718	1.913	2.758	3.568	4.322
Tom actual tomstyle on MVA2_TMlpANN_cut1	2.640	2.987	4.377	6.093	7.950
Tom expected tomstyle Bayes on MVA2_TMlpANN_cut1	1.821	1.982	2.779	3.604	4.339
Tom actual tomstyle Bayes on MVA2_TMlpANN_cut1	3.020	3.302	4.627	6.352	8.050
Tom expected emu Bayes					
Tom actual emu Bayes					

Table 30: Results of the Neural Net analysis for various fitting procedures and handling of systematic uncertainties

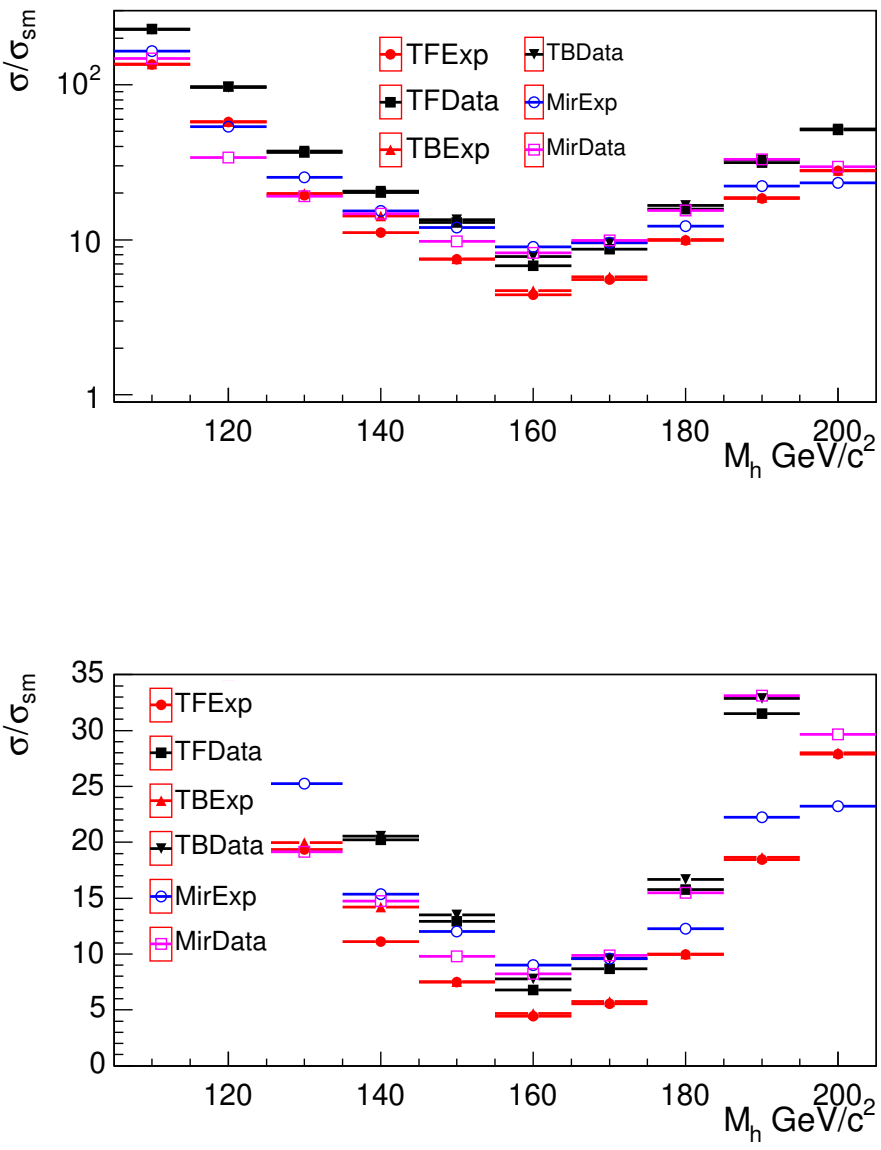

Figure 46: Expected (red) and Actual (black) limits for $\sigma(gg \to H^0) \times \mathrm{BR}(H^0 \to W^+W^-)$ relative to that expected in the NNLO computation of Table 1. The blue points are taken from CDF7708 for the expected limits and the magenta points for the actual limits in CDF7708.

M_H (GeV/c^2)	110	120	130	140	150	160	170	180	190	200
Expected (pb)		7.6	4.4	3.5	2.7	1.7	1.9	2.8	3.6	4.3
Actual (pb)		12.9	8.4	6.3	4.6	2.6	3.0	4.4	6.1	8.0

Table 31: Expected and Actual limits on the cross section for $p\bar{p} \to H^0 \to WW^*$.

12 Conclusions

We have studied high p_t dilepton events and measured the cross section for $\sigma(p\bar{p} \to Z^0) \times \mathrm{BR}(Z^0 \to l^+l^-)$ separated by the different types of dileptons separated by which detector system was used to identify them. We achived a consistency of better than 1% across all categories and a cross section consistent with expectation from the Standard Model. We then proceeded to search for a contribution of $H^0 \to W^+W^-$ decays using a cut procedure. and then using a more sophisticated neural network. A statistically significant contribution of the Higgs signal is not observed, so a 95% C.L. limit on the Standard-Model cross-section $\times$ branching ratio $\sigma \cdot \mathrm{BR}_{\mathrm{SM}}(p\bar{p} \to H \to WW^*)$ at center-of-mass energy $\sqrt{\hat{s}} = 1.96$ TeV, for Higgs masses between 110 - 200 GeV has been set as shown in Table 31.

References

[1] "Search for a Neutral Higgs Boson Decaying to a W Boson Pair in p a nti-p Collisions at s**(1/2) = 1.96 TeV ", Phys. Rev. Lett. 97, 081802 (2006) and "Search for $H \to WW^*$ in the dilepton channel with 360 pb^{-1} of Run II Data ", S. Chuang,M. Coca,M. Kruse, CDF7708.

[2] "QCD corrections to Higgs-boson production at proton-proton colliders", D. Graudenz, M. Spira, P. M. Zerwas, Phys. Rev. Lett. 70, 1372 - 1375 (1993) and "Soft-gluon resummation for Higgs boson production at hadron colliders", S. Catani, D. de Florian, M. Grazzini, P. Nason, hep-ph/0306211.

[3] Lep Electroweak Workging Group page

`http://lepewwg.web.cern.ch/LEPEWWG/`

[4] "Search for the Standard Model Higgs boson at LEP", ALEPH Collaboration, DELPHI Collaboration, L3 Collaboration, OPAL Collaboration and The LEP Working Group for Higgs Boson Searches, Phys. Lett. B 565 (2003) 61.

[5] J. Pumplin *et al.*-"New Generation of Parton Distributions with Uncertainties from Global QCD Analysis",hep-ph/0201195

[6] S. Sultansoy,"The "Golden Mode" at the Upgraded Tevatron?",hep-ex/0010037.

[7] S. Miller, "Pdf Acceptance Uncertainties for $t\bar{t}$ Cross Section", Joint Physics Web page March 19, 2004.

[8] Joint Physics web page:

`http://www-cdf.fnal.gov/internal/physics/joint_physics/instructions/pdferrors.html`

[9] J.Huston, J.Campbell, J. Stirling, "Hard interactions of Quarks and Gluons: a Primer for LHC Physics"

`http://www.pa.msu.edu/~huston/seminars/Main.pdf`

[10] O. Gonzalez and C. Rott, "Uncertainties due to the PDFs for the gluino-sbottom search", CDF-7051.

[11] A.Abulencia *et al.*, CDF Collaboration, "Measurements of Inclusive W and Z Cross Sections in $p\bar{p}$ Collissions at $\sqrt{s} = 1.96$ TeV", CDF Note 7332.

[12] PRL 84 (5) 845 (2000).

[13] David Dagenhart, "Measurement of the Z Production Cross Section", CDF-7865.

[14] Martin Griffiths, Beate Heinemann, Giulia Manca, "Central Electron ID Efficiencies at Medium Energy", CDF-7233.

[15] D.Bortoletto, A.Canepa, O.Gonzalez, E.Lytken, "Search for the associated production of chargino and neutralino in dimuon+lepton events", CDF-7714.

[16] C.Hill, J.Incandela, and C.Mills, "Electron Identification in Offline Release 5.3", CDF-7309.

[17] Tim Nelson, Rick Snider, David Stuart, "Forward Electron Tracking with the PhoenixMods Package", CDF-6278.

[18] Sunny S.Chuang, D.Carlsmith, Susana Cabrera, Mark Kruse, Dustin McGivern, David Waters, "Search for a SM Higgs Boson in the gg→H→WW* Dilepton Channel with 200/pb Run II Data at CDF", CDF-6958.

[19] Yoshio Ishizawa and Jason Nielsen, "Trigger Efficiencies for High Et Electrons", CDF-7401.

[20] D. Benjamin,P. Bussey,T. Davies,D. Hidas,M. Kruse,A. Robson,R. St. Denis,A. S. Thompson, "Fake Lepton Studies for HWW analysis with 1/fb", CDF-8649

[21] D. Benjamin,P. Bussey,T. Davies,D. Hidas,M. Kruse,A. Robson,R. St. Denis,A. S. Thompson, "Application of Fake Lepton Studies to the HWW analysis with 1/fb", CDF-8652

[22] U. Grundler, A. Taffard, X. Zhang, "High-Pt muons recommended cuts and efficiencies for summer2006", CDF-8262.

[23] T. Spreitzer, C. Mills, J. Incandela, "Electron ID Efficiency and Scale Factor with TopNtuple 6.1.4 for Summer 2006", CDF-8274.

[24] S.Cabrera, S.Carron, S.Chuang, J.Deng, A.Goshaw, Y.Huang, M.Kruse, D.McGivern, D.Waters, "WW Production in the Dilepton channel with 200/pb", CDF-6909

[25] S.Cabrera, J.Deng, A.Goshaw, C.Hays, Y.Huang, M.Kruse- Measurement of ZZ+ZW cross section using Run II data, CDF-6920

[26] Joint Physics Meeting High-Pt Lepton ID http://www-cdf.fnal.gov/internal/physics/joint_physics/index.html.

[27] " Muon Selection for the H$\rightarrow$ W^+W^- Analysis", D. Benjamin, P. Bussey, D. Hidas, M. Kruse, A. Robson, R. St. Denis, A.S. Thompson, CDF Note XXXX

[28] "High P_T Intermediate Muon (BMU) Reconstruction and Identification with 5.3.3/6.1.2 Data vs 5.3.3/6.1.3 MC", S.Carillo,S.Chuang,N.Giokaris,A.Manousakis,A.Taffard,M.Techio,F.Vazquez, Costas Velidis, CDF 8088.

[29] Jet Energy and Resolution Group "Jet Energy Corrections Systematic Uncertainties" http://www-cdf.fnal.gov/internal/physics/top/jets/systematics.html.

[30] R.Barate *et al.*, ALEPH Collaboration", hep-ex/0306033 (Phys.Lett.B 565), 2003

[31] Tomura, Tomonobu, Top Mass at the Tevatron, HCP 2005, 4-9 July 2005

[32] M.Carena *et al.*, Report of the Tevatron Higgs Working Group, hep-ph/0010338

[33] D.Benjamin *et al.*, Measurement of the Wgamma and Zgamma Production Cross Sections using 200/pb of Run 2 Data, CDF-6601

[34] U.Baur, Berger El., Probing the WW gamma vertex at the Fermilab Tevatron Collider, Phys Rev D .41, 1476 (1990).

[35] B.Heinemann, A.Goshaw, M.Kirby, N.Tanimoto, H.Hayward - Measurement of Wgamma and Zgamma Production in $p\bar{p}$ collisions at sqrt(s)=1.96 TeV, CDF 7165

[36] M.Tecchio - Acceptance and background systematics for the Top Dilepton cross-section measurement, CDF 6590

[37] T. Junk, "Sensitivity, Exclusion, and Discovery with Small Signals, Large Backgrounds, and Large Systematic Uncertainties", CDF 8128.

A Expected signal, backgrounds and data candidates per di-lepton channel

110 GeV	ee	$e\mu$	$\mu\mu$	ll
WW	2.71009+-1.64624	5.26205+-2.29392	2.46031+-1.56854	10.4325+-3.229
WZ	0.0943042+-0.30709	0.187537+-0.433055	0.110477+-0.33238	0.392318+-0.626
ZZ	0.087543+-0.295877	0.0373484+-0.193257	0.0904517+-0.300752	0.215343+-0.464
ttbar	0.0529269+-0.230059	0.156991+-0.396221	0.0501418+-0.223924	0.260059+-0.509
wgamma	3.45454+-1.85864	3.16116+-1.77797	0.0136383+-0.116783	6.62934+-2.574
DYll	2.6868+-1.63915	4.07353+-2.0183	2.7433+-1.65629	9.50363+-3.082
Background Total	9.08621+-3.01433	12.8786+-3.58868	5.46832+-2.33844	27.4332+-5.237
higgsww	0.0290234+-0.170363	0.0580205+-0.240874	0.0275619+-0.166018	0.114605+-0.338
data	8	20	7	35

Table 32: Summary of the signal and background expectations for a Higgs mass of 110 GeV, for 1fb^{-1}. Also the observed number of events is shown. The error on luminosity it is not included.

120 GeV	ee	$e\mu$	$\mu\mu$	ll
WW	3.68012+-1.91836	7.30096+-2.70203	3.39054+-1.84134	14.3717+-3.7910
WZ	0.128007+-0.35778	0.258016+-0.507953	0.150056+-0.387371	0.536079+-0.7321
ZZ	0.101481+-0.31856	0.047447+-0.217823	0.109655+-0.331142	0.258583+-0.5085
ttbar	0.0867645+-0.294558	0.223024+-0.472254	0.0642638+-0.253503	0.374052+-0.6115
wgamma	3.27832+-1.81061	2.81891+-1.67896	0.0136383+-0.116783	6.11087+-2.4720
DYll	2.21013+-1.48665	3.42003+-1.84933	2.12109+-1.4564	7.75125+-2.7841
Background Total	9.48483+-3.07974	14.0684+-3.75078	5.84925+-2.41852	29.4026+-5.4224
higgsww	0.0778719+-0.279055	0.156798+-0.395978	0.0739289+-0.271899	0.308602+-0.5555
data	9	21	7	37

Table 33: Summary of the signal and background expectations for a Higgs mass of 120 GeV, for 1fb^{-1}. Also the observed number of events is shown. The error on luminosity it is not included.

130 GeV	ee	$e\mu$	$\mu\mu$	ll
WW	4.68991+-2.16562	9.30639+-3.05064	4.22871+-2.05638	18.2253+-4.2691
WZ	0.16424+-0.405265	0.325574+-0.570591	0.186715+-0.432106	0.676529+-0.8225
ZZ	0.115788+-0.340276	0.0574877+-0.239766	0.122305+-0.349721	0.29558+-0.54367
ttbar	0.141228+-0.375803	0.340213+-0.583278	0.124603+-0.352992	0.606045+-0.7784
wgamma	3.00441+-1.73332	2.42149+-1.55611	0.0136383+-0.116783	5.43954+-2.3322
DYll	1.68313+-1.29736	2.42634+-1.55767	1.45469+-1.20611	5.56416+-2.3588
Background Total	9.79871+-3.13029	14.8775+-3.85713	6.13066+-2.47602	30.8071+-5.5504
higgsww	0.194773+-0.441331	0.399771+-0.632274	0.189108+-0.434866	0.783644+-0.8852
data	9	21	7	37

Table 34: Summary of the signal and background expectations for a Higgs mass of 130 GeV, for 1fb^{-1}. Also the observed number of events is shown. The error on luminosity it is not included.

140 GeV	ee	$e\mu$	$\mu\mu$	ll
WW	5.54751+-2.35532	11.012+-3.31843	4.94233+-2.22314	21.5023+-4.63
WZ	0.195519+-0.442176	0.386976+-0.622074	0.22248+-0.471678	0.804975+-0.89
ZZ	0.127316+-0.356813	0.0646188+-0.254202	0.135106+-0.367568	0.327041+-0.57
ttbar	0.208308+-0.456407	0.411076+-0.641152	0.152801+-0.390898	0.772184+-0.87
wgamma	2.51596+-1.58618	2.0344+-1.42632	0.00490359+-0.0700256	4.55526+-2.13
DYll	1.38921+-1.17865	2.05765+-1.43445	1.15117+-1.07293	4.59803+-2.14
Background Total	9.98383+-3.15972	15.9667+-3.99583	6.60879+-2.57076	32.5598+-5.70
higgsww	0.315779+-0.561942	0.665928+-0.816044	0.318881+-0.564696	1.3006+-1.140
data	10	20	10	40

Table 35: Summary of the signal and background expectations for a Higgs mass of 140 GeV, for 1fb^{-1}. Also the observed number of events is shown. The error on luminosity it is not included.

150 GeV	ee	$e\mu$	$\mu\mu$	ll
WW	6.20546+-2.49108	12.2995+-3.50707	5.43863+-2.33209	23.9442+-4.89
WZ	0.221234+-0.470355	0.433345+-0.658289	0.256398+-0.506358	0.910976+-0.95
ZZ	0.139937+-0.374081	0.0695204+-0.263667	0.143855+-0.379282	0.353312+-0.5
ttbar	0.270347+-0.519949	0.48775+-0.698391	0.212294+-0.460754	0.97039+-0.985
wgamma	2.0358+-1.42681	1.67037+-1.29243	0.00490359+-0.0700256	3.71107+-1.92
DYll	1.13238+-1.06413	1.49831+-1.22405	0.771631+-0.878425	3.40232+-1.84
Background Total	10.0052+-3.16309	16.4588+-4.05694	6.82771+-2.61299	33.2923+-5.76
higgsww	0.413883+-0.643338	0.888839+-0.942783	0.425892+-0.652604	1.72868+-1.31
data	11	21	12	44

Table 36: Summary of the signal and background expectations for a Higgs mass of 150 GeV, for 1fb^{-1}. Also the observed number of events is shown. The error on luminosity it is not included.

160 GeV	ee	$e\mu$	$\mu\mu$	ll
WW	6.64152+-2.57712	13.0747+-3.61589	5.72569+-2.39284	25.4426+-5.04406
WZ	0.243428+-0.493385	0.464913+-0.681845	0.282971+-0.53195	0.991311+-0.99564
ZZ	0.153975+-0.392396	0.0701528+-0.264864	0.152963+-0.391105	0.377091+-0.61407
ttbar	0.337+-0.580517	0.60536+-0.778049	0.255667+-0.505635	1.19803+-1.09454
wgamma	1.68568+-1.29834	1.30057+-1.14043	0+-0	2.98625+-1.72808
DYll	0.93314+-0.965992	1.33584+-1.15578	0.625877+-0.791124	2.89485+-1.70143
Background Total	9.99475+-3.16145	16.8515+-4.10506	7.04317+-2.6539	33.8901+-5.82152
higgsww	0.533054+-0.730106	1.15167+-1.07316	0.556758+-0.746162	2.24141+-1.49714
data	11	26	10	47

Table 37: Summary of the signal and background expectations for a Higgs mass of 160 GeV, for 1fb^{-1}. Also the observed number of events is shown. The error on luminosity it is not included.

170 GeV	ee	$e\mu$	$\mu\mu$	ll
WW	6.80989+-2.60958	13.3568+-3.65469	5.7429+-2.39643	25.9103+-5.09021
WZ	0.266956+-0.516678	0.482007+-0.694267	0.307026+-0.554099	1.05599+-1.02761
ZZ	0.176706+-0.420364	0.0715031+-0.267401	0.170613+-0.413053	0.418822+-0.64716
ttbar	0.38644+-0.621643	0.712892+-0.844329	0.309186+-0.556045	1.40852+-1.18681
wgamma	1.37314+-1.17181	1.03927+-1.01945	0+-0	2.41241+-1.55319
DYll	0.902282+-0.949885	1.09635+-1.04707	0.35969+-0.599742	2.35832+-1.53568
Background Total	9.91541+-3.14887	16.7588+-4.09375	6.88942+-2.62477	33.5643+-5.79347
higgsww	0.500126+-0.707196	1.08469+-1.04149	0.529272+-0.727511	2.11417+-1.45402
data	9	26	12	47

Table 38: Summary of the signal and background expectations for a Higgs mass of 170 GeV, for 1fb^{-1}. Also the observed number of events is shown. The error on luminosity it is not included.

180 GeV	ee	$e\mu$	$\mu\mu$	ll
WW	6.79238+-2.60622	13.1077+-3.62046	5.60007+-2.36645	25.5009+-5.04984
WZ	0.315696+-0.561868	0.488488+-0.698919	0.339151+-0.582366	1.14333+-1.06927
ZZ	0.241575+-0.491503	0.0724038+-0.269079	0.211518+-0.45991	0.525497+-0.72491
ttbar	0.436338+-0.660559	0.822782+-0.907073	0.366557+-0.60544	1.62568+-1.27502
wgamma	1.1675+-1.08051	0.874477+-0.935135	0+-0	2.04197+-1.42898
DYll	0.876647+-0.936294	0.972731+-0.986271	0.266752+-0.51648	2.11613+-1.45469
Background Total	9.83013+-3.1353	16.3386+-4.0421	6.78405+-2.60462	32.9535+-5.74052
higgsww	0.388507+-0.623303	0.815078+-0.902817	0.387876+-0.622797	1.59153+-1.26156
data	9	26	13	48

Table 39: Summary of the signal and background expectations for a Higgs mass of 180 GeV, for 1fb^{-1}. Also the observed number of events is shown. The error on luminosity it is not included.

190 GeV	ee	$e\mu$	$\mu\mu$	ll
WW	6.58856+-2.56682	12.6424+-3.55562	5.33203+-2.30912	24.5638+-4.95619
WZ	0.575267+-0.758464	0.477163+-0.69077	0.53663+-0.73255	1.58905+-1.26058
ZZ	0.596119+-0.772087	0.0700466+-0.264663	0.502813+-0.709093	1.16898+-1.08119
ttbar	0.462147+-0.679814	0.891301+-0.944087	0.418441+-0.64687	1.77189+-1.33112
wgamma	0.972764+-0.986288	0.687059+-0.82889	0+-0	1.65982+-1.28834
DYll	1.20718+-1.09872	0.888993+-0.942864	0.398421+-0.631206	2.49459+-1.57943
Background Total	10.402+-3.22522	15.657+-3.95689	7.18833+-2.68111	33.2481+-5.76612
higgsww	0.25243+-0.502424	0.532654+-0.729831	0.250945+-0.500944	1.03606+-1.01787
data	11	25	12	48

Table 40: Summary of the signal and background expectations for a Higgs mass of 190 GeV, for 1fb^{-1}. Also the observed number of events is shown. The error on luminosity it is not included.

200 GeV	ee	$e\mu$	$\mu\mu$	ll
WW	6.27676+-2.50535	11.9761+-3.46065	4.97748+-2.23103	23.2311+-4.81986
WZ	1.0683+-1.03359	0.458342+-0.67701	0.858301+-0.926445	2.38495+-1.54433
ZZ	1.30768+-1.14354	0.0655514+-0.25603	1.0104+-1.00519	2.38363+-1.5439
ttbar	0.492287+-0.701632	0.938823+-0.968929	0.434483+-0.659153	1.86559+-1.36587
wgamma	0.764119+-0.874139	0.542827+-0.736768	0+-0	1.30695+-1.14322
DYll	1.52714+-1.23577	0.858754+-0.92669	0.810553+-0.900307	3.19645+-1.78786
Background Total	11.4363+-3.38176	14.8404+-3.85232	8.09122+-2.84451	34.3686+-5.86248
higgsww	0.189838+-0.435704	0.395782+-0.629112	0.181702+-0.426265	0.767326+-0.875971
data	10	22	12	44

Table 41: Summary of the signal and background expectations for a Higgs mass of 200 GeV, for 1fb^{-1}. Also the observed number of events is shown. The error on luminosity it is not included.

B Cuts Analysis:All Mass point Cut Distributions

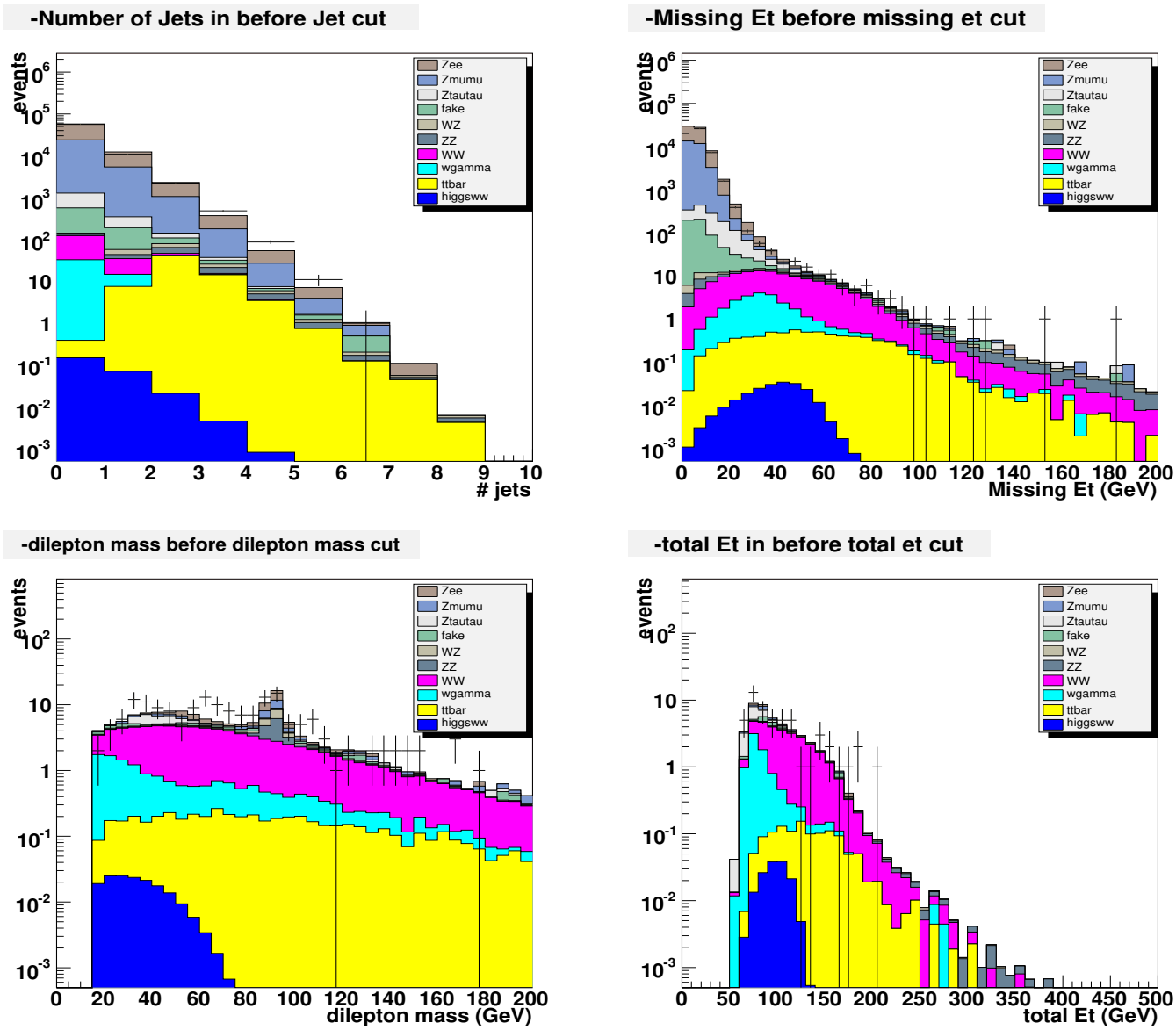

Figure 47: Four of the variables used in the event selection (for $M_H = 110$ GeV) are shown before cutting on that variable: (upper-left) number of jets; (upper-right) missing energy; (lower-left) dilepton invariant mass and (lower-right) $P_T(lep1) + P_T(lep2)+\not{E}_T$.

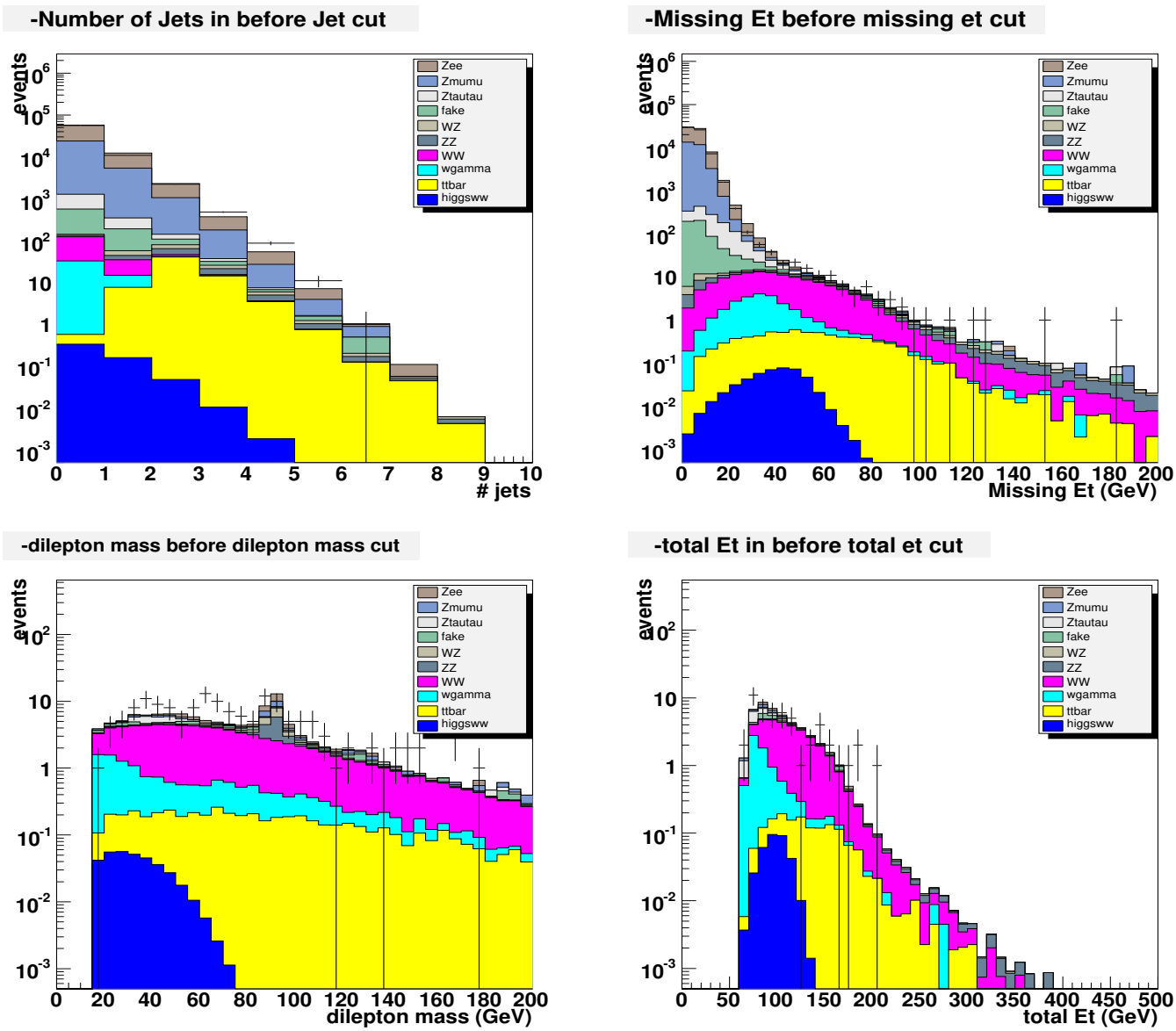

Figure 48: Four of the variables used in the event selection (for $M_H = 120$ GeV) are shown before cutting on that variable: (upper-left) number of jets; (upper-right) missing energy; (lower-left) dilepton invariant mass and (lower-right) $P_T(lep1) + P_T(lep2)+\not\!\!E_T$.

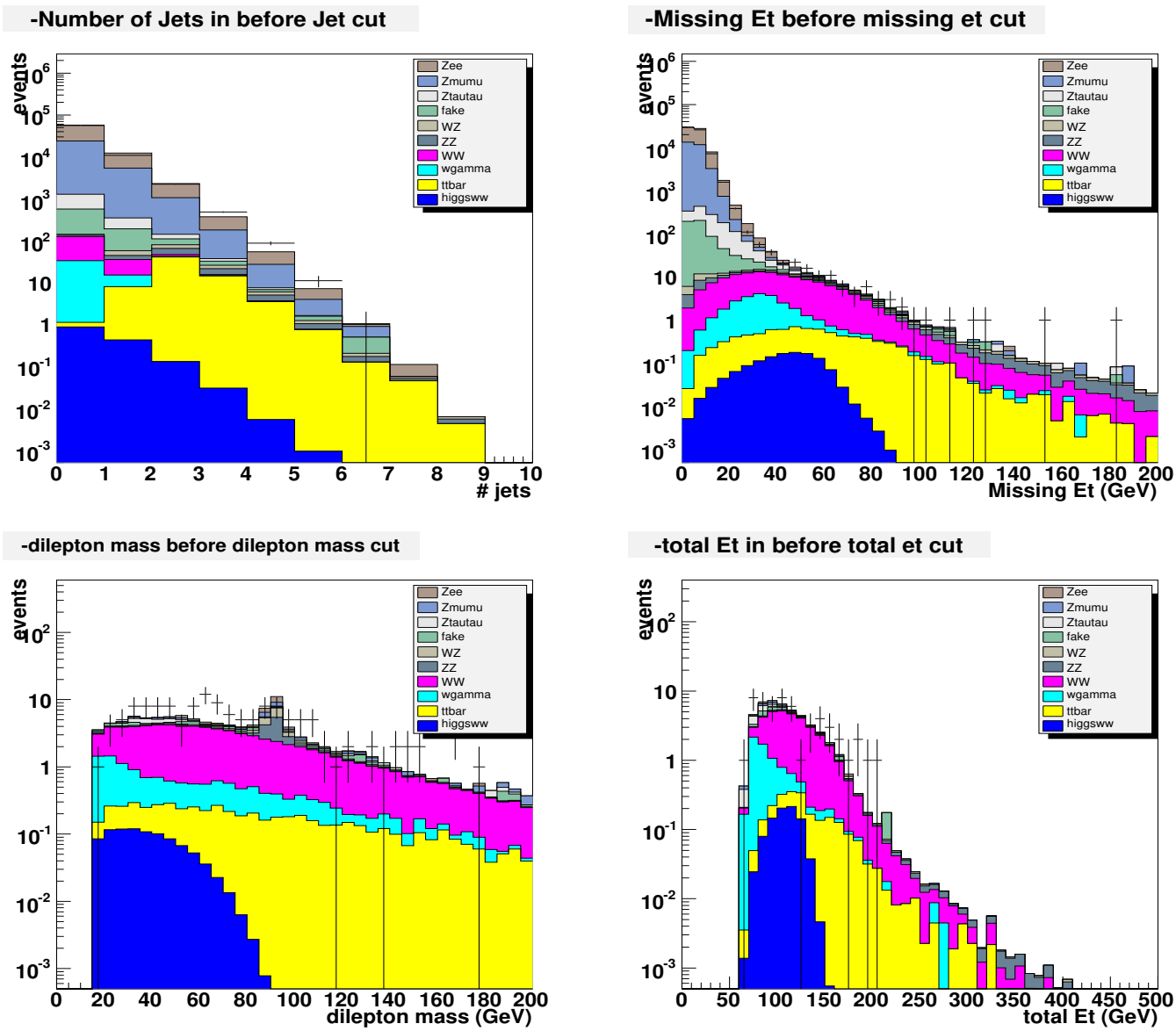

Figure 49: Four of the variables used in the event selection (for $M_H = 130$ GeV) are shown before cutting on that variable: (upper-left) number of jets; (upper-right) missing energy; (lower-left) dilepton invariant mass and (lower-right) $P_T(lep1) + P_T(lep2)+\not\!\!E_T$.

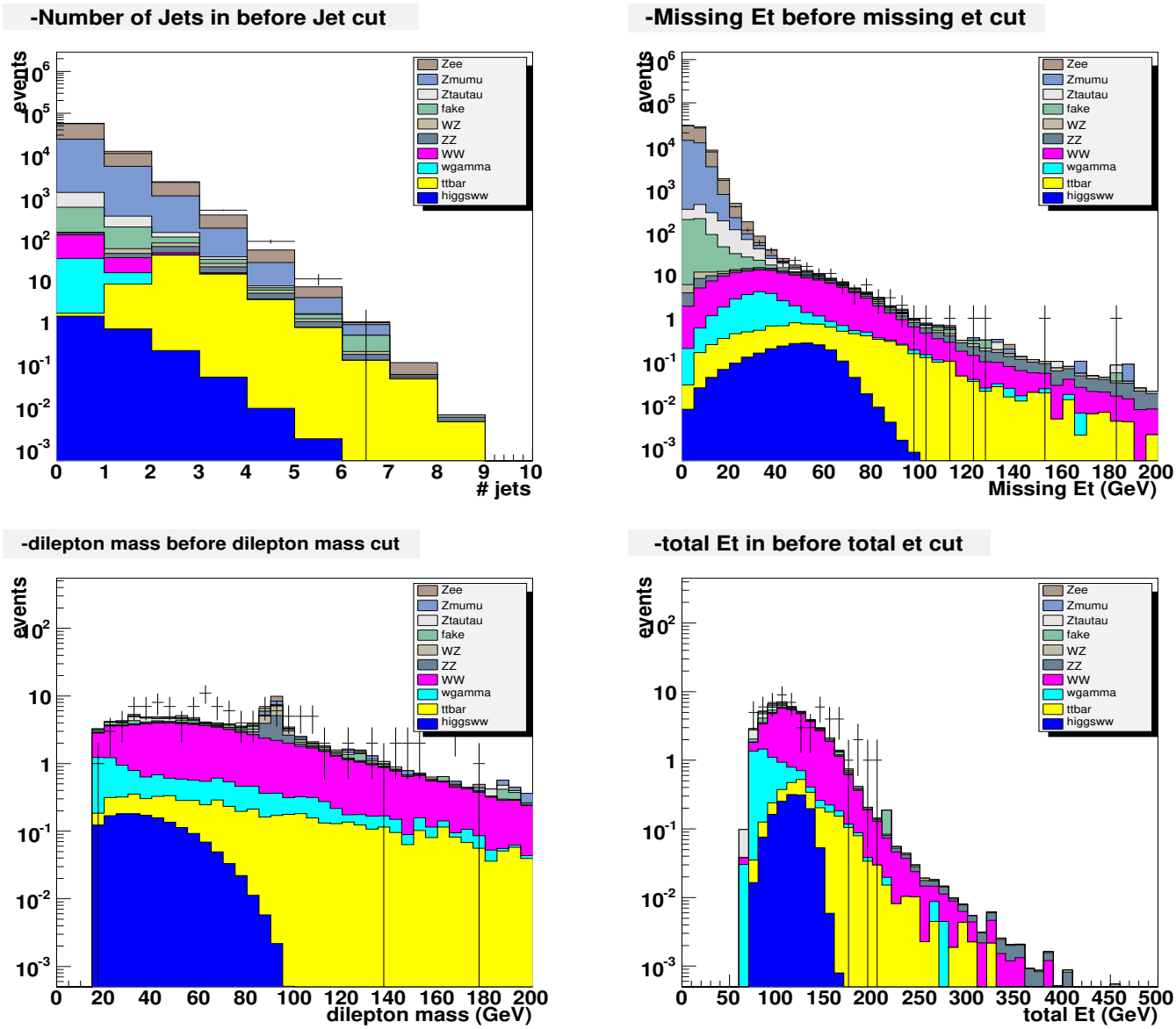

Figure 50: Four of the variables used in the event selection (for $M_H = 140$ GeV) are shown before cutting on that variable: (upper-left) number of jets; (upper-right) missing energy; (lower-left) dilepton invariant mass and (lower-right) $P_T(lep1) + P_T(lep2)+\not\!\!E_T$.

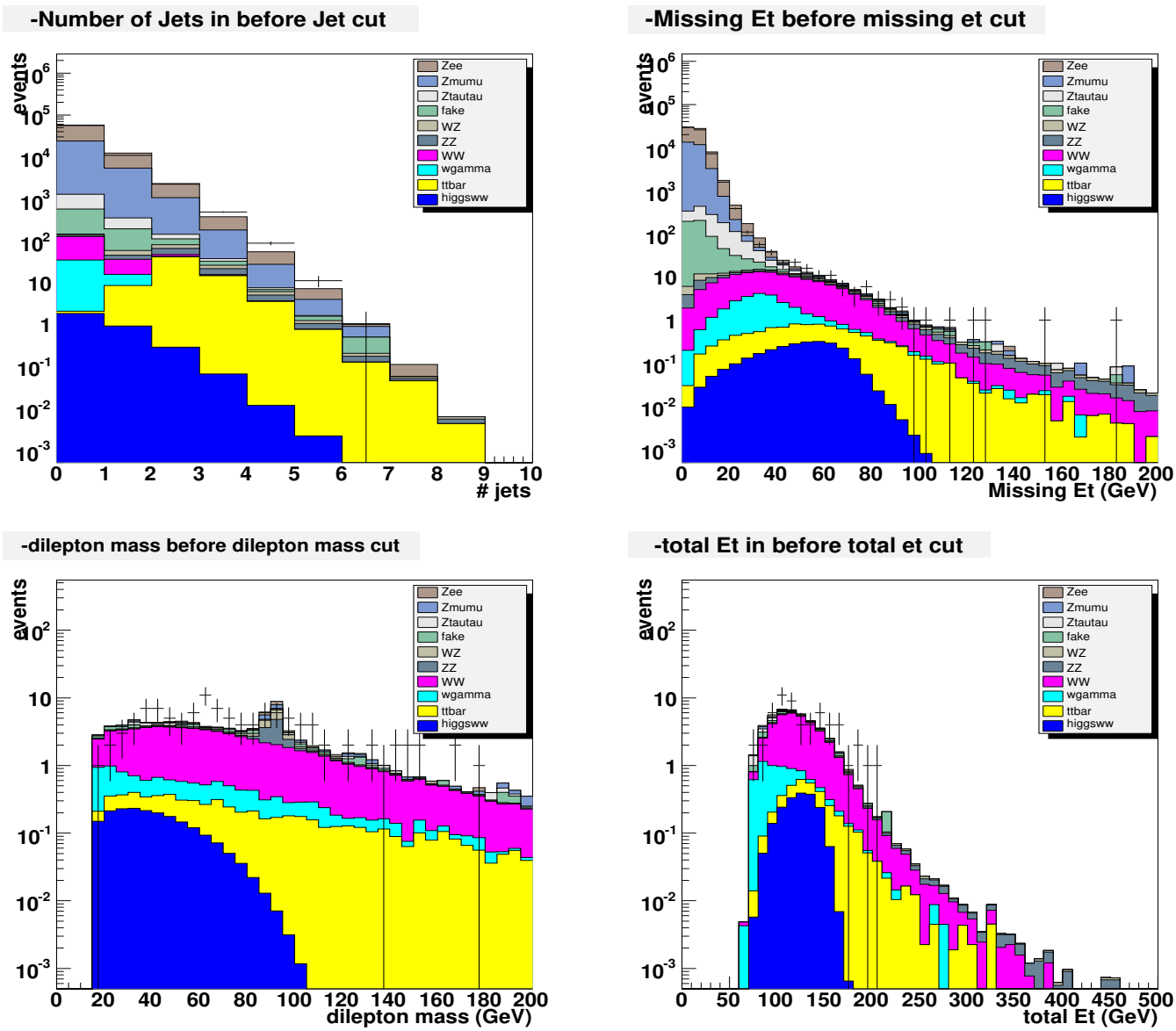

Figure 51: Four of the variables used in the event selection (for $M_H = 150$ GeV) are shown before cutting on that variable: (upper-left) number of jets; (upper-right) missing energy; (lower-left) dilepton invariant mass and (lower-right) $P_T(lep1) + P_T(lep2)+\not\!\!E_T$.

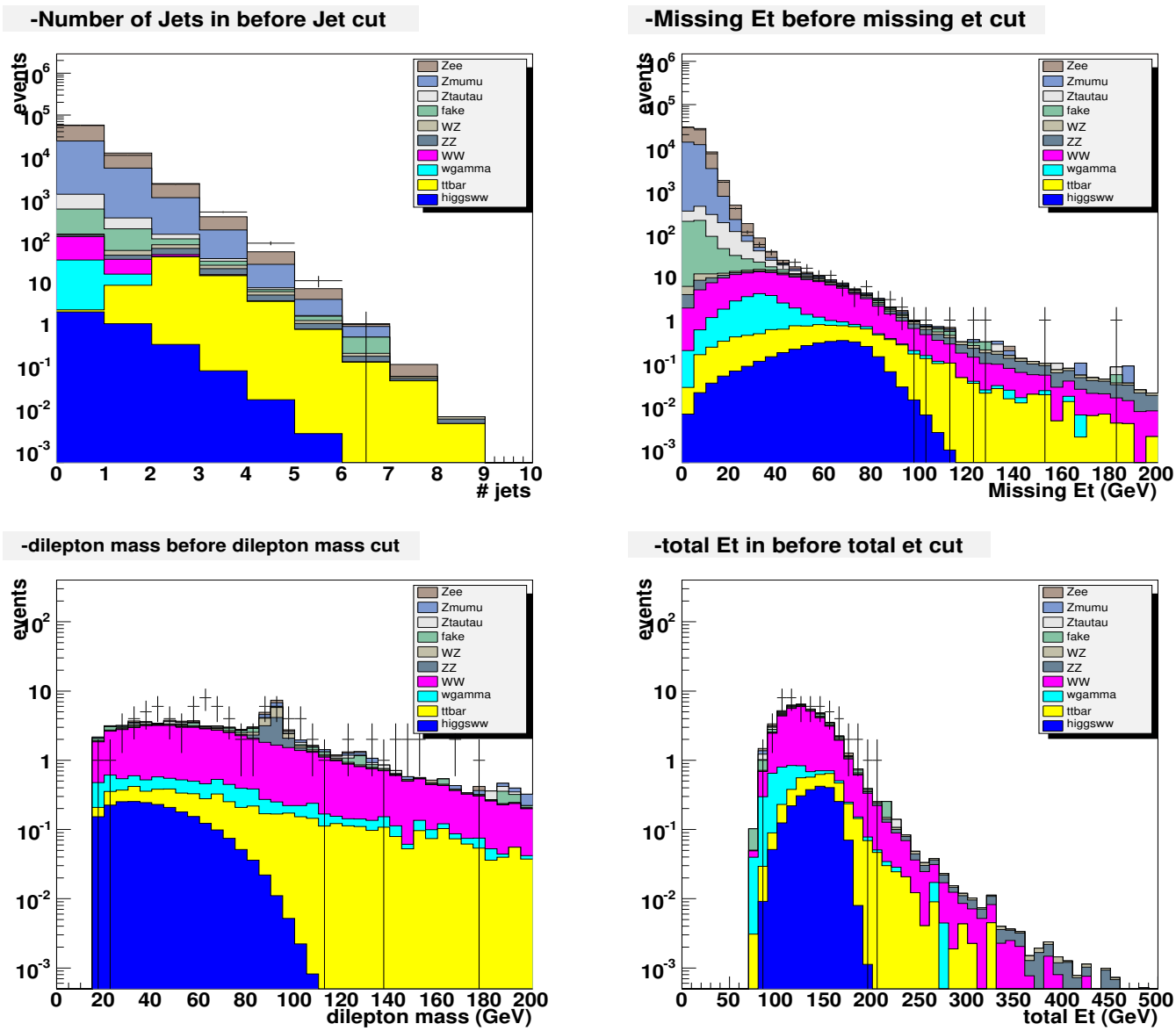

Figure 52: Four of the variables used in the event selection (for $M_H = 170$ GeV) are shown before cutting on that variable: (upper-left) number of jets; (upper-right) missing energy; (lower-left) dilepton invariant mass and (lower-right) $P_T(lep1) + P_T(lep2)+\not\!\!E_T$.

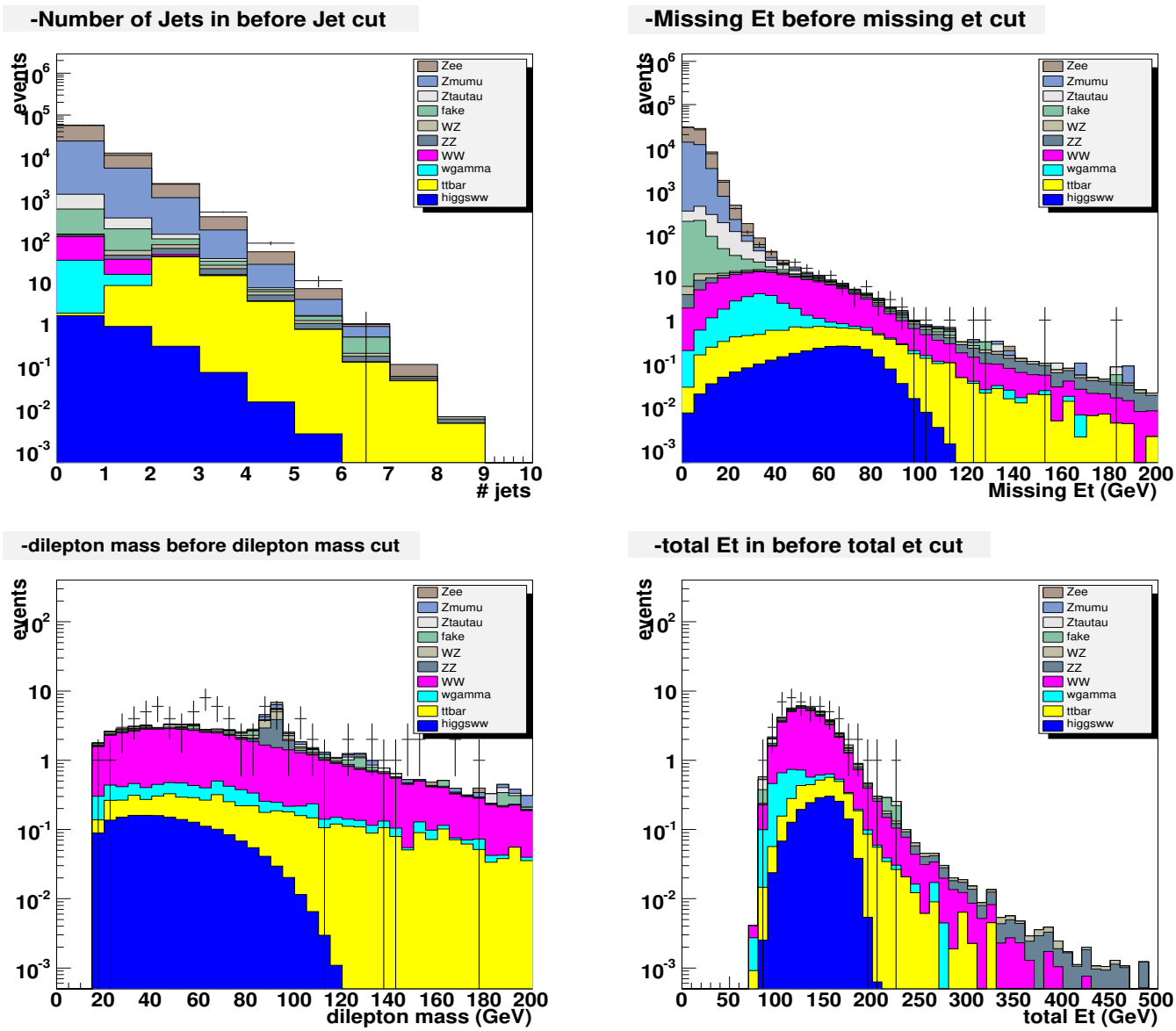

Figure 53: Four of the variables used in the event selection (for $M_H = 180$ GeV) are shown before cutting on that variable: (upper-left) number of jets; (upper-right) missing energy; (lower-left) dilepton invariant mass and (lower-right) $P_T(lep1) + P_T(lep2)+\not\!\!E_T$.

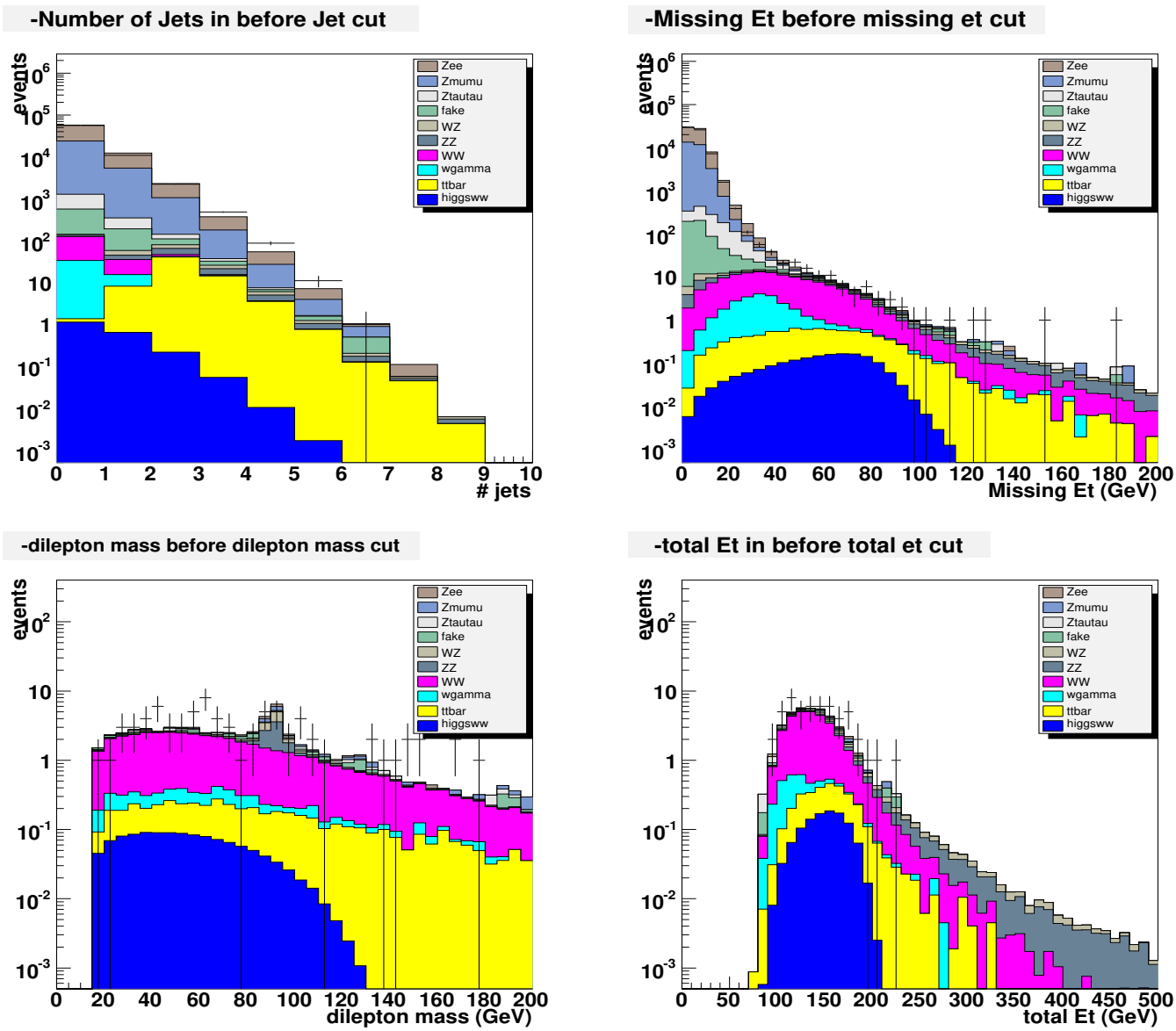

Figure 54: Four of the variables used in the event selection (for $M_H = 190$ GeV) are shown before cutting on that variable: (upper-left) number of jets; (upper-right) missing energy; (lower-left) dilepton invariant mass and (lower-right) $P_T(lep1) + P_T(lep2)+\not\!\!E_T$.

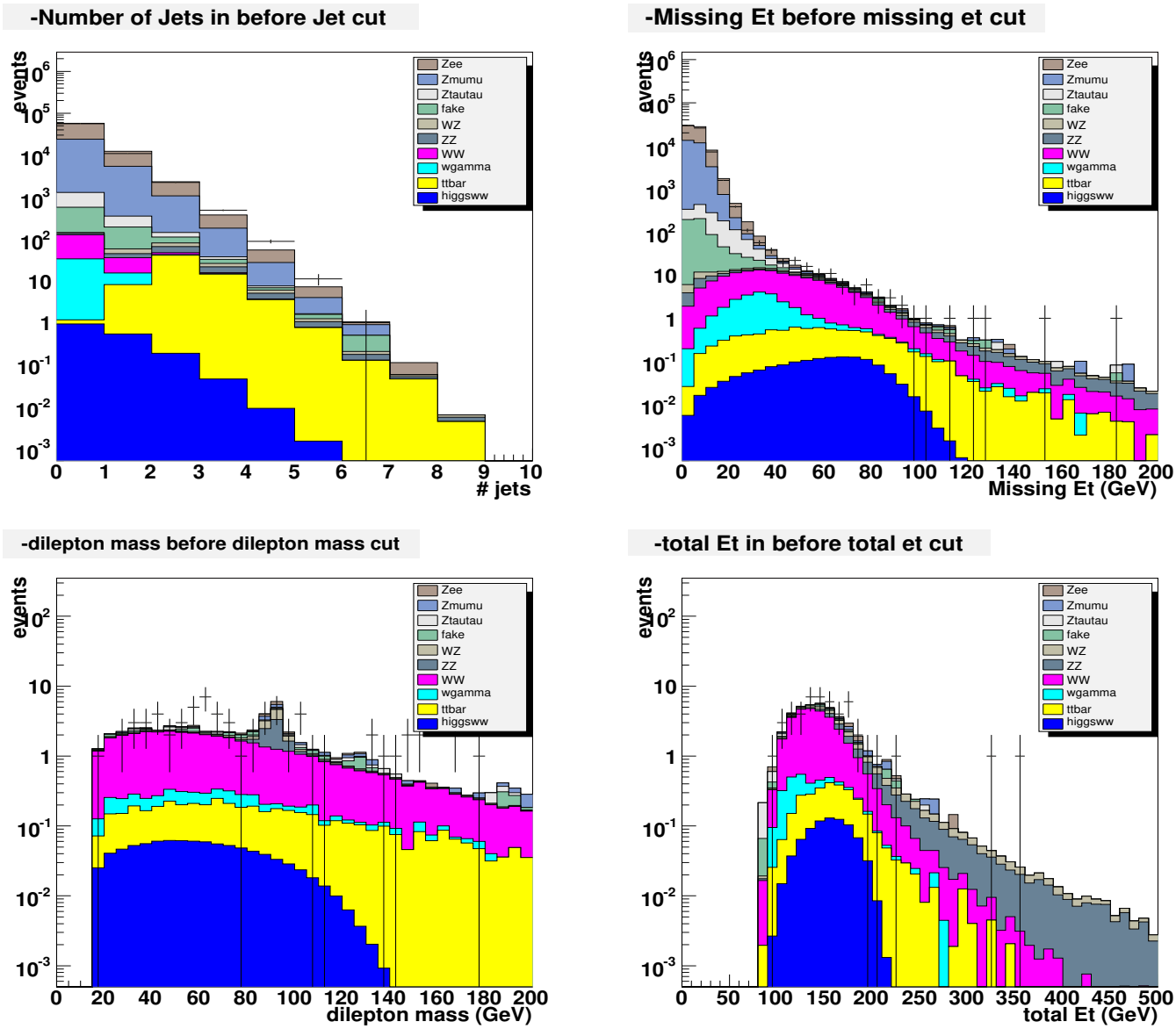

Figure 55: Four of the variables used in the event selection (for $M_H = 200$ GeV) are shown before cutting on that variable: (upper-left) number of jets; (upper-right) missing energy; (lower-left) dilepton invariant mass and (lower-right) $P_T(lep1) + P_T(lep2)+\not\!\!E_T$.

C Detailed Acceptance Tables

We present next the full tables of the number of data events after every selection cut, for all Higgs masses. Also we show the full tables for all backgrounds, for $M_H = 160$ GeV/c^2. For

simplicity we introduce the notations: $M_u \equiv M_H/2 - 5$ GeV (the upper cut on $M_{\ell\ell}$.) and $H_T \equiv {p_T}^{\ell_1} + {p_T}^{\ell_2} + \not{E}_T$.